DISSERTATION

Visualization of local intracellular & cell surface cation alterations using fluorescent protein-based probes

submitted by

BSc MSc

Sandra BURGSTALLER

for the Academic Degree of

Doctor of Philosophy

(PhD)

at the Medical University of Graz

Gottfried Schatz Research Center for Cell Signaling, Metabolism and Aging

under the supervision of

Assoz. Prof. Priv.-Doz. Mag.pharm. Dr.rer.nat. Roland Malli

2020

Statutory Declaration

I hereby declare that this thesis is my own original work and that I have fully acknowledged by name all of those individuals and organizations that have contributed to the research for this thesis. Due acknowledgement has been made in the text to all other material used. Throughout this thesis and in all related publications I followed the “Standards of Good Scientific Practice and Ombuds Committee at the Medical University of Graz“.

Place, Date Sandra Burgstaller

Disclosures

Parts of this thesis are reproduced in part or modified with permission from Burgstaller, S; Bischof, H; Gensch, T; Stryeck, S; Gottschalk, B; Ramadani-Muja, J; Eroglu, E; Rost, R; Balfanz, S; Baumann, A; Waldeck-Weiermair, M; Hay, JC; Madl, T; Graier, WF; Malli, R. pH-Lemon, a Fluorescent Protein-Based pH Reporter for Acidic Compartments. ACS Sens. 2019; 4(4): 883-891. https://pubs.acs.org/doi/10.1021/acssensors.8b01599 Copyright 2019 American Chemical Society.

I obtained permission from the American Chemical Society. For further permission concerning the material excerpted, ACS should be contacted. For the "Right and Permission" statements, please visit the American Chemical Society website and copyright policies. https://pubs.acs.org/page/copyright/permissions_journals.html

The following co-authors contributed to my publication and agreed with the use of their data within my thesis

Helmut Bischof[1], Thomas Gensch[2], Sarah Stryeck[3], Benjamin Gottschalk[1], Jeta-Ramadani-Muja[1], Emrah Eroglu[4], Rene Rost[1], Sabine Balfanz[2], Arnd Baumann[2], Markus Waldeck-Weiermair[5], Jesse C. Hay[6], Tobias Madl[1,7], Wolfgang F. Graier[1,7], Roland Malli[1,7]

[1] Medical University of Graz, Gottfried Schatz Research Center for Cell Signaling, Metabolism and Ageing, Neue Stiftingtalstraße 6/6, 8010 Graz, Austria

[2] Forschungszentrum Jülich, Institute of Complex Systems, Zelluläre Biophysik (ICS-4), 52428 Jülich, Germany

[3] Technical University of Graz, Institute of Interactive Systems and Data Science, 8010 Graz, Inffeldgasse 16c/I

[4] Sabanci University, Orta Mahallesi, No: 27, 34956 Tuzla/Istanbul, TURKEY

[5] Harvard Medical School, Brigham and Women's Hospital, Cardiovascular Division, 75 Francis Street,Boston MA, 02115, USA

[6] The University of Montana, Division of Biological Sciences and Center for Structural and Functional Neuroscience, 32 CampusDrive, HS410, Missoula 59812-4824, Montana United States

[7] BioTechMed Graz, Mozartgasse 12/II, 8010 Graz, Austria

During my PhD-thesis, I furthermore contributed to the following publications as a co-author

- Bischof, H; Burgstaller, S; Vujic, N; Madl, T; Kratky, D; Graier, WF; Malli. R Purification and Application of Genetically Encoded Potassium Ion Indicators for Quantification of Potassium Ion Concentrations within Biological Samples. Curr Protoc Chem Biol. 2019; 11(3): e71-e71.
- Ramadani-Muja, J; Gottschalk, B; Pfeil, K; Burgstaller, S; Rauter, T; Bischof, H; Waldeck-Weiermair, M; Bugger, H; Graier, WF; Malli, R. Visualization of Sirtuin 4 Distribution between Mitochondria and the Nucleus, Based on Bimolecular Fluorescence Self-Complementation. Cells. 2019; 8(12)
- Waldeck-Weiermair, M; Gottschalk, B; Madreiter-Sokolowski, CT; Ramadani-Muja, J; Ziomek, G; Klec, C; Burgstaller, S; Bischof, H; Depaoli, MR; Eroglu, E; Malli, R; Graier, WF. Development and Application of Sub-Mitochondrial Targeted Ca^{2+} Biosensors. Front Cell Neurosci. 2019; 13: 449-449.
- Yong, J; Bischof, H; Burgstaller, S; Siirin, M; Murphy, A; Malli, R; Kaufman, RJ. Mitochondria supply ATP to the ER through a mechanism antagonized by cytosolic Ca2. Elife. 2019; 8
- Bischof, H; Burgstaller, S; Waldeck-Weiermair, M; Rauter, T; Schinagl, M; Ramadani-Muja, J; Graier, WF; Malli, R. Live-Cell Imaging of Physiologically Relevant Metal Ions Using Genetically Encoded FRET-Based Probes. Cells. 2019; 8(5)
- Depaoli, MR; Bischof, H; Eroglu, E; Burgstaller, S; Ramadani-Muja, J; Rauter, T; Schinagl, M; Waldeck-Weiermair, M; Hay, JC; Graier, WF; Malli, R. Live cell imaging of signaling and metabolic activities. Pharmacol Ther. 2019; 202:98-119
- Madreiter-Sokolowski, CT; Ramadani-Muja, J; Ziomek, G; Burgstaller, S; Bischof, H; Koshenov, Z; Gottschalk, B; Malli, R; Graier, WF. Tracking intra- and inter-organelle signaling of mitochondria. FEBS J. 2019; 286(22):4378-4401

Acknowledgements

PhD student Sandra Burgstaller received funding from the Medical University of Graz through the PhD Program “Molecular Medicine” (MOLMED), by Nikon Austria within the Nikon-Center of Excellence (Graz), the Austrian Science Fund (FWF) projects I3716−B27 and P28529−B27 to R.M. and the doctoral program Metabolic and Cardiovascular Disease (DK-W1226) to W.F.G.

Danksagung

Mit diesen Zeilen möchte ich mich von Herzen bei allen bedanken, die mich während meiner Dissertation unterstützt haben. Es war eine unbeschreiblich tolle, spannende und aufregende Zeit, an die ich immer gerne zurückdenken werde.

Ein besonderer Dank gilt meinem Supervisor, Prof. Roland Malli, der es mir ermöglicht hat, in einem außergewöhnlichen Team an spannenden Projekten zu arbeiten und mich stets unterstützt hat. Er hat mich ermutigt, innovative Gedanken zu verfolgen und immer das Beste zu geben. Vielen Dank für den regen Ideenaustausch, die vielen Diskussionen und die Möglichkeit, eigene Ideen zu verfolgen und umzusetzen.

Des Weiteren möchte ich mich recht herzlich bei Prof. Wolfgang Graier bedanken, der mir als essentielles Mitglied meines Dissertations-Komitees jederzeit für Fragen und Diskussionen zur Seite stand. Die großartige Co-Betreuung war maßgeblich daran beteiligt, dass ich in den letzten Jahren meine Projekte mit großer Freude verfolgen konnte.

Ein herzliches Dankeschön gilt auch Prof. Seth Hallström, der als Teil meines Dissertations-Komitees stets neue Ideen einbrachte und mich mit seinem Wissen unterstützte und motivierte.

Ein großer Dank gilt meinen Co-Autoren Helmut Bischof, Thomas Gensch, Sarah Stryeck, Benjamin Gottschalk, Jeta Ramadani-Muja, Emrah Eroglu, Rene Rost, Sabine Balfanz, Arnd Baumann, Markus Waldeck-Weiermair, Jesse C. Hay und Tobias Madl, die mich mit ihrer großartigen Arbeit, ihrem Wissen, viel Motivation und Engagement auf meinem Weg begleitet haben.

Des Weiteren möchte mich besonders bei meinen lieben Kollegen und Freunden Jeta und Thomas, sowie der ganzen AG Malli/Graier bedanken, ohne die die letzten Jahre nicht einmal halb so lustig, spannend und emotional gewesen wären. Ein großer Dank gilt auch Anna, Sandra und Sonja, für die tolle Unterstützung während meines PhD. Ich kann wahrlich behaupten, dass ich nicht nur Kollegen, sondern gute Freunde während der letzten Jahre gewonnen habe.

Ein ganz besonderer Dank gilt meiner Familie, ohne die ich meine Träume nicht hätte verwirklichen können. Meine Eltern haben immer an mich geglaubt und mich über so viele Jahre hinweg unterstützt und motiviert.

Zu guter Letzt danke ich meinem Kollegen und Partner Helmut, der mich nicht nur mit seiner großartigen Arbeit und unzähligen Diskussionen unterstützt hat, sondern mich stets motiviert hat über mich hinaus zu wachsen. Vielen Dank für die wunderbare Zeit.

INDEX

Abbreviations 1
List of Figures 3
List of Tables 4
Zusammenfassung 5
Abstract 6
1 Introduction 7
1.1 Intracellular pH homeostasis and regulation 7
1.1.1 pH homeostasis of mitochondria 7
1.1.2 pH homeostasis of the cytosol, the nucleus & the endoplasmic reticulum 8
1.1.3 pH homeostasis of the Golgi complex 9
1.1.4 pH homeostasis of intracellular vesicles 9
1.2 Lysosomes and their involvement in autophagy 10
1.3 Role of V-ATPase in vesicular acidification 11
1.4 Cellular pH dyshomeostasis 12
1.5 Cell metabolic activity affects extracellular pH 13
1.6 Genetically encoded pH sensors 13
1.7 Strategies for extracellular sensor immobilization 15
2 Materials and Methods 17
2.1 Chemicals, Buffers and Solutions 17
2.1.1 Chemicals 17
2.1.2 Buffers used for protein purification 17
2.1.3 Buffers used for the characterization of recombinant sensors 18
2.1.4 Buffers used for fluorescence microscopy 18
2.2 Design of sensor constructs 19
2.2.1 pH-Lemon sensor cloning and subcellular targeting 19
2.2.2 Recombinant pH sensors 22
2.2.3 Recombinant traptavidin-fusion constructs 22
2.3 Protein purification & *in vitro* fluorimetry 22
2.3.1 Recombinant protein expression and purification 22
2.3.2 Characterization of recombinant proteins 23
2.4 Fluorescence lifetime imaging 24
2.4.1 Fluorescence lifetime imaging spectroscopy in vitro 24
2.4.2 Fluorescence lifetime imaging microscopy in situ 24
2.5 Wide-field imaging microscopy 25
2.6 High resolution imaging 25
2.7 Cell cultivation and transfection 26

2.8 Cell treatments 27
2.8.1 Starvation of cells 27
2.8.2 Neutralization of endosomal vesicles 27
2.8.3 Acidic compartment staining 27
2.9 Calibration of pH-Lemon constructs 27
2.9.1 Calibration of pH-Lemon - cyto 27
2.9.2 Calibration of pH-Lemon - GPI 28
2.10 Application of buffers and substances 28
2.10.1 Application by hand 28
2.10.2 Application via gravity-based perfusion system 28
2.10.3 Application via BioPen® SYSTEMS - Fluicell 28
2.11 Traptavidin-Biotin coupling 29
2.11.1 Coupling of Traptavidin constructs on the cell surface 29
2.11.2 Coupling of traptavidin constructs on glass slides 29
2.12. Data analysis & statistical analysis 29
3 Aims and Objectives 30
4 Results 31
4.1 EYFP fluorescence is sensitive to pH 31
4.2 Fusion constructs of mTurquoise2 and EYFP respond to pH alterations in a ratiometric manner 32
4.3 Design and characterization of pH-Lemon *in vitro* 34
4.4 The pH sensitivity of pH-Lemon is independent of the environmental temperature 36
4.5 pH-Lemon is insensitive to physiological changes of intra- or extracellular cation concentrations 37
4.6 pH-Lemon is suitable for the detection of intracellular H^+ alterations 38
4.7 Image-based read-out of pH alterations *in situ* 40
4.8 Separate exposure of the FPs enhances the dynamic range of pH-Lemon 41
4.9 pH-Lemon is suitable for fluorescence lifetime imaging microscopy 43
4.10 pH-Lemon does not discriminate between neutral to alkaline pH values 45
4.11 pH-Lemon fused to LC3B detects autophagic vesicles 46
4.12 pH-Lemon is suitable for the real-time visualization of autophagy 48
4.13 Targeting pH-Lemon to the secretory pathway 49
4.14 Revealing the pH heterogeneity of secretory vesicles using pH-Lemon 51
4.15 Visualization of vesicles with different pH values using fluorescence lifetime imaging microscopy 52
4.16 pH-Lemon features high stability in acidic environments 53
4.17 Precise real-time determination of vesicular pH values using pH-Lemon - GPI 56
4.18 pH-Lemon is suitable to monitor V-ATPase activity 58
4.19 Extracellular pH strongly affects vesicular pH levels 60

4.20 Novel approach for targeting pH-Lemon solely to the plasma membrane.....61
4.21 Immobilization of purified sensors at the cell membrane using the traptavidin-biotin interaction.....63
4.22 Precise monitoring of extracellular pH alterations using purified traptavidin-pH-Lemon bound to biotin.....65
4.23 Recording extracellular K^+ changes at the cell surface.....66
4.24 Fusion of traptavidin to GEPII does not impair structural rearrangement *in vitro*.....67
4.25 Traptavidin-GEPII 1.0 remains functional upon immobilization at the cell surface.....68
4.26 Immobilization of traptavidin fusion constructs on glass surfaces allows pH and K^+ determinations within fluids.....70
4.27 Traptavidin-GEPII 1.0 is functional after immobilization via microperfusion.....73
4.28 Coupling of selected cells using microperfusion.....74
5 Discussion.....76
6 References.....86

Abbreviations

Ψ_{mito}	Mitochondrial membrane potential
$[H^+]$	Proton concentration
$[H^+]_i$	Intracellular proton concentration
$[K^+]$	Potassium ion concentration
$[Na^+]$	Sodium ion concentration
AD	Alzheimer's Disease
ADP	Adenosine-5'-diphosphate
AP	Biotin acceptor peptide
ATG	Autophagy related gene
ATP	Adenosine-5'-triphosphate
ATPase	Adenosine phosphatase
Baf-A	Bafilomycin-A
BirA	*Escherichia coli* biotin ligase
Ca^{2+}	Calcium ion
CaR	Calreticulin
CDH13	Cadherin 13
CFP	Cyan fluorescent protein
Cl^-	Chloride ion
CO_2	Carbon dioxide
DAMP	N-{3-[(2,4-Dinitrophenyl)amino]propyl}-N-(3-aminopropyl)methylamine dihydrochloride
E.coli	*Eschericha coli*
EE	Early endosome
ER	Endoplasmic reticulum
FITC	Fluorescein isothiocyanate
FP	Fluorescent protein
FRET	Förster resonance energy transfer
GEPII	Genetically-encoded potassium ion indicator
GFP	Green fluorescent protein
GPI	Glycosylphosphatidylinositol

H^+	Hydrogen ion
HCO_3^-	Hydrogen carbonate
H_2CO_3	Carbonic acid
ILV	Intravesicular vesicle
IMM	Inner mitochondrial membrane
IMS	Intermembrane space
K^+	Potassium ion
KDEL	Endoplasmic reticulum retention site
LC3	Microtubule-associated proteins 1A/1B light chain 3B
LE	Late endosome
MCT	H^+-monocarboxylate co-transporter
Mg^{2+}	Magnesium ion
MLS	Membrane leading sequence
mPTP	Mitochondrial permeability transition pore
mTOR	Mammalian target of rapamycin
MVB	Multivesicular body
Na^+	Sodium ion
NHE	Na^+/H^+ exchanger
OMM	Outer mitochondrial membrane
PD	Parkinson's Disease
PEG	Polyethylene glycol
pH_{ex}	Extracellular pH
pH_i	Intracellular pH
pHLIP	pH low insertion peptide
pKa	Acid dissociation constant
RAVE	Regulator of the H^+ adenosine phosphatase of the vacuolar and endosomal membrane
RFP	Red fluorescent protein
TME	Tumor microenvironment
V-ATPase	Vacuolar-type H^+ adenosine phosphatase
YFP	Yellow fluorescent protein

List of Figures

Figure 1: pH sensitivity of mTurquoise2 and EYFP 32
Figure 2: Design and characterization of differently orientated fusion constructs of mTurquoise2 and EYFP 33
Figure 3: Design and characterization of pH-Lemon *in vitro* 35
Figure 4: pH-Lemon is temperature insensitive *in vitro* 37
Figure 5: pH-Lemon is not affected by changes of physiologically relevant ion concentrations 38
Figure 6: Characterization of cytosolic pH-Lemon in HeLa cells 39
Figure 7: Visualization of intracellular pH alterations using an image-based read-out 41
Figure 8: Direct illumination of the two FPs, mTurquoise2 and EYFP, increases the dynamic range of pH-Lemon 42
Figure 9: pH-Lemon is suitable for the detection of pH alterations using fluorescence lifetime imaging microscopy (FLIM) 44
Figure 10: Targeting of pH-Lemon to intracellular compartments for the visualization of pH levels 45
Figure 11: pH-Lemon is targeted to autophagic vesicles upon fusion to LC3B 47
Figure 12: Dynamic visualization of autolysosome formation 48
Figure 13: Targeting the secretory pathway by expression of pH-Lemon – GPI 49
Figure 14: Classification of vesicles into different sub-categories based on their pH values 51
Figure 15: Detection of vesicular pH levels using FLIM 52
Figure 16: EYFP fluorescence was restored upon neutralization of vesicular pH levels 54
Figure 17: Heterogeneous response of intracellular vesicles upon treatment with neutralizing agents 55
Figure 18: Dynamic real-time measurements of vesicular pH changes 57
Figure 19: Monitoring vesicular pH as a measure of V-ATPase activity 58
Figure 20: Dynamic real-time determination of pH values to resolve V-ATPase activity 59
Figure 21: Effect of extracellular pH alterations on vesicular pH levels 60
Figure 22: Expression of AviTag and the enzyme biotin ligase (BirA) to obtain membrane-bound biotin 62
Figure 23: Cell surface labelling with traptavidin-pH-Lemon 64
Figure 24: Dynamic real-time imaging of traptavidin-pH-Lemon bound to biotinylated AviTag 65
Figure 25: Targeting of GEPII 1.0 to the plasma membrane via a GPI-anchor caused K^+ insensitivity 67
Figure 26: Purified traptavidin-GEPII 1.0 accurately measures [K^+] in vitro 68
Figure 27: Traptavidin-GEPII 1.0 detects extracellular K^+ alterations at the cell surface 69
Figure 28: Binding traptavidin-pH-Lemon to glass surfaces allows long-term measurements and storage 70
Figure 29: Immobilized traptavidin-GEPII 1.0 enables the determination of K^+ levels in fluids 71
Figure 30: Measuring K^+ alterations in a defined area of immobilized protein 72
Figure 31: Generation of sensor patterns via a microperfusion enables K^+ meaurements within a small, defined region 73
Figure 32: Living cells are highly accessible to be coupled with traptavidin-GEPII 1.0 using the microperfusion system 75

List of Tables

Table 1: Nucleotide sequences for cloning different pH-Lemon constructs.....20
Table 2: Primers used to generate pH-Lemon constructs.....21

Zusammenfassung

Die Aufrechterhaltung und Regulation des intrazellulären pH-Wertes ist für jede Zelle von größter Bedeutung, da viele wesentliche Stoffwechselprozesse auf einer streng kontrollierten pH-Homöostase basieren. Letztendlich stören schon kleineste pH-Änderungen den Zellstoffwechsel, indem sie wichtige Zellpfade beeinflussen und so verschiedene Krankheiten fördern. Dabei spielen nicht nur intrazelluläre, sondern auch extrazelluläre pH-Werte eine wichtige Rolle. pH-Lemon, ein Sensor bestehend aus einem pH-stabilen und einem pH-sensitiven fluoreszierenden Protein (FP), eignet sich hervorragend zur Visualisierung von intrazellulären sauren pH-Werten. Die Lokalisation von pH-Lemon in sekretorischen Vesikeln und Autolysosomen zeigte eine große Heterogenität der vesikulären pH-Werte. Reversible Veränderungen dieser intravesikulären pH-Werte konnten in Echtzeit mit hoher Genauigkeit gemessen werden. In Anbetracht der Anwendung von pH-Lemon zum Nachweis extrazellulärer pH-Werte wurden verschiedene Techniken entwickelt, um die Zellmembranlokalisierung des Sensors zu erreichen. Neben der Expression von GPI-verankertem pH-Lemon beschreiben wir neuartige Techniken, welche die Anwendung von rekombinanten gereinigten genetisch codierten Sensoren umfassen. Die Immobilisierung gereinigter Sensoren an der Plasmamembran lebender Zellen öffnet neue Türen für noch unbekannte Anwendungen genetisch codierter Sensoren. Darüber hinaus stellte sich unsere Methode als ideal heraus, um rekombinante Sensorproteine auf Glasoberflächen zu immobilisieren, was zu neuen Ansätzen auf dem Gebiet der Zellbiologie, Medizin und Biotechnologie führen könnte.

Abstract

The maintenance and regulation of intracellular pH levels is of utmost importance for every cell, since many essential metabolic processes rely on a tightly controlled pH homeostasis. Eventually, small pH alterations might disturb cell metabolism by affecting important cellular pathways, thereby promoting various diseases. However, not only intracellular, but also extracellular pH alterations play an important role. Hence, the determination and visualization of intra- and extracellular pH values might lead to crucial insight into the development and progression of various diseases. In order to measure pH levels and alterations with high precision, we developed pH-Lemon, a pH indicator based on Förster resonance energy transfer (FRET). pH-Lemon, a probe consisting of a pH stable and a pH sensitive fluorescent protein (FP), is perfectly suitable for the visualization of intracellular acidic pH values. Localization of pH-Lemon within secretory vesicles and autolysosomes revealed a great heterogeneity of vesicular pH values. Reversible alterations of these intravesicular pH levels could be measured with high precision in real-time. Considering the application of pH-Lemon to detect extracellular pH levels, different techniques to obtain cell membrane localization of the probe have been developed. Besides expression of GPI-anchored pH-Lemon, we describe novel techniques comprising the application of recombinant purified genetically-encoded sensors. The immobilization of purified sensors on the plasma membrane of living cells opens new doors for yet unknown applications of genetically-encoded probes. Furthermore, our method proved perfectly suitable for the immobilization of recombinant sensor proteins on glass surfaces, leading to new approaches in the field of cell biology, medicine and biotechnology.

1 Introduction

1.1 Intracellular pH homeostasis and regulation

The regulation of intracellular pH (pH_i) values is of utmost importance to guarantee an intact and functional cell metabolism, therefore, pH values are tightly controlled and regulated (1,2). Hence, disturbances of pH_i levels play a major role in the development and progression of many different diseases (3–6). Recent evidences suggest that severe brain disorder such as Alzheimer's disease (AD) or Parkinson's disease (PD) might be promoted by a pH imbalance in the brain (6–8). Considering such serious consequences of pH dysregulations, the determination of pH_i values represents an important tool to gain a better understanding of the complex interplay of pH and other metabolic processes.

1.1.1 pH homeostasis of mitochondria

The pH of intracellular organelles is widely spread over a huge pH range under physiological conditions (9,10). Due to their role in cell metabolism, mitochondria represent a unique compartment in terms of pH, harboring alkaline and acidic pH values in one organelle (11–13). The mitochondrial matrix is known to be alkaline with pH values in the range of 7.6 to 8.0, while it has been demonstrated, that the intermembrane space (IMS) contains mildly acidic pH values (14–16). The events causing this pH gradient across the inner mitochondrial membrane have already been described in 1961 by Mitchell et al.(16). Energy that is produced as a result of the serial reduction of electrons is responsible for the generation of a hydrogen ion (H^+) gradient, due to the shuttling of H^+ against their gradient by complexes I, III and IV of the respiratory chain from the mitochondrial matrix into the IMS. The pH gradient established by the extrusion of H^+, as well as the mitochondrial membrane potential (Ψ_{mito}), force H^+ to re-enter the mitochondrial matrix. This re-entering is essential for the generation of adenosine-5'-triphosphate (ATP) via the F_0/F_1 ATP-Synthase located in the inner mitochondrial membrane (IMM)(16–18). Besides H^+, also other ions rely on the generated H^+ gradient in order to enter the mitochondrial matrix (19–21). ATP-adenosine-5'-diphosphate (ADP) exchangers are dependent on Ψ_{mito} to fulfill their work, while sodium ion (Na^+)/H^+ exchangers, as well as potassium ion (K^+)/H^+ exchangers, in contrast, rely on the H^+ gradient (22–24). Alterations of this sensitive homeostasis might have severe consequences. As an example, increased mitochondrial calcium ion (Ca^{2+}) levels result in a higher permeability of the IMM, which eventually favors the opening of the mitochondrial permeability transition pore (mPTP). Subsequent cytochrome c release will initiate the apoptotic cascade by activation of caspases, finally resulting in programmed cell death (25,26).

1.1.2 pH homeostasis of the cytosol, the nucleus & the endoplasmic reticulum

While the mitochondrial matrix represents the most alkaline compartment within a cell, the cytosolic pH is slightly above neutral with pH values around 7.2 (27). This pH has to be tightly regulated, as essential physiological processes would cause pH alterations (28). As an example, glycolytic activity has the potential to cause elevated H^+ levels within the cytosol, leading to decreased intracellular pH values (28–30). If not regulated, many intracellular processes might be impaired, since several enzymes located in the cytosol rely on controlled pH values to fulfill their role. Furthermore, ion transporters and channels have also been described to function in a pH dependent manner (31–34). Therefore, the cell is in need of complex regulation systems to control the intracellular H^+ concentration ($[H^+]_i$). Due to their H^+ buffering capacity, intracellular weak acids and bases, as well as phosphate groups are responsible for regulating pH levels (27). Another mechanism for buffering excess cytosolic H^+ consists of the bicarbonate buffering system. Hydrogen carbonate (HCO_3^-) is generated upon hydration and deprotonation of carbon dioxide (CO_2) and effectively binds excess H^+ in order to generate CO_2, which is membrane permeable and can easily pass the cell membrane (35–37). Cells furthermore possess several other possibilities to restore intracellular pH, comprising different H^+ transporters (38–40). These transporters are located within the plasma membrane of most cells as well as the membranes of some intracellular vesicles, and mostly represent exchangers of alkali metal cations against H^+ (41,42). While there are many different types known in mammalian cells, especially the Na^+/H^+ Exchanger 1 (NHE1) located at the plasma membrane plays an important role in pH homeostasis (43–45). The exchanger thereby utilizes the Na^+ gradient comprising high extracellular and low intracellular Na^+ concentrations ($[Na^+]$). This difference is responsible for the exchange of Na^+ against H^+ via NHE1, causing effective deprotonation of the cytosol (46,47). Considering increased lactate and pyruvate production during glycolysis, H^+-monocarboxylate co-transporters (MCTs) manage the export of glycolytic products by co-transporting H^+ out of the cell (48,49). Nonetheless, to ensure cellular pH homeostasis, also alkalinization of the cytosol has to be prevented. Hence, cells are also capable of importing acidic loads to restore physiological pH levels (50). Although the cytoplasmic pH has been extensively studied over the last years, the nuclear pH is still an ongoing debate. While some might hypothesize that the pH is similar to the cytosol due to possible free diffusion of H^+, other groups reported that there is indeed a pH gradient between the nucleus and the cytosol that seems to be tightly regulated (51–53). Experiments using fluorescent dyes targeted to the endoplasmic reticulum (ER) also revealed a neutral pH within this organelle, similar to the pH found in the cytosol (54,55).

1.1.3 pH homeostasis of the Golgi complex

Considering the high dynamics of the Golgi complex, the pH of this compartment remained a mystery for quite a long time. Glickman and colleagues were the first to determine Golgi pH levels using electron microscopy in combination with N-{3-[(2,4-Dinitrophenyl)amino]propyl}-N-(3-aminopropyl)methylamine dihydrochloride (DAMP), a compound accumulating within acidic structures (56). Since then, different methods and techniques have been developed to accurately determine the different pH levels of the cis-Golgi with a pH of around 6.8, while the trans-Golgi possesses more acidic pH of around 6.0 (57–59). As the pH level of the Golgi complex is more acidic than the cytosol, the Golgi membrane requires H^+ pumps or -channels for establishing the mild acidic pH. Two of these regulators represent the vacuolar-type H^+ adenosine phosphatase (V-ATPase), a H^+ pump located within the membrane of the Golgi apparatus, that is responsible for the generation of mild acidic pH levels within the Golgi lumen, and the counter-ion transport of chloride ions (Cl-)(60,61). However, the Golgi seems to have another mechanisms regulation pH, as H^+ leaking back into the cytosol are thought to prevent the compartment from reaching an unphysiological H+ concentration [H^+] (60). Although Golgi pH is known to regulate important functions such as secretion, trafficking and protein sorting, the distinct roles of membrane transporters are still not fully characterized (62,63).

1.1.4 pH homeostasis of intracellular vesicles

In contrast to other organelles found in mammalian cell, the pH of most intracellular vesicles is low to highly acidic, which is crucial for these structures to fulfill their roles. These vesicles originate from different sources and belong to different pathways. Nonetheless they work together within a complex interplay to regulate cell homeostasis (61,64,65).

i. Secretory vesicles

In order to transport essential components towards the cell membrane, secretory vesicles are formed by the ER or by the Golgi complex containing the cargo that should be delivered (66). However, the transported cargoes can differ widely. Not only plasma membrane proteins are packed into vesicles to reach their final localization, also secretory proteins such as hormones reach the extracellular space by vesicular transport (66,67). Important communication between cells is possible due to vesicle release by the cell. As an example, neuronal vesicles, containing neurotransmitters, fuse with the synaptic membrane for subsequent release of their cargo into the synaptic cleft, enabling signal transduction (68,69). One hallmark of cellular secretion is the transition of vesicular pH values during transport and the maturation of vesicles from the Golgi towards the plasma membrane.

While newly synthesized vesicles that emanated from the Golgi complex are thought to have a similar pH than the Golgi itself, vesicles acidify upon transport to the cell membrane. As a result, vesicular pH values range from mildly acidic towards a pH of 5.5 (57,58,70). The characteristic acidification of these vesicles is caused by V-ATPases present in their membrane, that pump H^+ from the cytosol into the lumen of the vesicle (71). In order to prevent excessive acidification, Cl^- channels counteract too low pH levels (72).

ii. Endosomes and lysosomes

In order to recycle parts of the plasma membrane and/or to take up extracellular components cells also undergo endocytosis (73). The endocytic pathway consists of several compartments, namely early endosomes (EEs), late endosomes (LEs) and lysosomes, however, all of these vesicular subpopulations fulfill different roles (74). In the early stage of endocytosis, the plasma membrane buds mainly at clathrin coated regions to from a vesicular structure (75). However, the destination of these vesicles is quite diverse. The newly formed vesicles deliver the cargo to EEs, which, in turn, are responsible for either recycling the cargo directly back to the membrane or for delivering the content to recycling endosomes, that are capable of traveling toward the membrane for re-use of the delivered content (76–80). However, not all cargoes located within EEs are recycled back to the plasma membrane. Upon conversion of the EE to the more acidic LE, possessing pH values of 5.5, the cargo is delivered towards the perinuclear region with high lysosomal density (81). Eventually, the endosomal membrane might form intravesicular vesicles (ILVs) by budding inward or by fusion with other endosomes to generate multivesicular bodies (MVB). As a result of the increasing number of ILVs, the endosomes grow and go through further maturation for final fusion with highly acidic lysosomes (82–84). This fusion creates endo-lysosomal vesicles with highly acidic pH values, which is essential for the activity of lysosomal hydrolases (66,85). After successful degradation, the remaining lysosome represents a storage pool for hydrolases and membrane components (86).

1.2 Lysosomes and their involvement in autophagy

One major cellular pathway that is dependent on lysosomes and acidic pH is represented by autophagy (87). Cells usually possess sophisticated sensing mechanisms to recognize nutrient availability and glucose levels that are important to guarantee ATP production (88,89). Conditions where the extracellular glucose concentration or nutrient availability is restricted or even diminished would lead to a severe metabolic crisis of cells (90). To counteract such nutrient shortages, cells are capable of generating essential cellular building blocks for cell metabolism and energy production by autophagy (91).

As a result of ongoing starvation, the mammalian target of rapamycin (mTOR), a central energy sensor within the cell, is inhibited, leading to autophagy induction via a highly organized signaling cascade (92,93). At the end of this process, the interplay of different autophagy related genes (ATG) and the microtubule-associated proteins 1A/1B light chain 3B (LC3B) results in the formation of an autophagosomal vesicle that either carries selected or random cargo destined for degradation (94–97). During autophagic flux, the neutral autophagosomes fuse with acidic lysosomes in order to degrade the intravesicular components, finally leading to the production of energy for the cell and its metabolic processes (91).

1.3 Role of V-ATPase in vesicular acidification

Acidic pH values are a hallmark of intracellular vesicles and the Golgi complex. Responsible for the acidification are ion channels and pumps that are located within the membrane, as they facilitate the accumulation of H^+ within the Golgi and vesicles, thereby acidifying the lumen. However, their localization is not limited to vesicles, hence, they can be found within different intracellular membranes. One prominent candidate is the well described V-ATPase, a multi-subunit complex with diverse composition, depending on the compartment (98,99). In general, the H^+ pump consist of two big parts, the membrane sector V_0 and the catalytic sector V_1 subunit. While the V_0 subunit is located within the membrane, the V_1 subunit acts as a peripheral complex without integration into the vesicular bilayer. Together, these subunits cause vesicular lumen acidification (98). The V_0 subunit is responsible for H^+ translocation across the membrane, while V_1 hydrolyses ATP, thereby generating the force needed to pump H^+ inside the compartment (100). However, the different pH levels of compartments possessing V-ATPases might be regulated by their density within the membranes. According to that theory, the Golgi complex is likely to have less V-ATPases within the Golgi membrane than vesicles that are capable of acidifying their lumen to a higher extend (60). However, direct evidence of different H^+ pump densities are largely missing, possibly also due to the constant dynamic release and uptake of vesicular structures. While it is still questionable, whether the pump density is responsible for the wide pH range throughout the secretory pathway, also the activity of V-ATPases might be regulated by intrinsic signals. Experiments performed in the past would, therefore, explain the different $[H^+]$ found in secretory vesicles as a result of assembly and disassembly of the V_0 and V_1 subunit. The first experiments suggesting that the V_0 and V_1 subunit assembly could be the missing link were performed in yeast, where a high rate of disassembly of the V_0 and V_1 subunits was described upon glucose removal (101). In general, V-ATPase activity also seems to be regulated by various other means, as aldolase activity was described to regulate V-ATPase expression (102).

Binding of the “regulator of the H^+-ATPase of the vacuolar and endosomal membrane” (RAVE) complex to the V_1 subunit, as well as redox changes are thought to act as regulatory mechanisms (103,104). Nowadays, several V-ATPase inhibitors are available (105). However, one of the most commonly used inhibitors is bafilomycin-A (Baf-A), a macrolide antibiotic that inhibits the V-ATPase and prevents H^+ from entering the vesicles (106–108). Bowman et al. firstly described in 1988, that Baf-A was suitable to differentiate between different ATPase enzymes, as they reported that Baf-A only inhibited the V-ATPase. Hanada et al. suggested that the binding site of Baf-A is located within the V_0 complex (109). These hypothesis was confirmed by other groups, as they showed that Baf-A inhibited H^+ flux through the V_0 complex, whereas the H^+ pump activity could be restored upon addition of excess V_0 (110,111).

1.4 Cellular pH dyshomeostasis

While the tight regulation of pH_i is important for every cell, especially pH_i dysregulations in neurons have been described in more detail, since several commonly known diseases that affect a great percentage of the population are related to an altered neuronal pH homeostasis (112,113). Hence, understanding the molecular mechanisms behind these diseases is extremely important in order to design and develop valuable treatment strategies (114).

Considering neuronal excitability, alkaline pH values in the brain are thought to increase the excitability, while acidification has been reported to have the contrary effect (115). However, one must take several factors into account that eventually promote disease conditions. As an example, it has been reported that mild levels of cytosolic acidosis (pH 7.0 to 6.5) even seem to reduce neuronal cell death induced by glutamate and might decrease ischemic injury (116,117). Only some of many examples of diseases that are associated with dysregulated neuronal activity are multiple sclerosis, PD and AD (112,113,118). The effective clearance of amyloid beta peptides is dependent on functional degradation within neurons (119). These mechanisms seem to be impaired during Alzheimer’s disease, as a downregulation of the Na^+/H^+ exchanger NHE6 has been reported to be responsible for increased endosomal acidification. Methods to restore NHE6 expression could, therefore, represent a target for the effective degradation of amyloid beta, thereby preventing the disease or serving as an effective treatment strategy (120). While alkaline pH is known to prevent apoptosis in cells, acidification directly promotes cell death (121). Ibaretta et al showed that an acid load effects lymphoblasts from AD patients to a greater extent than control cells. This would lead to the hypothesis that the H^+ buffering capacity and the extrusion of H^+ might be impaired in AD, finally causing increased cell death (8).

1.5 Cell metabolic activity affects extracellular pH

Many different metabolic processes are capable of producing H^+ that eventually could lead to decreased pH_{ex}. Especially skeletal muscle and adipose tissue cells represent cells of high glycolytic activity, thereby producing high amounts of lactic acid (122–124). Eventually, due to the low acid dissociation constant (pKa), lactic acid dissociates to lactate and H^+ that can be released from the cell via H+ transporters (125). While lactate is the main source of extracellular acidification during glycolysis, also CO_2 generated during respiration is an alternative cause of extracellular acidification. Upon conversion to carbonic acid (H_2CO_3), which dissociates to HCO_3^- and H^+, CO_2 might contribute to extracellular pH (pH_{ex}) alterations (29). While high lactate production might be a normal event within cells like skeletal muscle cells, excessive lactate production and secretion is furthermore a hallmark of cancer cells (126,127). Especially tumor cells mainly produce energy via glycolysis, a process known as Warburg effect, which causes elevated intracellular lactate levels (128,129). Extrusion of lactate and H^+ by the previously mentioned transporters inevitably leads to an increase of pH_i and an acidification of the pH_{ex} within the tumor microenvironment (TME), which in turn has been described to be beneficial for cell proliferation, metastasis formation and treatment resistance (130–132). The control and re-establishment of dysregulated pH levels, therefore, seems to be a promising target for novel therapies. Hence, measuring pH and other ions within local extracellular fluids is of utmost importance to better understand complex networks and their interplay

1.6 Genetically encoded pH sensors

Over the last years, many genetically-encoded sensors have been developed to measure a plethora of different ions and metabolites. Besides probes sensitive for calcium ions (Ca^{2+}), K^+, magnesium ions (Mg^{2+}) or ATP, also several pH sensors have been developed (133–136). pH sensors can either work as single fluorescent protein (FP)- or double FP-based sensors (11,137). The use of intensiometric single FP-based sensors rather allows the detection of pH changes in a qualitative manner, as the quantitative determination of pH changes is challenging due to the absence of a normalization reference (138). However, some single FP probes provide and allow a ratiometric read-out that is either ratiometric by excitation or by emission (138,139). Such principles allow the determination of pH values and their changes. Nonetheless, probes relying on the Förster resonance energy transfer (FRET) principle still represent the gold-standard of genetically-encoded probes, due to their facile calibration (137,140). Mostly the FRET donor is represented by a cyan fluorescent protein (CFP) or a green fluorescent protein (GFP), while yellow fluorescent proteins (YFP) and red fluorescent proteins (RFP) act as FRET acceptors (141).

Usually the donor and acceptor are connected via an ion- or analyte binding domain that is capable of binding the analyte of interest in a highly specific and sensitive manner. Upon binding, the domain usually undergoes a conformational change, yielding a reduction of the distance between the FPs. As a consequence, the donor fluorescence emission decreases, while the FRET emission increases (134,136). In contrast to sensors containing a specific analyte binding domain, the most commonly used FRET-based pH sensors are not dependent on conformational changes. In contrast, these sensors consist of one pH sensitive and one pH insensitive FP. Due to a quench of the fluorescence ability of the pH sensitive FP upon protonation, FRET changes can be detected and serve as a read-out for pH alterations (137,142).

The first genetically-encoded pH probe, pHluorin, was introduced by Miesenböck and colleagues (138). The ratiometric GFP derived probe was used as a reporter for fusion of vesicles with the plasma membrane upon secretion. Due to the acidic pH within secretory vesicles, the GFP fluorescence is quenched during transport, while fusion with the plasma membrane and release into the neutral extracellular space caused a dramatic increase of the fluorescence (138). Considering mitochondrial pH levels, the YFP derived probe SypHer is perfectly suitable to detect pH changes within mitochondria, due to its relatively high pKa of 8.0 (11). Recently, two improved SypHer variants were introduced, while especially the third generation, Sypher3s, displays enhanced brightness and a big dynamic range (143,144). Another frequently used probe for pH_i measurements is pHRed, a red fluorescent variant that was developed by Tantama et al, possessing a pKa around 6.6 (145). pHRed was targeted to mitochondria and measured in combination with a cytosolic ATP/ADP ratio sensor to examine the link between cell metabolism and mitochondrial pH levels (145). Besides pHRed, pHTomato represents another red shifted pH probe that facilitates multi-color imaging due to only one excitation wavelength (146).

An example of a FRET-based pH indicator was developed by Esposito and colleagues using the ECFP-EYFP FRET-pair for the determination of acidic to neutral pH values (137). They used a construct named Cy11.5 as a template for the generation of different pHlameleon variants with pKa values from 5 to 7. However, the applicability of these FRET-based indicators upon targeting to distinct subcellular compartments remains elusive (137).

1.7 Strategies for extracellular sensor immobilization

Considering the extracellular acidification caused by metabolic activities of cells, measuring pH_{ex} might help to design and generate novel approaches to counteract or stabilize cellular pH homeostasis. However, many pH indicators have only been used for the determination of pH_i values so far (137,147). In order to precisely measure pH_{ex} close to the cell membrane, sensors need to be located near the plasma membrane facing the extracellular space. In theory, this can be achieved using different approaches.

One possibility to locate sensors at the outer side of the plasma membrane is the addition of a glycosylphosphatidylinositol (GPI) anchor (148,149). Such targeting can be achieved by the addition of the cadherin 13 (CDH13) membrane targeting sequence on the N-terminal end, while the sequence for a GPI-anchor is added at the C-terminal end of a sensor (149,150). Expression of such constructs should result in glycosylation of the GPI-anchor within the ER with further transport to the Golgi. Secretory vesicles, emanating from the Golgi complex transport the construct to the plasma membrane, where the GPI-anchor inserts at the outer side (149,150). In theory, every transmembrane protein that has at least one terminus located toward the extracellular space could potentially serve as a carrier for the pH sensor (151). However, it is much more complex, since overexpression of huge transmembrane proteins could possibly disturb the membrane flexibility and impair normal cell homeostasis (152,152). Hence, the choice of a targeting sequence that affects the cell physiology and morphology only by minimal ways is essential to obtain meaningful results.

Besides expression of the construct, sensors can also be “loaded” onto the cell surface. Recently, a sophisticated method based on membrane insertion has been described, comprising a pH low insertion peptide (pHLIP) (153). Anderson and colleagues used this method to locate a pH sensing chemical dye to the plasma membrane. The pHLIP peptides benefit from their characteristic of membrane insertion in a pH dependent manner.

Slightly acidic pH results in protonation of asparagine and glutamine residues within the peptide, thereby increasing its hydrophobicity. The low pH helps membrane associated folding with subsequent membrane insertion of the peptide. Finally, the N-terminal end is located within the extracellular space, while the C-terminal end is located within the cytosol. The dissociation of the peptide has been described to be very low, even if the pH is raised again (153).

Immobilization of fluorescein isothiocyanate (FITC), a chemical pH probe, has already been achieved by using an amphiphilic polymer. The poly(ethylene glycol) (PEG)-phospholipid is spontaneously inserted into the cell membrane due to its hydrophobic alkyl chains (154).

Another method for targeting the cell membrane is represented by Ke and colleagues, who used lipid-DNA consisting of a hydrophobic diacyl-lipid part and a hydrophilic DNA, fused to a pH sensitive dye (155). Interaction of the membranous phospholipids with the hydrophobic tail of the constructs thereby results in immobilization of the probe at the plasma membrane. Due to the hydrophilic structure, the DNA fused to the probe is outward-facing the extracellular space (155).

One further well-known possibility for immobilization represents the biotin-avidin interaction (156). This technique has already been used for co-immunoprecipitation, pull-down assays as well as for biotinylated antibodies, to target cell surface receptors (157–159). However, some recently developed techniques exploited the strong non-covalent bond of biotin and avidin also for immobilization of quantum dots on the cell surface (160). To achieve high biotinylation rates of the plasma membrane, the use of a biotin acceptor peptide (AP) is highly advantageous. While several different peptides exist, the 15 amino acids long AviTag is probably the most frequently used AP (161,162). If the AviTag is fused to, for example, a transmembrane protein, the peptide is exposed at the cell surface for further biotinylation using the recombinant purified *Escherichia coli* (*E.coli*) biotin ligase (BirA) enzyme, that can be added to the extracellular medium in order to biotinylate the AviTag (160).

In contrast to adding purified BirA to the cells, several groups reported that BirA targeted to the ER very efficiently biotinylates the AP, if both proteins are present within the ER lumen (163,164). Co-expression of the AP fused to a membrane leading sequence together with ER-targeted BirA, therefore, leads to biotinylation of the AP in the ER lumen, subsequent transport to the Golgi and packaging into secretory vesicles. When reaching the cell surface, the biotin located at the AP is exposed to the extracellular space and can be bound by the avidin counterpart (163,164). Besides avidin, also streptavidin and traptavidin are capable of binding to biotin. Considering the high thermo- and pH-stability, streptavidin features some advantages compared to avidin (165,166). Recently developed traptavidin has been described to feature even lower dissociation rates over a long time and a high temperature and pH stability (167).

The fact that genetically-encoded probes are suitable to measure extracellular analyte alterations as recombinant proteins has been demonstrated recently (134). Nonetheless, they have never been applied after immobilization, which would drastically enhance our understanding of local ion and analyte alterations.

2 Materials and Methods

Parts of this section are reproduced in part or modified with permission from Burgstaller et al., 2019 © American Chemical Society (176)

2.1 Chemicals, Buffers and Solutions

2.1.1 Chemicals

Agar–Agar Kobe I, Bacterial Protease Inhibitor Cocktail, $CaCl_2$, D-Glucose, HCl (30%), HEPES, KCl, KH_2PO_4, $MgCl_2$, NaCl, NaH_2PO_4, NaOH, Triton X-100, Trypton/Pepton, and Yeast Extract were purchased from Carl Roth (Graz, Austria). Agarose was purchased from Carl Roth (Graz, Austria). β-D-1-thiogalactopyranoside (IPTG), Bafilomycin-A, Benzonase Nuclease, Biotin, Dulbecco´s Modified Eagle's Medium (DMEM), Gramicidin, Imidazole, Isopropyl-Beta-D-Thiogalactoside (IPTG), Monensin, 2-(N-Morpholino)Ethanesulfonic Acid (MES), NaN_3, NH_4Cl, 3-(N-Morpholino) Propanesulfonic Acid (MOPS)), *N*-Methyl-D-Glucamine (NMDG) and Triton X-100 were purchased from Sigma Aldrich (Vienna, Austria). Fetal calf serum (FCS), Fungizone, Gibco RPMI 1640 cell culture medium, MEM Glutamax Supplement, MEM Amino Acids, Penicillin, Protino Ni-NTA Agarose, and Streptomycin were purchased from ThermoFisher Scientific (Vienna, Austria). Nigericin was purchased from Tocris (Abingdon, United Kingdom).

2.1.2 Buffers used for protein purification

Buffer formulations to purify recombinant proteins expressed in *E.coli* were as followed: Lysis buffer (in mM): 150 NaCl, 100 Na_2HPO_4, 10 Imidazole, 250 units Benzonase Nuclease, 100 µl of Bacterial Protease Inhibitor Cocktail (diluted according to the manufacturer's protocol), pH 8.0. Washing buffer 1 (in mM): 100 Na_2HPO_4, 150 NaCl, 20 Imidazole, pH 8.0. Washing buffer 2 (in mM): 100 Na_2HPO_4, 1000 NaCl, 20 Imidazole, pH 8.0. Purification buffer (in mM): 100 Na_2HPO_4, 150 NaCl, 300 Imidazole, pH 8.0. Elution buffer for size exclusion chromatography (SEC buffer) for recombinant pH-Lemon variants (in mM): 10 HEPES, 0.05% Triton X-100, pH 7.3 with *N*-Methyl-D-Glucamine (NMDG). SEC buffer for recombinant Traptavidin-fusion constructs (in mM): 10 HEPES, pH 7.3 with NMDG.

2.1.3 Buffers used for the characterization of recombinant sensors

SEC buffers with different pH values containing Triton X-100 were used for the characterization of the recombinant purified sensors pH-Lemon (=mTurquoise2-EYFP), EYFP-mTurquoise2, mTurquoise2-EYFP-mTurquoise2 and SypHer. To characterize traptavidin-pH-Lemon, pH buffers without Triton X-100 were used. SEC buffers containing different concentrations of K^+, were used for *in vitro* measurements of traptavidin-GEPII 1.0. To obtain different [K^+], KCl was added to SEC buffer. 10 mM MES was used for the adjustment of pH values below 5.5, and 10 mM MOPS was used for adjustment of pH values above 9.0. The pH was adjusted either using HCl or NMDG to different pH levels for the characterization of the pH probes, or to a pH of 7.3 for measurements of the traptavidin-GEPII 1.0-construct.

2.1.4 Buffers used for fluorescence microscopy

Before fluorescence microscopy experiments, all cells expressing pH-Lemon constructs (excluding traptavidin-constructs) were washed and stored for 30 min in a HEPES-buffered solution (storage buffer) containing 138 mM NaCl, 5 mM KCl, 2 mM $CaCl_2$, 1 mM $MgCl_2$, 10 mM HEPES, 2.6 mM $NaHCO_3$, 0.44 mM KH_2PO_4, 0.34 mM Na_2HPO_4, 10 mM D-glucose, 0.1% vitamins, 0.2% essential amino acids, and 1% penicillin–streptomycin, pH adjusted to 7.4 with NaOH. For fluorescence microscopy, a physiological buffer containing (in mM) 138 NaCl, 10 D-Glucose, 5 KCl, 2 $CaCl_2$, 1 $MgCl_2$, pH adjusted to 7.4 with NaOH was used. For the characterization of pH-Lemon variants and SypHer *in situ* regarding their EC_{50} values, 5 µM Nigericin and 10 µM Monensin were added to the physiological buffer and the pH was adjusted using HCl or NaOH to different pH values ranging from 4.0 to 10.0, containing either (in mM) 10 MES (for adjustment of pH <5.5), 10 HEPES (for adjustment of pH 5.5-9.0) or 10 MOPS (for adjustment of pH >9.0). In order to neutralize acidic vesicles, the neutralization buffer was composed of a modified physiological buffer with addition of 0.5% NaN_3 (Sigma Aldrich) and 50 mM NH_4Cl (Sigma Aldrich), pH adjusted to 9.0, NaCl reduced to 80 mM to maintain the osmolarity. Phosphate buffered saline (PBS) was composed of (in mM) 137 NaCl, 2.7 KCl, 10 Na_2HPO_4, 1.8 KH_2PO_4 with the pH adjusted to 7.4.

2.2 Design of sensor constructs

2.2.1 pH-Lemon sensor cloning and subcellular targeting

For cloning procedures, chemically competent 10-beta *E.coli* cells and restriction enzymes purchased from New England Biolabs (Ipswich, MA, USA) were used. To generate differently targeted pH-Lemon variants, primers were obtained from ThermoFisher Scientific. PCR reactions were performed using Herculase II fusion DNA polymerase (Agilent, Santa Clara, USA). For all PCR reactions the manufacturer´s instructions were followed. The plasmid vector pcDNA3.1(-) served as the backbone for the construction of the differently targeted pH-Lemon variants. Addition of the sequence LPPLERLTL (from GP41 human immunodeficiency virus) (**Tab. 1**) using the HindIII-Stop-NES-EYFP_rev and EcoRI-EYFP_for primer pair (**Tab. 2**), led to a cytosolic localized pH-Lemon variant. In order to target pH-Lemon into the lumen of mitochondria, the N-terminus of pH-Lemon was fused to a commonly used mitochondrial targeting sequence derived from COX8 (**Tab. 1**), which was used as a tandem dimeric repeat to improve targeting efficiency. After fusion of the N-terminus of pH-Lemon to the calreticulin (CaR) targeting sequence, and the C-terminus to the ER retention signal (KDEL) (**Tab. 1**), pH-Lemon was targeted into the lumen of the ER. For the generation of the ER-targeted construct, the primers NheI-CaR-mT2_for and HindIII-Stop-KDEL_rev (**Tab. 2**) were used. Fusion of the C-terminal end of pH-Lemon to the outer mitochondrial membrane (OMM) protein OMP25 targeting sequence led to a localization at the OMM **(Tab. 1)**. HeLa cell cDNA was used for cloning of LC3B (**Tab. 1**) into pcDNA3.1(+) as vector backbone (ThermoFisher Scientific) using the primer pair EcoRI-LC3B_for and XhoI-Stop-LcC3B_rev (**Tab. 2**). After fusion of LC3B to the C-terminal end of pH-Lemon, the sensor was targeted to autophagosomes and autolysosomes. mTurquoise2 and EYFP were cloned into the LC3B containing vector using the primers NheI-mT2_for, BamHI-Linker-mT2_rev, BamHI-EYFP_for and EcoRI-EYFP_rev (**Tab. 2**). In order to target pH-Lemon to the outer side of the plasma membrane, a GPI-anchor was used (**Tab. 1**). Therefore, pH-Lemon was flanked with the membrane leading signal (MLS) at the N-terminal end derived from CDH13 and with the GPI-anchor at the C-terminal end (**Tab. 1**). For this purpose, the primer pairs MLS1-XhoI-mT2_for / EcoRI-Linker-mT2_rev, and NheI-MLS2_for / EcoRI-Linker-mT2_rev were used for the amplification of mTurqoiuse2 with the MLS of CDH13 attached (**Tab. 2**). GPI1-KpnI-EYFP_rev / EcoRI-EYFP and HindIII-Stop-GPI2_rev / EcoRI-EYFP primer pairs (**Tab. 2**) were used for the amplification of EYFP, followed by ligation of MLS-mTurquoise2 PCR product into pcDNA3.1(-) vector. All constructs were confirmed for the correctness of their sequence by Sanger sequencing carried out by Microsynth (Vienna, Austria).

Table 1: Nucleotide sequences for cloning different pH-Lemon constructs. Table was reproduced in part and modified from Burgstaller et al., 2019 with the permission of the publisher ACS Sensors.

SENSOR PART	*SEQUENCE*
Glycin-Serine (GS) Linker	GGTGGAGGCGGTAGC
Mitochondrial targeting sequence (MTS)	ATGTCTGTTCTGACTCCTCTGCTGCTCCGGGGTCTCACAGGTTCC GCAAGAAGACTCCCCGTGCCTAGGGCCAAAATTCATTCACTGGG GGACCCCATGAGCGTGCTCACCCCACTCCTGCTGCGGGGGCTGA CCGGCAGCGCTAGGCGGCTGCCAGTCCCCAGGGCCAAGATCCA CAGTCTCGGCGATCCCAAGGATCCACCGGTCGCC
CDH13 leading sequence	ATGCAGCCGAGAACTCCGCTCGTTCTGTGCGTTCTCCTGTCCCAG GTGCTGCTGCTAACATCTGCAGGATCC
GPI-anchor	GACTGCAACGCGGCAGGGGCCCTGCGCTTCAGCCTGCCCTCAGT CCTGCTCCTCAGCCTCTTCAGCTTAGCTTGTCTG
ER targeting sequence	ATGCTGCTGCCCGTCCCCCTGCTGCTGGGCCTGCTGGGCGCCG CCGCC
ER retention site	AAGGACGAGCTG
OMP25 targeting sequence	CGAGGCGACGGAGAGCCGAGTGGAGTTCCTGTAGCTGTGGTGCT GCTGCCAGTGTTTGCCCTTACCCTGGTAGCAGTTTGGGCCTTCGT GAGATACCGAAAGCAGCTC
Nuclear exclusion sequence	TTGCCTCCATTAGAACGATTGACGTTA
LC3B	ATGCCGTCGGAGAAGACCTTCAAGCAGCGCCGCACCTTCGAACA AAGAGTAGAAGATGTCCGACTTATTCGAGAGCAGCATCCAACCAA AATCCCGGTGATAATAGAACGATACAAGGGTGAGAAGCAGCTTCC TGTTCTGGATAAAACAAAGTTCCTTGTACCTGACCATGTCAACATG AGTGAGCTCATCAAGATAATTAGAAGGCGCTTACAGCTCAATGCT AATCAGGCCTTCTTCCTGTTGGTGAACGGACACAGCATGGTCAGC GTCTCCACACCAATCTCAGAGGTGTATGAGAGTGAGAAAGATGAA GATGGATTCCTGTACATGGTCTATGCCTCCCAGGAGACGTTCGGG ATGAAATTGTCAGTG

Table 2: Primers used to generate pH-Lemon constructs. Table was reproduced in part and modified from Burgstaller et al., 2019 with the permission of the publisher ACS Sensors.

PRIMER	*SEQUENCE*
HindIII-Stop-NES-EYFP_rev	TTTAAGCTTATAACGTCAATCGTTCTAATGGAGGCAACTTGTACAG CTCGTCCATGC
EcoRI-EYFP_for	AAAGAATTCATGGTGAGCAAGGGCGA
NheI-CaR-mT2_for	GCTAGCATGCTGCTGCCCGTCCCCCTGCTGCTGGGCCTGCTGGG CGCCGCCGCCGACTCGAG TATGGTGAGCAAGGGCGAGG
HindIII-Stop-KDEL_rev	TGTTAAGCTTACAGCTCGTCCTTCTTGTACAGCTCGTCCATGC
NheI-mT2_for	AAAGCTAGCTATGGTGAGCAAGGGCGA
BamHI-Linker-mT2_rev	AGCGGATCCCGCTACCGCCTCCACCCTTGTACAGCTCGTCCATG
EcoRI-Lc3b_for	AAGGAATTCATGCCGTCGGAGAAGACC
XhoI-Stop-Lc3b_rev	AGACTCGAGTTACACTGACAATTTCATCCCG
BamHI-EYFP_for	AAAGGATCCATGGTGAGCAAGGGCGA
EcoRI-EYFP_rev	TTTGAATTCCTTGTACAGCTCGTCCATGC
GPI1-XhoI-mT2_for	CTGTGCGTTCTCCTGTCCCAGGTGCTGCTGCTAACATCTGCAGGA TCCCTCGAGTATGGTGAGCAAGGGCGAGG
NheI-GPI2_for	AGATCTAGAATGCAGCCGAGAACTCCGCTCGTTCTGTGCGTTCTC CTGTCC
EcoRI-Linker-mT2_rev	AGCGAATTCGCTACCGCCTCCACCCTTGTACAGCTCGTCCATG
GPI1-KpnI-EYFP_rev	CTGAGGGCAGGCTGAAGCGCAGGGCCCCTGCCGCGTTGCAGTC GGTACCCTTGTACAGCTCGTCCATGC
HindIII-Stop-GPI2_rev	AGCAAGCTTACAGACAAGCTAAGCTGAAGAGGCTGAGGAGCAGG ACTGAGGGCAGGCTGAAG

2.2.2 Recombinant pH sensors

Three fusion constructs between mTurquoise2 and EYFP with different orientations of the FPs (mTurquoise2-EYFP = pH-Lemon, EYFP-mTurquoise2, mTurquoise2-EYFP-mTurquoise2) and the pH probe SypHer were ordered from Gene Universal Inc. (Newark, USA) in a pET28a(+) backbone for recombinant protein expression in *E.coli* and protein purification.

2.2.3 Recombinant traptavidin-fusion constructs

Considering the approach of coupling recombinant sensors to surfaces (cells and glass slides), fusion constructs of traptavidin and the respective probe (pH-Lemon or GEPII1.0) were ordered from Gene Universal Inc. Traptavidin was attached via a $(GGGGS)_2$ linker, with traptavidin being located at the N-terminal end of the sensors. The vector backbone of these constructs was pET28a(+) with a His-tag for expression of the constructs in *E.coli* and subsequent purification.

2.3 Protein purification & *in vitro* fluorimetry

2.3.1 Recombinant protein expression and purification

For protein expression and purification, plasmid-DNA was transformed into chemically competent one shot BL21 star (DE3) *E.coli* (ThermoFisher Scientific) using the standard protocol for plasmid transformation according to manufacturer's instructions. The following constructs were transformed for purification: pH-Lemon = mTurquoise2-EYFP, EYFP-mTurquoise2, mTurquoise2-EYFP-mTurquoise2, SypHer, traptavidin-pH-Lemon and traptavidin-GEPII 1.0. One single colony was picked from each transformation from agar-agar plates. The colony was inoculated in 10 mL of LB-media containing 50 µg/mL kanamycin and cultured over-night vigorously shaking. On the next day, the pre-culture was transferred into 1 L of LB medium with 50µg/µL kanamycin. The bacteria were cultivated at 37°C in a shaking incubator (MaxQ 8000 HP Incubated & Refrigerated Shaker, ThermoFisher Scientific) until an OD_{600} of 0.8 was reached. At this point, the protein expression was induced by the addition of 1 mM IPTG and the temperature was changed to 20°C. The time of induction varied depending on the constructs used (e.g. 4 hours of induction were sufficient for pH-Lemon and SypHer, traptavidin-GEPII 1.0 was incubated for 16 hours overnight to guarantee sufficient protein expression). After protein expression for the defined times, cells were harvested by centrifugation at 4°C with 6.000 rpm (Sorvall LYNX 6000, ThermoFisher Scientific).

The pellet was resuspended in 15 mL lysis buffer followed by sonication (QSONICA Ultrasonic Processor; 12 min, 50% amplitude, 1 sec on/off) on ice. After additional 45 minutes of centrifugation at 10.000 rpm and 4°C, the supernatant was applied onto a gravity-based nickel affinity column at a flow rate of 2 mL/minute. After 1 washing step using lysis buffer, the agarose beads were washed twice with washing buffer 1 and washing buffer 2, respectively, followed by the elution of the protein from the nickel column using purification buffer. Using protein concentrator tubes with a molecular weight cut-off of 30kDa (Amicon Ultra-15, Merck Chemicals and Life Science, Vienna, Austria), the protein solution was concentrated via centrifugation at 3.600 rpm at 4°C (Eppendorf centrifuge 5810 R, Eppendorf, Vienna, Austria) to a final volume of 500 µL. This solution was applied onto an ÄKTA™ pure system (GE Healthcare, Vienna, Austria) for further purification via a Superdex Increase 200 10/300 (GE Healthcare) following the manufacturer's instructions and settings for the Äkta as well as for the use of the size exclusion column. SEC buffer was used for the size exclusion step. In order to determine the protein concentration, NanoDrop™ 1000 UV/VIS spectrometer (ThermoFisher Scientific) was used.

2.3.2 Characterization of recombinant proteins

The determination of the EC_{50} values as well as temperature dependencies was performed using a CLARIOstar multi-mode fluorescence plate reader (BMG Labtech, Ortenberg, Germany). All proteins were used at a concentration of 200 nM and diluted with SEC buffer. The characterization of the pH probes was done with SEC buffers of different pH values. The SEC buffers used for the characterization of traptavidin-GEPII 1.0 contained different concentrations ($[K^+]$) with a pH of 7.3. The samples were analyzed using FRET analysis with an excitation at 430 nm ± 10 nm and emission were collected at 475 nm ± 10 nm for mTurquiose2 with a dichroic mirror at 452.5 nm. The FRET emission was detected at 525 nm ± 10 nm with a dichroic mirror at 476.2 nm. Separate excitation of the two FPs was performed at 430 nm ± 10 nm for mTurquoise2 with the emission detected at 475 nm ± 10 nm, dichroic mirror: 452.5 nm. EYFP was excited at 480 nm ± 10 nm with the emission collected at 525 nm ± 10 nm, dichroic mirror: 501.2 nm. FRET emission spectra were generated using an excitation of 413,4 nm ± 8 nm and emissions were detected from 450 nm to 550 nm in 1 nm steps. The emission spectra of EYFP were collected using an excitation at 480 nm ± 8 nm and with the detection of the emission from 510 nm to 580 nm in 1 nm steps. Spectral scans were normalized for the area under the curve (AUC) using GraphPad Prism5 software (California, USA) for analysis.

2.4 Fluorescence lifetime imaging

2.4.1 Fluorescence lifetime imaging spectroscopy in vitro

Characterization of the recombinant purified pH-Lemon was performed using fluorescence lifetime imaging microscopy (FLIM) on a time-resolved fluorescence spectrophotometer. The spectrophotometer Fluotime 100 (Picoquant, Berlin, Germany) is based on a PicoHarp300 unit (TCSPC-based). The microscope is equipped with a pulsed diode laser (LDHC440; λ_{exc} = 440 nm; 50 ps pulse width; 20 MHz repetition frequency) as the excitation source and a photomultiplier for single photon detection. The emission of mTurquoise2 and EYFP were detected at 475 nm and 530 nm, respectively.

2.4.2 Fluorescence lifetime imaging microscopy in situ

Characterization of pH-Lemon using FLIM was performed on an upright fluorescence microscope obtained from Nikon (A1 MP; Nikon, Amsterdam, The Netherlands) equipped with a water immersion objective (25x; NA1.1; WD 2 mm; Nikon). The illumination of the pH-Lemon donor mTurquoise2 was achieved by a train of 100 fs light pulses (λ_{exc} = 880 nm; 80 MHz; Mai Tai DeepSee HP, Newport Spectra Physics; Irvine, California). A Galliumarsenidphosphide (GaAsP) hybrid photodetector (HPM-100-40; Becker & Hickl, Berlin, Germany) was used to detect the fluorescence signals that passed a band-pass filter at 445 +/- 45 nm (445BP90, Omega Optical, Brattleboro, VT, USA). Multi-dimensional time-correlated single photon counting (TCSPC) employing TCSPC electronics (SPC-152; Becker & Hickl) was used to generate the decays of fluorescence intensities in every pixel. Plotting the amplitude weighted average fluorescence lifetime tau_ave was used to generate color coded values. Least-square minimizing-based fitting of a biexponential fitting curve was used to obtain tau_mean. The function was re-convoluted with the instrument response function for a proper description of the time course of the pixel fluorescence intensity decays. For FLIM experiments, cells were trypsinized and seeded on poly-L-lysine coated (0.1 mg/mL) coverslips.

2.5 Wide-field imaging microscopy

An inverted and advanced fluorescent microscope was used for wide-field live-cell imaging of pH-Lemon and SypHer *in situ* as well as traptavidin-pH-Lemon. The microscope was equipped with x40 or x100 magnification objective (EC Plan-NEO FLUAR x40; alpha Plan FLUAR x100, Zeiss, Göttingen, Germany) and a motorized sample stage (TILL Photonics, Gräfelfing, Germany). Images were acquired using the charge-coupled device (CCD) camera AVT Stingray 25 F145B (Allied Vision Technologies, Stadtroda, Germany) with a binning of 2 or 4. Excitation was set at 430 nm and emissions were collected at 475 nm and 525 nm, respectively, for FRET imaging of pH-Lemon. In order to measure pH-Lemon with illumination of both FPs separately, CFP and YFP were excited at 430 nm and 500 nm, respectively, with emissions collected at 475 nm and 525 nm. Live acquisition 2 (TILL Photonics) was used for the acquisition of measurements and device control. Measurements of traptavidin-GEPII 1.0 were performed at the TILL microscope described above and at an OLYMPUS IX73 inverted wide-field microscope (OLYMPUS, Vienna, Austria), which was equipped with a 40x (UApo N 340, 40x/1.35 Oil, ∞/ 0.17 / FN22, OLYMPUS) or an 10x objective (UPLXAPO10X, 10x/0.4 Air, ∞/0.17). The microscope was equipped with an OMICRON LedHUB High-Power LED Light Engine as light source with a 455 nm and 505 nm LED for the excitation of CFP and YFP, respectively (OMICRON electronics, Vienna, Austria), as well as 430 nm and 500 nm excitation filters (AHF Analysentechnik, Tübingen, Germany), respectively. The measurements were performed using a binning of 2 or 4 on a Retiga R1 CCD camera (TELEDYNE QIMAGING, Surrey, Canada) attached to an optical beam splitter (DV2, Photometrics, Arizona, USA) to separate the emissions.

2.6 High resolution imaging

High resolution images were acquired using a Nipkow-spinning-disk-based array confocal laser scanning microscope (ACLSM) consisting of a Zeiss Axiovert 200M (Zeiss Microsystems, Jena, Germany) equipped with a x100 objective (α Plan-Fluar x100/1.45 oil objective, Zeiss Microsystems, Jena, Germany). The microscope was equipped with VoxCell Scan® (VisiTech, Sunderland, UK). The light source consisted of an air-cooled argon ion laser system (series 543, CVI Melles Griot, CA, USA). Emission filters ET480/40m (for CFP) and ET525/50m (for EYFP) (Chroma Technologies, VT, USA) were used to detect emitted light during imaging. CFP was excited using 445 nm laser light, while 510 nm laser light was used for YFP excitation. RFP was excited at 561 nm. A CCD camera (CoolSnap HQ2, Photometrics, Tucson, Arizona, USA) was used to acquire emissions at 475 nm, 525 nm and 610 nm (CFP, YFP or mCherry) at a binning of 1, 2 or 4. The system was controlled using VisiView image acquisition and control software (Visitron Systems, Puchheim, Germany).

2.7 Cell cultivation and transfection

Cell culture materials were purchased from Greiner Bio-One (Kremsmünster, Austria). DMEM medium for the cultivation of HeLa and HEK-293 cells (ATCC, Wesel, Germany) contained 10% FCS, 100 U/mL penicillin, 100 µg/mL streptomycin, and 2.5 µg/mL, fungizone (ThermoFisher Scientific). HEK-293 cells for FLIM imaging were grown in DMEM with MEM Glutamax supplement, 10% FCS, 1% (v/v) antibiotics/antimycotics, and 1% (v/v) non-essential amino acids (ThermoFisher Scientific). INS-1 832/13 (INS-1) cells (gift from C.B. Newgard, Department of Pharmacology and Cancer Biology, Duke University School of Medicine, USA) were cultivated in Gibco RPMI 1640 medium purchased from ThermoFisher Scientific. For the cultivation of all cell lines, a humidified incubator with 37°C and 5% CO_2 was used. PolyJet (SignaGen Laboratories, Rockville, USA) transfection reagent was used to transfect HeLa cells according to the manufacturer's protocol 48 hours before measurements in a 3:1 ratio (mixture of 3 µL PolyJet with 1 µg DNA). TransFast purchased from Promega (Madison, USA) was used for the transfection of HEK-293, INS-1 with pH-Lemon – GPI and HeLa cells with pH-Lemon - LC3B. 2,5 µL TransFast and 1,5 µg plasmid DNA were added to a modified DMEM medium without serum. After 4 hours, the transfection medium was replaced with fresh DMEM or Gibco RPMI 1640 media. In order to transfect cells used for FLIM imaging experiments, 2 µg of plasmid DNA were transfected into HEK-293 using a modified calcium-phosphate method (168). For expression of the biotinylated AviTag on the cell membrane, cells were either transfected using PolyJet transfection or infected via an Adenovirus serotype 5 (AV5) obtained from VectorBuilder (Neu-Isenburg, Germany). Conventional transfection was done by co-tansfecting the biotinylase and the GPI-anchored AviTag. For viral infections, a virus encoding for both constructs (the ER-targeted BirA and the GPI-targeted Avitag) separated via an internal ribosome entry site (IRES) was designed and used at a MOI of 50 and incubated in DMEM for 24 hours 2 days prior measurement. Independent of the method of transduction, all cells expressing BirA were supplemented with 10 µM biotin. Co-localization of pH-Lemon - GPI with the Golgi apparatus and intracellular vesicles was analyzed by co-transfecting cells with pH-Lemon and mCherry-Golgi-7, which was a gift from Michael Davidson (Addgene plasmid # 55167). For cell fixation, HeLa cells were washed 3 times with PBS, followed by 10 minutes incubation at room temperature with PBS containing 3.7% paraformaldehyde. After 3 additional washing steps cells were kept in PBS for imaging.

2.8 Cell treatments

2.8.1 Starvation of cells

For autophagy induction, cells were washed with PBS twice to remove the nutrients and starved for 2 hours in nutrient free salt-buffer ("physiological buffer") containing 2 mM D-glucose at 25°C.

2.8.2 Neutralization of endosomal vesicles

Vesicles were either neutralized using incubation with neutralization buffer (see chapter "Buffers & Solutions") for 5 minutes or pre-incubation with 0,5 µM Baf-A in DMEM for 70 minutes at 37°C (for the subsequent experiments, Baf-A was present in every buffer).

2.8.3 Acidic compartment staining

LysoTracker Red DND-99 (ThermoFisher Scientific) was used for 30 minutes at 37°C at a final concentration of 75 nM. After the staining procedure, cells were washed 2 times with PBS prior to analysis.

2.9 Calibration of pH-Lemon constructs

2.9.1 Calibration of pH-Lemon - cyto

HeLa cells were transfected with the cytosolic pH-Lemon 48 hours prior measurements. To ensure effective permeabilization, the cells were pre-incubated in a physiological buffer containing 5 µM nigericin and 10 µM monensin. For titration of the cytosolic pH-sensor, buffers with different pH values (as described in the section "Buffers used for fluorescence microscopy") with additional 5 µM nigericin and 10 µM monensin were perfused using the gravity-based perfusion system (NGFI, Graz, Austria).

2.9.2 Calibration of pH-Lemon - GPI

HeLa cells were transfected with pH-Lemon-GPI 48 hours prior to measurements. Cells were perfused using a gravity-based perfusion system (NGFI). Extracellular buffers possessing a pH of 4.0 and 10.0 were perfused to record the minimum and the maximum response of the sensor. Respective maximal and minimal ratio signals of the cell surface of single cells were used to define pH values according to formula

$$pH = K_D * (\frac{Ratio - Ratio_{min}}{Ratio_{max} - Ratio})$$

2.10 Application of buffers and substances

2.10.1 Application by hand

The application of NaN_3 and NH_4Cl for ACLSM measurements was done via injection by hand to cells grown in 35 mm µ-dishes (Ibidi, Gräfelfing, Germany).

2.10.2 Application via gravity-based perfusion system

A gravity-based perfusion system (NGFI) was used for titrations, therefore cells were grown on 30 mm circular glass slides (Paul Marienfeld GmbH, Lauda-Königshofen, Germany). For fast and precise buffer exchange, the perfusion system was connected to a perfusion chamber fitting the glass slides (NGFI). A vacuum pump (Chemistry diaphragm pump ME 1c, Vacuubrand, Wertheim, Germany) was connected to ensure laminar buffer flow.

2.10.3 Application via BioPen® SYSTEMS - Fluicell

Cells seeded in 35 mm µ-Dishes or on 30 mm circular glass slides were covered with physiological buffer to prevent them from drying. Via a micromanipulator (Sutter MP-225, Sutter Instruments, California, USA), the tip of the microperfusion system (BioPen, Fluicell, Mölndal, Sweden) was inserted into the liquid and positioned near the cells that should be perfused. The device was used in order to apply the recombinant traptavidin-construct proteins to the cell surface as wells as to couple glass surfaces.

2.11 Traptavidin-Biotin coupling

2.11.1 Coupling of Traptavidin constructs on the cell surface

In order to bind traptavidin to the biotinylated cell surface, the cells were washed five times with PBS. The recombinant proteins were diluted to a final concentration of 8 µM with the respective x-times stock of PBS, in order to maintain buffer osmolarity. For the acquisition of high-resolution images, cells were grown in 8-well µ-Slides (Ibidi) and were incubated with 200 µL of the diluted recombinant protein for 40 minutes in the dark at 25°C followed by 5 washing steps using PBS to remove excess protein. The cells were then kept in physiological buffer for imaging. Single cell coupling was performed using the BioPen. Therefore, cells were perfused with the 8 µM protein solution for 10-20 minutes. Afterwards the tip was removed and the cells were kept in physiological buffer for 30 minutes to reduce background signal by dissociation of unspecifically bound protein. The subsequent exchange of different pH or K^+ buffers was performed using the gravity-based perfusion system (NGFI).

2.11.2 Coupling of traptavidin constructs on glass slides

Biotinylated 30 mm circular glass slides were purchased from Microsurfaces Inc. (New Jersey, USA) and stored sterile at -80°C in argon environment. To bind traptavidin-sensors onto the glass surface, either 600 µL protein solution was added on top of the glass surface at 25°C for 40 minutes or the BioPen was used to perfuse the biotinylated glass slides for 40 minutes. After coupling, the glass slide was washed 5 times with PBS and kept in physiological buffer for 30 minutes to allow unbound protein to dissociate prior to imaging. For the subsequent imaging experiment, a gravity-based perfusion system was used (NGFI).

2.12. Data analysis & statistical analysis

Obtained data were analyzed using Excel (Microsoft, Washington, USA), MetaMorph (Molecular devices, California, USA) and GraphPad Prism 5 Software. Pseudo-colored ratio images were generated using MetaMorph software. Ratio scale was set as demonstrated in the figures. For data visualization, CorelDraw was used. Images generated using ACLSM were adjusted in light and contrast (+40%/+40%). For the calculation of the EC_{50} values of recombinant pH proteins, the FRET (or YFP) fluorescence was divided by the mTurquoise2 fluorescence. Since 100% of the EYFP fluorescence were quenched at a pH of 4.0, dividing FRET/mTurquoise2 avoided a mathematically incorrect division by 0.

3 Aims and Objectives

Based on the importance of the intra- and extracellular pH homeostasis of cells and within organisms, we aim

1) **To develop a genetically-encoded, FRET-based probe suitable for (local) pH imaging.**

The probe should thereby meet all criteria of highly sophisticated, state-of-the-art FRET-based indicators, including a high signal-to-noise ratio, reversible, fast and reliable reporting of pH alterations and should be suitable to visualize intra- and extracellular pH levels. Therefore, a pKa close to 7.0 measuring a wide pH range is advantageous. The probe will extensively be characterized *in vitro.* After the *in vitro* identification of suitable candidates, we will

2) **Target and express the pH sensor to subcellular compartments including the ER, mitochondria, the outer mitochondrial membrane, the cytosol and acidic vesicles of single living cells.**

Within these organelles we aim to visualize and quantify subcellular pH levels using the FRET-based pH sensor.

Furthermore, pH alterations are of major interest within the TME. Hence, we aim to

3) **Target the pH-sensor to the extracellular side of the plasma membrane to visualize local extracellular pH alterations on the surface of cancer cells.**

Besides the expression of the pH probe and its targeting to the outer side of the plasma membrane, we aim

4) **To develop and establish procedures for a selective immobilization of recombinant purified biosensor proteins on the plasma membrane.**

Furthermore, such new immobilization strategies of highly specific genetically-encoded probes is of great interest in biotechnological or medical applications. Thus, we furthermore aim

5) **To immobilize recombinant purified biosensor proteins on inorganic surfaces, which will allow to quantify analyte concentrations within biological fluids.**

4 Results

4.1 EYFP fluorescence is sensitive to pH

In order to generate a pH sensor, that covers a wide range of pH values, we decided to test two FPs with highly contrary pH sensitivities, namely mTurquoise2 and EYFP, for their suitability to function as a pH sensor (15,169,170). Both FPs are monomeric, have a quite fast maturation time of 33 min and 9 min, respectively, and therefore seemed to be promising candidates for the design of a pH reporting construct (171). Importantly, EYFP has a high pKa of 6.5, which makes it extremely sensitive for protonation (170,172). In contrast, mTurquoise2 has an extremely low pKa of 3.1, which, in theory, should prevent the FP from a loss of fluorescence upon acidification (169). To investigate these characteristics of the two FPs we transfected HeLa cells either with mTurquoise2 or EYFP, respectively. In order to investigate the pH dependency of the fluorescence emission of the two FPs, we permeabilized cells expressing the FPs using a combination of the K^+/H^+ antiporter nigericin and the Na^+/H^+ antiporter monensin to adjust the intracellular pH using extracellular buffers (173–175). Upon switching the pH from alkaline towards acidic, the fluorescence emissions of mTurquoise2 and EYFP were recorded using a wide-field microscope. In line with the proposed pKa of mTurquoise2, the fluorescence intensity remained almost unaffected over-time from a pH range of 10.0 to 4.0. (**Fig. 1a**)(169,176). Contrary, the fluorescence emission of EYFP was strongly affected by the increasing protonation of the FP, resulting in a decline of the fluorescence (**Fig. 1a**), which was almost completely quenched at a pH of 4.0 (**Fig. 1a**)(176). Plotting the fluorescence intensity values determined upon perfusion with buffers of distinct pH against the pH values resulted in EC_{50} curves for mTurquoise2 and EYFP. Due to the pH sensitivity of EYFP, the EC_{50} was determined to be 6.3, which is close to the previously described EC_{50} value (Fig.1b)(172,176). While EYFP has lost 50% of its fluorescence at a pH of 6.3, the loss of mTurquoise2 fluorescence was negligible at that pH level (Fig.1b). Due to the pH stability of mTurquoise2 over an extremely wide pH range, the FP had lost only ~10% of its fluorescence at a pH of 4.0 (**Fig. 1b**)(176). Based on these contrary characteristics of mTurquoise2 and EYFP we hypothesized, that a combination of these two FPs will result in a suitable pH sensor for measuring in the acidic to neutral range.

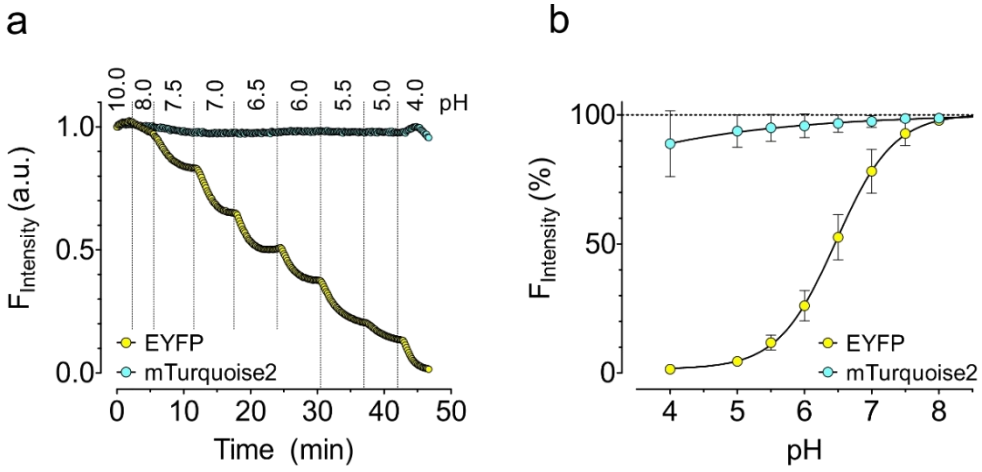

Figure 1: pH sensitivity of mTurquoise2 and EYFP. mTurquoise2 and EYFP expressed in HeLa cells, respectively, were analyzed regarding their pH sensitivity. For the adjustment of intracellular pH values and subsequent pH titration, cells were permeabilized using nigericin and monensin. **(a)** Representative normalized single cell fluorescence responses over-time of mTurquoise2 (cyan dots) and EYFP (yellow dots). Cells were analyzed using fluorescence wide-field microscopy and buffers with different pH as indicated in the panel (black numbers on top of the graph) were exchanged using a perfusion system to adjust intracellular pH levels (n=3 for both FPs). **(b)** Concentration response curve in percentage of the remaining fluorescence intensity of the two FPs against the respective pH value resulted in the generation of EC_{50} curves for mTurquoise2 (blue circles) and EYFP (yellow circles). Initial fluorescence value at pH 8.0 was set as 100% fluorescence intensity and is indicated with black dotted line (n=3 for both, average ± SD). Reproduced in part & modified with permission from Burgstaller et al., 2019; © American Chemical Society

4.2 Fusion constructs of mTurquoise2 and EYFP respond to pH alterations in a ratiometric manner

Due to the advantageous, fluorescence properties of mTurquoise2 and EYFP, we aimed to test different fusion constructs of these proteins for their suitability to report pH alterations. Within these constructs, mTurquoise2 acts as the FRET donor, while EYFP represents the FRET acceptor (176). Most genetically-encoded, FRET-based sensors rely on conformational rearrangements upon ion or analyte binding, thereby in- or decreasing FRET-ratio signals (90,177). In contrast to these ion binding probes, the sensitivity of pH sensors is not based on a change in the conformation and distance between the FRET donor and -acceptor, but relies on a protonation and the subsequent reduction of the fluorescent ability, leading to decreased FRET (90,137). Therefore, we hypothesized that the critical step in the design of a suitable pH probe might be the distance between the two FPs, which should be reduced to a minimum to ensure high FRET efficiency (178).

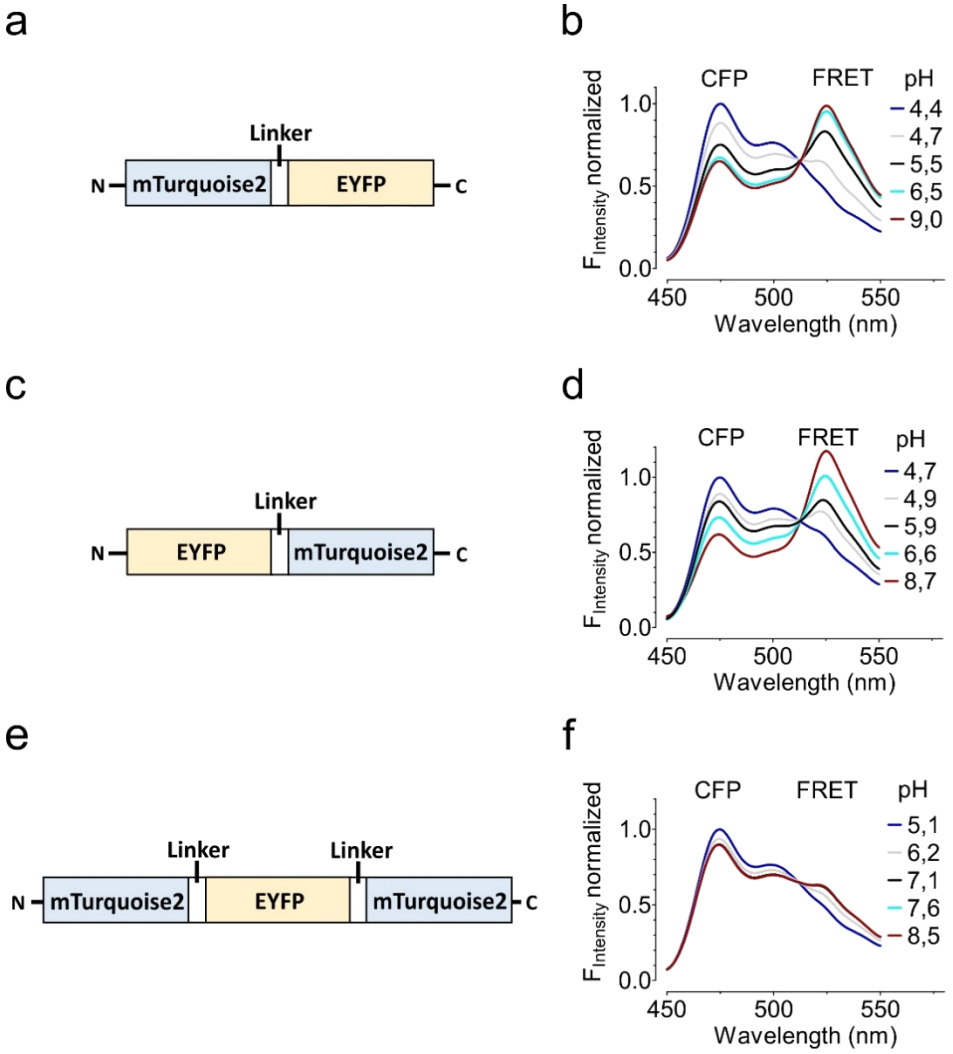

Figure 2: Design and characterization of differently orientated fusion constructs of mTurquoise2 and EYFP. (a) Schematic drawing of the fusion construct consisting of the N-terminal located mTurquoise2 (blue square) and the C-terminal EYFP (yellow square) connected via a flexible $(GGGGS)_2$ linker (white square). **(b)** Normalized emission spectra of the construct shown in **(a)** with the intensities of CFP and FRET emissions plotted in response to different pH values. Emissions were collected upon excitation of mTurquoise2 at 413,4 nm. **(c)** Illustration of the EYFP-mTurquoise2 fusion construct with EYFP (yellow square) at the N-terminal end and mTurquoise2 (blue square) at the C-terminal end, connected via a $(GGGGS)_2$ linker (white square). **(d)** Normalized emission spectra of the construct described in **(b)** with the intensities of CFP and FRET emissions plotted in response to different pH values. Emissions were collected upon excitation of mTurquoise2 at 413,4 nm. **(e)** Scheme of the triple fusion construct comprised of EYFP (yellow square) flanked by one mTurquoise2 (blue squares) on the N- and C-terminal side, respectively, each connected via a $(GGGGS)_2$ linker (white squares). **(f)** Normalized emission spectra of the construct shown in **(c)** with the intensities of CFP and FRET emission plotted in response to different pH values. Emissions were collected upon excitation of mTurquoise2 at 413,4 nm. 4 individual experiments were performed for **(b)**, **(d)** and **(f)**. Reproduced in part & modified with permission from Burgstaller et al., 2019; © American Chemical Society

Therefore, a flexible $(GGGGS)_2$ linker was introduced between the two FPs which should guarantee their close proximity, but also allow some remaining flexibility, as FRET-efficiency is dependent on the distance and orientation of the FPs (141,176). The first construct tested comprised a fusion of mTurquoise2 at the N-terminal end and EYFP at the C-terminal end (**Fig. 2a**)(176). The constructs was expressed in *E.coli* and further purified for measurements in solution using a plate reader. The mTurquoise2-EYFP construct showed a strong pH dependency, as depicted in the FRET spectra (**Fig. 2b**). While the CFP signal was reduced to a minimum at a pH of 9.0, the FRET signal was distinctly increased, pointing to high FRET at alkaline pH. Upon acidification, CFP emission increased, whereas the FRET signal decreased, confirming a reduction of FRET due to protonation, causing a quench of the EYFP. Finally, at acidic pH values, the FRET signal was almost absent (**Fig. 2b**)(176). The second fusion construct of a potential pH sensor was composed of EYFP at the N-terminus and mTurquoise2 at the C-terminus, respectively (**Fig. 2c**). Compared to mTurquoise2-EYFP, the FRET signal of EYFP-mTurquoise2 was moderately higher at alkaline pH values. Upon decreasing the pH levels, the sensor responded concentration dependently to pH changes. Addition of a buffer with pH 4.7 quenched the EYFP fluorescence, leading to reduced FRET, representing a similar response as observed previously (**Fig. 2b** & **Fig. 2d**)(176). Besides these two double FP constructs, a third construct was generated consisting of three FPs. To test whether two mTurquoise2 would enhance the FRET signal, EYFP was flanked with one mTurquoise2 on both of its termini (**Fig. 2e**). In contrast to the other two sensors, precisely reporting pH changes by a drastic change in the fluorescence emission (**Fig. 2b** & **Fig. 2d**), there was only a small detectable change in the emission spectra upon (de-)protonation, making this combination unsuitable to function as a pH probe, due to its reduced dynamic range (**Fig. 2f**)(176).

4.3 Design and characterization of pH-Lemon *in vitro*

Our characterization *in vitro* confirmed, that mTurquoise2-EYFP and EYFP-mTurquoise2 represent suitable pH-sensors and might hence be suitable to effectively measure pH also *in situ* (176). In both constructs tested, a changing FRET-ratio signal can be detected as a result of protonation (**Fig. 3a**)**.** Even though a combination of an N-terminal EYFP with a C-terminal mTurquoise2 seemed to have a slightly higher dynamic range as mTurquoise2-EYFP upon pH alterations (**Fig.2a** – **Fig.2d**), we decided to use the mTurquoise2-EYFP construct for all further experiments (176). Considering our aims of measuring acidic vesicular pH levels as well as pH at the outer side of the plasma membrane, vesicular- and plasma membrane targeting sequences will be located at the C-terminal end of the probe (149,179). This would result in a sensor construct comprised of mTurquoise2 at the N-terminal end, followed by EYFP in the middle and the targeting peptide or fusion protein located at the C-terminal end.

We hypothesized, that such flanking of the pH sensitive EYFP should protect the protein, at least to some extent, from possible proteolytic degradation. While a degradation of the FRET donor mTurquoise2 would completely eliminate the fluorescence signal upon excitation of the donor, degradation of the FRET acceptor EYFP would result in an increased but misleading mTurquoise2 signal that could falsely be interpreted as highly acidic pH values due to acceptor destruction. Considering these important aspects, mTurquoise2-EYFP seemed to be an advantageous combination. Due to the usage of a yellow, pH sensitive and bright FRET acceptor EYFP, we named our novel pH reporter pH-Lemon (**Fig. 3a**)(176).

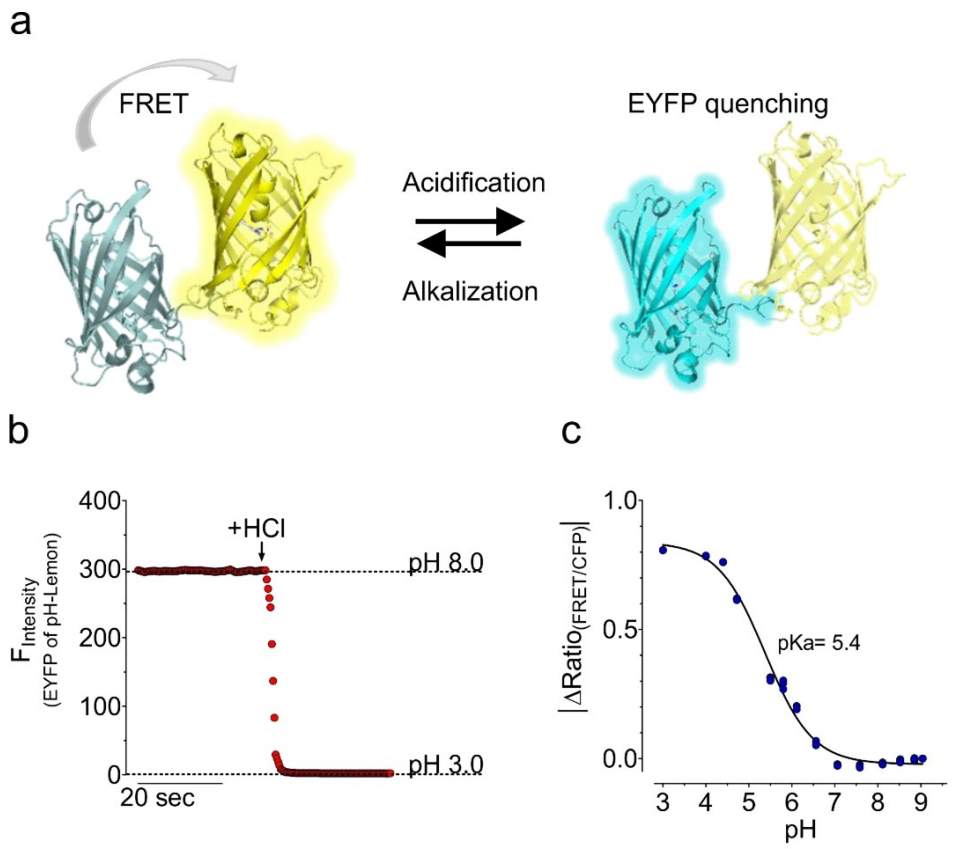

Figure 3: Design and characterization of pH-Lemon *in vitro*. (a) Schematic illustration of pH-Lemon consisting of mTurquoise2 at the N-terminus (cyan) and EYFP (yellow) at the C-terminus. The deprotonated state of the sensor is displayed on the left, resulting in a detectable FRET signal (bright yellow, grey arrow displays FRET) and a reduction of mTurquoise2 emissions (light cyan). In the protonated state (right panel) EYFP fluorescence is quenched (light yellow) yielding a reduction of the FRET signal, while the mTurquoise2 signal increases (bright cyan). **(b)** Representative fluorimetry measurement of recombinant purified pH-Lemon. The pH response of the EYFP fluorescence upon HCl addition is shown (n=3). **(c)** EC_{50} curve of pH-Lemon *in vitro*, determined using protein fluorimetry in response to different pH values (n=4, each replicate is shown). Reproduced in part & modified with permission from Burgstaller et al., 2019; © American Chemical Society

We further aimed to test whether the sensor is suitable to resolve fast pH alterations in real-time. For this purpose, recombinant purified pH-Lemon was analyzed using protein fluorimetry to determine its kinetics upon pH-alterations. After a stable baseline has established at a basal pH of 8.0, the pH was rapidly changed to 3.0 by addition of HCl. This caused a rapid drop of the pH, which was precisely and quickly reported by the sensor. The fluorescence intensity of the pH sensitive EYFP immediately decreased within seconds until no fluorescence emission was detectable at a pH of 3.0 (**Fig. 3b**). Furthermore, we determined the EC_{50} of pH-Lemon *in vitro* using different buffers with distinct pH values ranging from 3.0 to 9.0. The pKa of the purified protein in aqueous solution was found to be 5.4 with a Hill slope of -0.79 (**Fig. 3c**)(176).

4.4 The pH sensitivity of pH-Lemon is independent of the environmental temperature

The environmental temperature is an essential parameter that could affect the kinetics and the sensitivity of a genetically-encoded probe (134). Therefore, we analyzed the response of pH-Lemon to distinct pH levels at different temperatures (**Fig. 4**). The recombinant purified sensor was analyzed upon changing the environmental temperature from 25°C to 40°C in steps of 5°C. While 25°C was chosen as the minimal temperature, the highest temperature of 40°C represents the maximal temperature tested, covering all physiologically relevant temperatures. Importantly, the EC_{50} of pH-Lemon was almost identical under the different conditions, with the same dynamic range of around 0.8 under all temperatures tested (**Fig. 4a**)(176). The pKa of pH-Lemon did not change upon increasing temperatures, as it remained at around 5.4 in the average (**Fig. 4b**)(176). Additionally, also the Hill slope was not affected by the increasing temperature and was found to be -0.91, -0.91, -0.89 and -0.89 for 25°C, 30°C, 35°C and 40°C, respectively (**Fig. 4c**)(176). These characteristics of pH-Lemon are highly advantageous in terms of sensor applicability *in vitro*, and might be crucial for *in vivo* applications, where the temperature cannot be arbitrarily chosen.

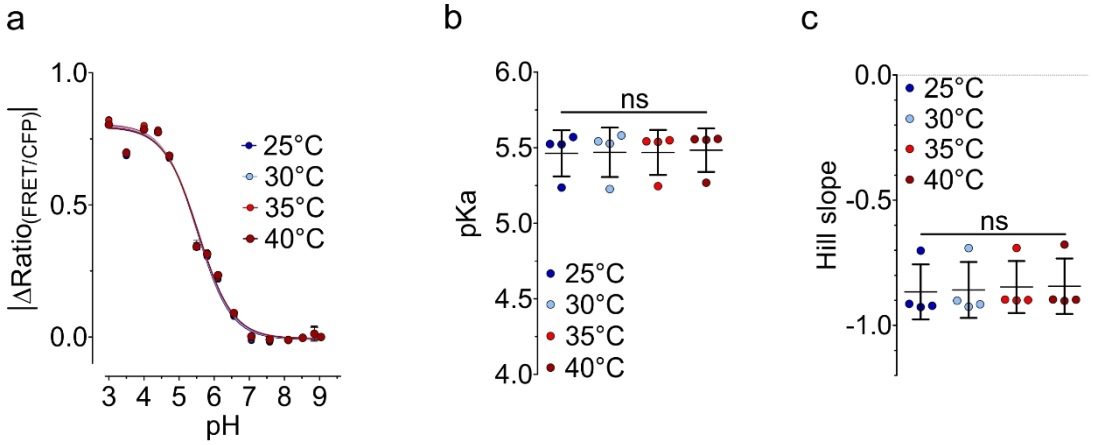

Figure 4: pH-Lemon is temperature insensitive *in vitro*. (a) ΔFRET-ratio values of recombinant purified pH-Lemon as determined using protein fluorimetry using different experimental buffer with distinct pH values from 3.0 to 9.0. During measurements, the temperature of the same wells was adjusted to 25°C (dark blue dots and line), 30°C (light blue dots and line), 35°C (light red dots and line) and 40°C (dark red dot and line). n=4, average ± SD. **(b)** Scatter dot plot of the pKa values of pH-Lemon in response to the temperatures 25°C (dark blue dots and line), 30°C (light blue dots and line), 35°C (light red dots and line) and 40°C (dark red dot and line) with data extracted from the curves shown in **(a)**, n=4, average ± SD. **(c)** Scatter dot blot of the hill slopes of pH-Lemon at the different temperatures 25°C (dark blue dots and line), 30°C (light blue dots and line), 35°C (light red dots and line) and 40°C (dark red dot and line) extracted from the curves shown in **(a)**, n=4, average ± SD. ns= not significant, one-way ANOVA test with Tukey´s post-hoc test. Reproduced in part & modified with permission from Burgstaller et al., 2019; © American Chemical Society

4.5 pH-Lemon is insensitive to physiological changes of intra- or extracellular cation concentrations

Next, we aimed to investigate the sensitivity of pH-Lemon to changes of other physiologically relevant ions besides H^+, as a sensitivity to other ions would make the sensor unsuitable for measuring intra- and extracellular pH levels and pH alterations. While K^+ represents the major intracellular cation with cytosolic concentrations around 140 mM, Na^+ represents the most abundant extracellular cation, also with a physiologic concentration of 140 mM in mammalian organisms (177,180). As the tight regulation of [K^+] and [Na^+] is crucial to maintain cell physiology, [K^+] and [Na^+] are kept close to 100.0 mM – 140.0 mM under physiological conditions (177). Therefore, we analyzed the FRET-ratio signal of recombinant purified pH-Lemon in the presence of 140.0 mM K^+ to mimic the intracellular environment (**Fig. 5a**), or 140.0 mM Na^+, to imitate the extracellular fluid (**Fig. 5b**)(176).

Under these conditions, the FRET-ratio signal of pH-Lemon was not significantly affected by changes of Ca^{2+}, Mg^{2+}, or both (**Fig. 5a** & **Fig. 5b**), indicating that pH-Lemon is insensitive to physiological changes of these ions.

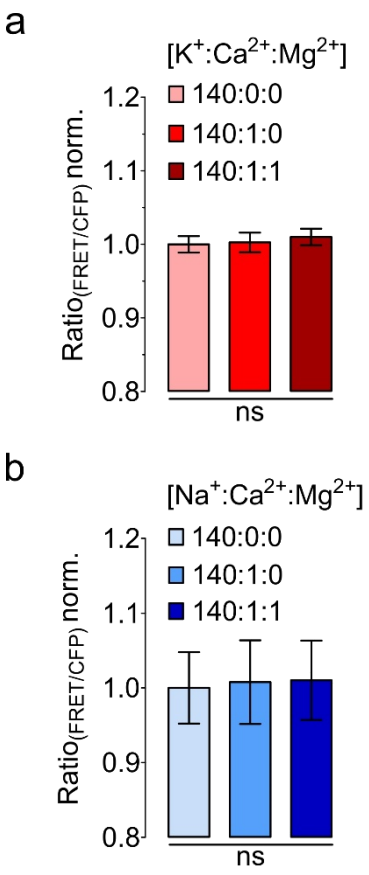

Figure 5: pH-Lemon is not affected by changes of physiologically relevant ion concentrations. (a) Recombinant purified pH-Lemon was analyzed using protein fluorimetry. Shown are normalized FRET-ratio values of the protein in response to different ion concentrations that usually occur intracellular. 3 different buffers containing either 140 mM K^+ (140:0:0, pink), 140 mM K^+ plus 1 mM Ca^{2+} (140:1:0, light red) and 140 mM K^+ plus 1 mM Ca^+ plus 1 mM Mg^{2+} (140:1:1, dark red) were used. n=4, average ± SEM. **(b)** Normalized ratio values of pH-Lemon determined using buffers representing changes of extracellular ion concentrations. Buffers containing 140 mM Na^+ (140:0:0, light blue), 140 mM Na^+ plus 1 mM Ca^{2+} (140:1:0, middle blue) and 140 mM Na^+ plus 1 mM Ca^{2+} plus 1 mM Mg^{2+} (140:1:1, dark blue) were used. n=4, average ± SEM. ns= not significant, one-way ANOVA test with Tukey´s post-hoc test.

4.6 pH-Lemon is suitable for the detection of intracellular H^+ alterations

Considering the precise performance of pH-Lemon *in vitro*, we aimed to characterize the probe *in situ* to test its applicability for live cell imaging experiments. Therefore, we transfected HeLa cells with cytosolic targeted pH-Lemon (pH-Lemon cyto) via lipid based transfection. Due to the nuclear exporting sequence (NES), the construct was found solely in the cytosol (176). Similar to the experiments performed for the *in vitro* analysis, we aimed to determine essential sensor characteristics and kinetics in response to different buffers with distinct pH values ranging from 4.0 to 10.0 (**Fig. 6a**). However, since the probe is located within cells and not soluble in solution, the cells had to be permeabilized with a combination consisting of nigericin and monensin (**Fig. 6a**).

Plotting the single wavelength fluorescence emission signals of cytosolic pH-Lemon confirmed the ratiometric behavior of the probe. While the FRET signals increased in response to increasing pH values, the mTurquoise2 signals declined (**Fig. 6a**)(176).

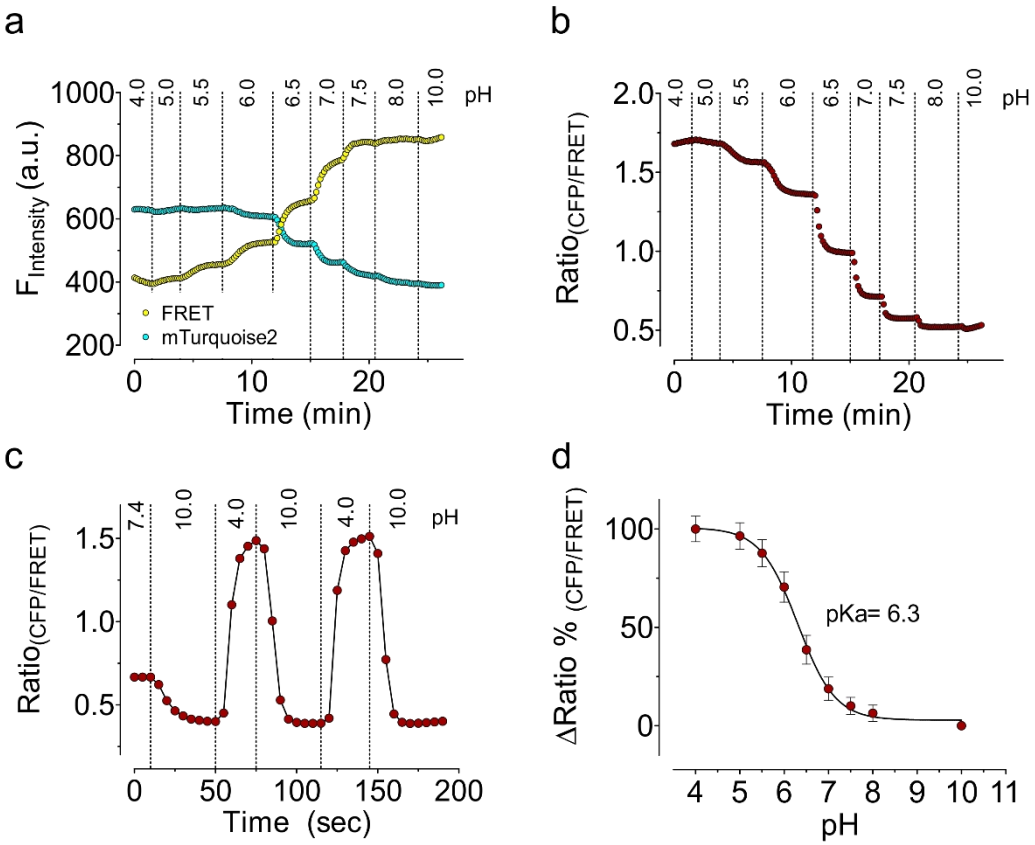

Figure 6: Characterization of cytosolic pH-Lemon in HeLa cells. (a) Representative fluorescence emission signals of mTurquoise2 (cyan dots) and FRET, i.e. EYFP (yellow dots), of permeabilized HeLa cells expressing cytosolic targeted pH-Lemon in response to different pH values from 4.0 to 10.0 (black numbers). n=3. **(b)** Representative FRET-ratio signal over time generated upon division of the data shown in **(a)**. **(c)** Representative FRET-ratio signal over time of permeabilized HeLa cells expressing cytosolic targeted pH-Lemon upon repetitive switching of pH between 4.0 and 10.0. n=9. **(d)** EC_{50} curve of pH-Lemon displayed as the percentage of the FRET-ratio change determined using *in situ* wide-field microscopy. n=3, average ± SD. Reproduced in part & modified with permission from Burgstaller et al., 2019; © American Chemical Society

Division of the mTurquoise2 signal by the FRET emission signal shown in **Fig. 6a**, generated a ratio curve of pH-Lemon under different intracellular proton concentrations with the highest FRET-ratio signal of pH-Lemon detected at a pH of 4.0 and lowest FRET-ratio signal of pH-Lemon detected at a pH of 10.0 (**Fig.6b**). Upon decreasing the pH in steps of 1.0 or 0.5 pH units, the FRET-ratio declined. In contrast to a moderate decrease of the FRET-ratio signal in the very acidic or high alkaline pH range, the biggest sensor response was observed between pH 5.5 to 7.0.

The dynamic range of the probe in protein-rich intracellular environment was found to be around 1.2, with FRET-ratio values of 0.3 to 0.5 at alkaline pH and FRET-ratio values of around 1.5 to 1.7 at acidic pH levels (**Fig. 6b** & **Fig. 6c**)(176). To test whether repetitive (de-)protonation affects the FRET-ratio signal and the amplitude of the maximal response, buffers with pH 4.0 and 10.0 were changed repetitively **(Fig. 6c)**. Within a few seconds, the intracellular pH changed from the minimal to the maximal pH value and vice versa, as reported by the FRET-ratio of pH-Lemon (**Fig. 6c**)(176). However, neither the kinetics, nor the amplitude of the sensor response were affected by repetitive pH-alterations, pointing to a high stability of the sensor. The pKa of pH-Lemon was found to be 6.3 *in situ* (**Fig. 6d**), hence, we supposed the sensor to perfectly respond to pH transitions from acidic toward neutral and vice versa, meeting our criteria for imaging intracellular vesicles as well as pH changes at the plasma membrane (176).

4.7 Image-based read-out of pH alterations *in situ*

Live-cell imaging is perfectly suitable to determine and follow changes of intracellular pH levels. The generated pH curves not only contain information about the pH change, but also about other parameters, like the kinetics of the reaction, the reversibility or the amplitude. However, it might also be useful to determine pH alterations at a first glance by an optical color-based read-out. To generate these images, HeLa cells were permeabilized as described previously with subsequent adjustment of pH levels using various buffers. After acquisition of the donor and acceptor fluorescence emission images, these images were used to generate pseudo-colored ratio images by dividing the mTurquoise2 image by the FRET image with every pixel containing a distinct intensity value. These images are color-coded over a color spectrum from red to blue, with red representing the highest (i.e. acidic pH) and blue representing the lowest ratio (i.e. alkaline pH) (**Fig. 7**)(176). Considering the ratiometric characteristics of pH-Lemon, alkaline pH levels of 10.0 and 8.0 resulted in a high FRET fluorescence, while the mTurquoise2 fluorescence was mildly decreased, resulting in low mTurquoise2/EYFP FRET-ratio values and, therefore, a blue color within the pseudo-colored FRET-ratio images. Due to increasing protonation from pH 7.5 towards acidic, a decrease of the FRET fluorescence with a simultaneous increase of the donor fluorescence could be detected. Due to the acidification, the FRET-ratio values increased, leading to a color-transition in the pseudo-colored ratio images from light blue (pH 7.0) to green (pH 6.0), yellow/orange (pH 5.5/pH 5.0) and finally red (pH 4.0) (**Fig. 7**)(176).

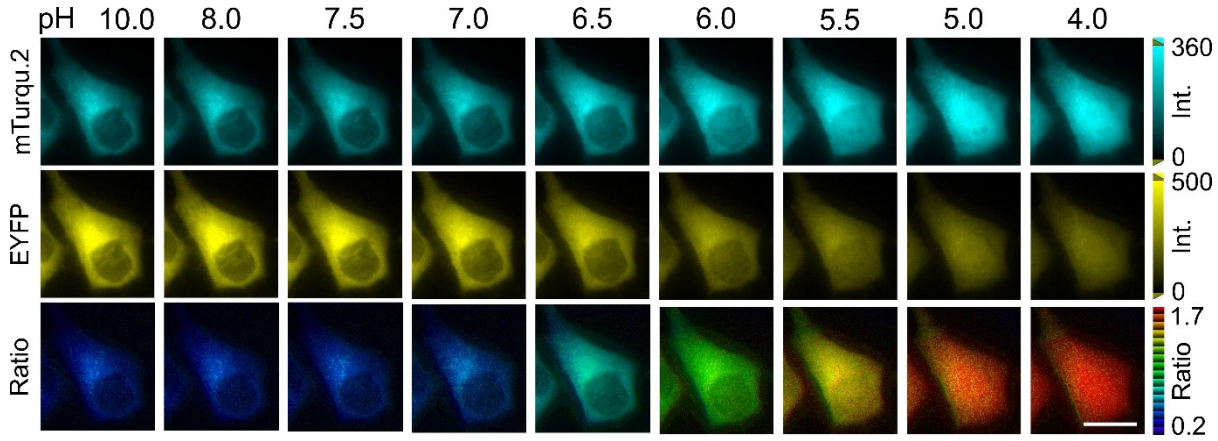

Figure 7: Visualization of intracellular pH alterations using an image-based read-out. HeLa cells expressing cytosolic pH-Lemon were permeabilized using a mixture of nigericin/monensin and images were acquired using wide-field microscopy. Cells were analyzed in response to various buffers with distinct pH values. Displayed are the fluorescence emission images of the FRET donor (mTurqu.2=mTurquoise2, upper panels, cyan) and the FRET acceptor (EYFP, middle panels, yellow). Respective pseudo-colored ratio images received upon division of mTurquoise2/FRET images are shown in the lower panels and scaled from a ratio of 0.2 to 1.7 (ratio scale bar, right of lower panels). Scale bar indicates 10 µm. Reproduced in part & modified with permission from Burgstaller et al., 2019; © American Chemical Society

4.8 Separate exposure of the FPs enhances the dynamic range of pH-Lemon

During classical FRET-imaging, the donor is excited at 430 nm and two emissions are collected simultaneously at 475 nm and 525 nm. This measurement method represents a highly sophisticated technique, however, requires a quite complex microscopic setup, since the emission wavelength have to be separated using a beam-splitter with proper emission filters. To extend the applicability of pH-Lemon, we also tested other measurement techniques. While mTurquoise2 was excited at 430 nm and the emission was detected at 475 nm, also EYFP was directly illuminated at 500 nm, with the emission detected at 525 nm (176). Again, we expected the fluorescence emission signal of EYFP to drop with descending pH values due to the protonation of the EYFP chromophore (**Fig.8a**). To test our assumption, we investigated the fluorescence emissions of recombinant purified pH-Lemon in response to different pH values.

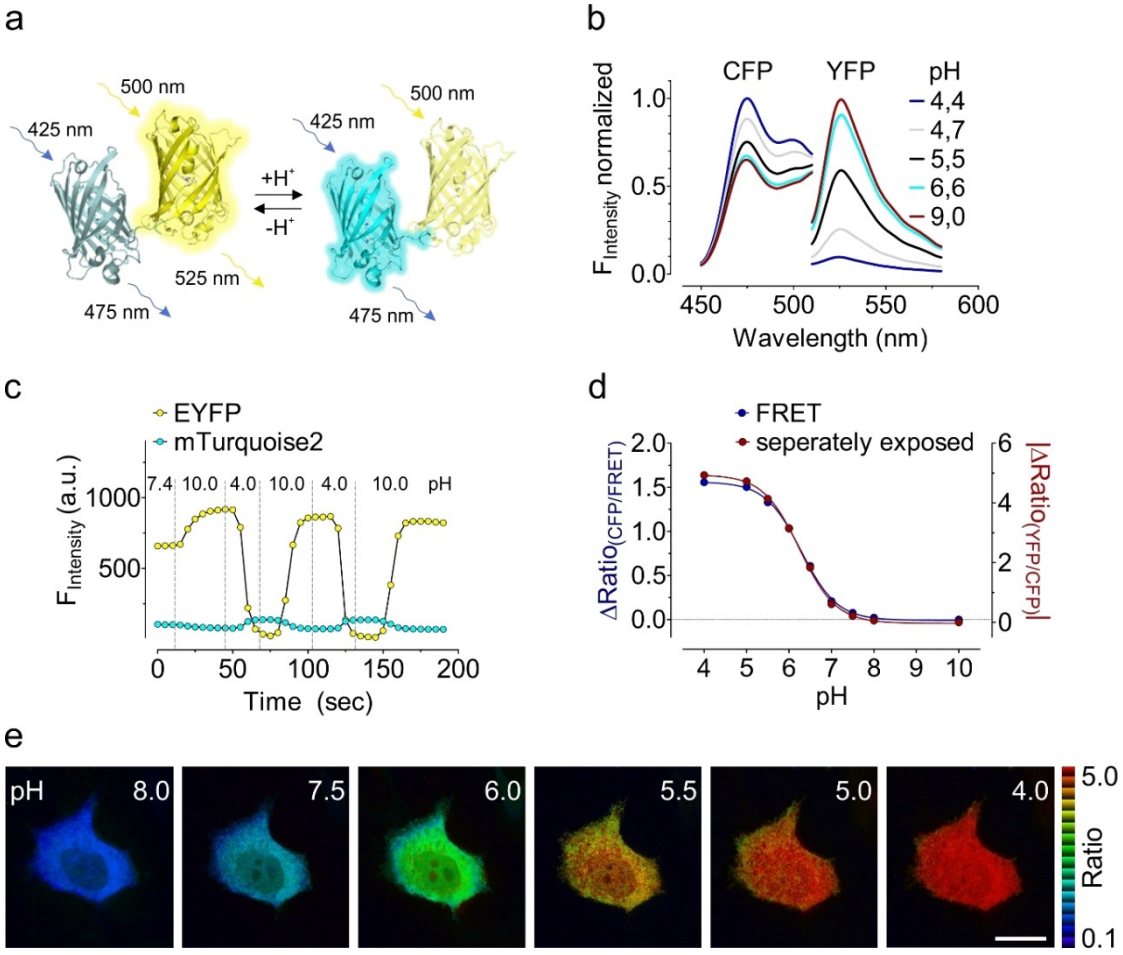

Figure 8: Direct illumination of the two FPs, mTurquoise2 and EYFP, increases the dynamic range of pH-Lemon. (a) Schematic drawing of pH-Lemon under neural/alkaline pH values ($-H^+$, left) and upon acidification ($+H^+$, right). mTurquoise2 (cyan) is excited at 430 nm, emission is detected at 475 nm. EYFP (yellow) is excited at 500 nm and the fluorescence emission is detected at 525 nm. Under alkaline conditions, both emission signals can be detected. Upon acidification, the EYFP fluorescence emission is reduced. **(b)** Fluorescence emission spectra of recombinant purified pH-Lemon upon separate excitation, with the fluorescence emission peaks of mTurquoise2 and EYFP shown at different pH values (indicated on the right). 4 experiments were performed. **(c)** Representative single cell fluorescence signals over-time of mTurquoise2 (cyan dots) and EYFP (yellow dots) of pH-Lemon expressed in HeLa cells, upon repetitive switching between acidic (pH 4.0) and alkaline (pH 10.0) pH values. n=10. **(d)** EC_{50} curves of pH-Lemon either generated using FRET analysis (blue curve and dots, plotted on left Y-axis) or separate exposure (dark red curve and dots, plotted on right Y-axis) in response to pH values ranging from pH 4.0 to 10.0. n=3 for both. **(e)** Pseudo-colored ratio images of HeLa cells expressing cytosolic pH-Lemon, received upon division of the mTurquoise2/EYFP image, which were acquired using ACLSM. mTurquoise2 and EYFP were excited separately and permeabilized HeLa cells were analyzed in response to buffers with various pH values (white numbers in each panel). Scale bar represents 10 µm. Reproduced in part & modified with permission from Burgstaller et al., 2019; © American Chemical Society

Analysis of the emission spectra unveiled an enlarged dynamic range of the EYFP fluorescence emission signals compared to classical FRET measurements (**Fig. 2a**), when illuminated separately (**Fig. 8b**)(176). The effect of an enhanced dynamic range was not only observed using the purified protein, but also in permeabilized HeLa cells expressing pH-Lemon (**Fig. 8c**). First, cells were kept in a buffer with a physiological extracellular pH of 7.4. Upon switching the extracellular buffer to pH 10.0, the probe located in the cytosol responded in a ratiometric manner, with an increase in EYFP and a decrease in mTurquoise2 fluorescence (**Fig. 8c**). As expected, pH-Lemon showed a fast and reproducible response (**Fig. 8c**) using this alternative measurement technique (176). Since direct excitation of the EYFP resulted in an enlarged dynamic range, it was necessary to test for a possible change of the EC_{50}. Importantly, the EC_{50} remained unchanged under these conditions, when compared to classical FRET-imaging data (**Fig. 8d**)(176). Generation of pseudo-colored ratio images displayed a similar color-coding as images received from FRET measurements, which facilitates a comparison of the different measurement techniques (**Fig. 8e**)(176).

4.9 pH-Lemon is suitable for fluorescence lifetime imaging microscopy

In order to test the applicability of pH-Lemon for other microscopic techniques than ratiometric fluorescence intensity imaging, we tested the suitability of the probe for fluorescence lifetime imaging microscopy (FLIM). Besides FRET imaging, FLIM measurements represent another highly sophisticated gold-standard method for quantitative imaging approaches (181). Therefore, we either expressed mTurquoise2 or pH-Lemon, respectively, in HEK-293 cells. After permeabilization of the cells for H^+ using nigericin and monensin, pH values from 4.0 to 8.0 were adjusted. The fluorescence lifetime of mTurquoise2 slightly declined with decreasing pH if the FP was expressed alone in HEK-293 cells (**Fig. 9a**)(176). However, interestingly, the fluorescence lifetime of mTurquoise2 increased pH-dependently, if the lifetime of the FP was measured in the pH-Lemon construct, probably caused by the quench of the EYFP and reduced FRET-efficiency upon acidification (**Fig. 9a**)(176). To investigate whether FLIM is also suitable to provide a high-resolution, image-based read-out of pH-Lemon, we analyzed the abundances of fluorescence lifetimes of mTurquoise2 frequencies of these permeabilized cells. Therefore three different pH values were chosen, a high pH of 7.01, a low pH of 4.03 and a pH of 6.05, which is close to the EC_{50} of pH-Lemon (**Fig. 9b**)(176). The relative abundances of fluorescence lifetimes at these pH values also nicely confirmed the pH-dependency of mTurquoise2 in pH-Lemon. While mTurquoise2 in pH-Lemon had a fluorescence lifetime of around 2.4 ns at neutral pH, the lifetime increased to 2.8 ns at pH 6.0.

Upon acidification to pH 4.0, the fluorescence lifetime of the mTurquoise2 in pH-Lemon further increased to 3.5 ns (**Fig. 9a** & **Fig. 9b**)(176). These distributions of fluorescence lifetimes that are clearly pH dependent, could also be observed in pseudo-colored images of HEK-293 cells (**Fig. 9c**)(176). Upon changing intracellular pH levels, a pH-dependent color-code could be determined. Similar to the pseudo-colored ratio images obtained from the FRET- as well as separately exposure measurements, cells appeared blue at alkaline pH, green at a pH near the EC_{50} of pH-Lemon and red at acidic pH (**Fig.7, Fig.8e** & **Fig. 9c**). This color-coded read-out of pH values was independent of the expression level of the probe, as the same color was obtained by analyzing cells with low and high expression of pH-Lemon (**Fig. 9c** & **Fig. 7**)(176).

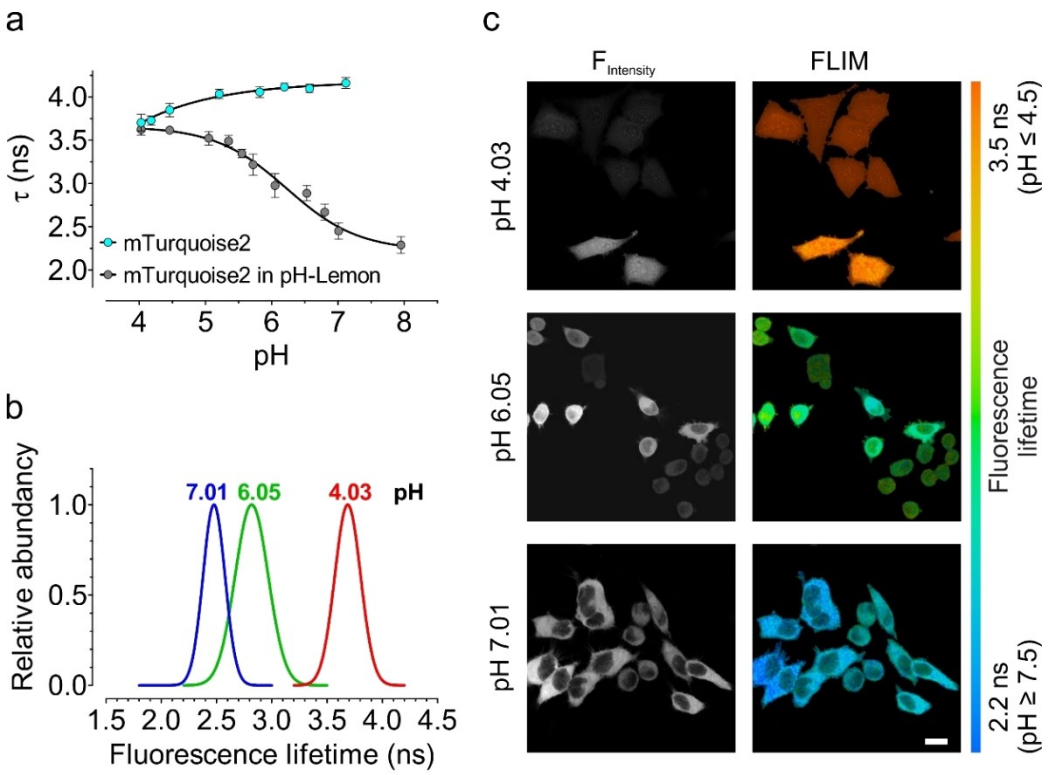

Figure 9: pH-Lemon is suitable for the detection of pH alterations using fluorescence lifetime imaging microscopy (FLIM). (a) Fluorescence lifetime curves of mTurquoise2 in HEK-293 cells expressing either mTurquoise2 alone or as part of cytosolic targeted pH-Lemon. Cells were permeabilized using nigericin and monensin and different pH values were adjusted. **(b)** Relative abundances of mTurquoise2 fluorescence lifetimes in the pH-Lemon construct, expressed in HEK-293 cells at high pH (pH 7.01), a pH close to the EC_{50} of pH-Lemon (pH. 6.05) and low pH (pH 4.03). (**c**) Pseudo-colored FLIM images of HEK293 cells expressing pH-Lemon targeted to the cytosol in response to pH 7.01 (upper panels), 6.05 (middle panels) and 4.03 (lower panels). Scale bar indicates 10 µm. Reproduced in part & modified with permission from Burgstaller et al., 2019; © American Chemical Society

4.10 pH-Lemon does not discriminate between neutral to alkaline pH values

Every cellular organelle is known to have a specific pH range, which ensures homeostasis and proper functioning of cell metabolism (2). Therefore we aimed to test the suitability of pH-Lemon to detect organelle specific pH values by generating differently targeted pH-Lemon constructs (**Fig.10**)(176). While the cytosolic pH-Lemon already proved suitable to detect cytosolic pH alterations in permeabilized cells, expression of the pH probe in intact HeLa cells confirmed a neutral, homogenously distributed pH value in the cytosol of these cells (**Fig. 10a**)(176).

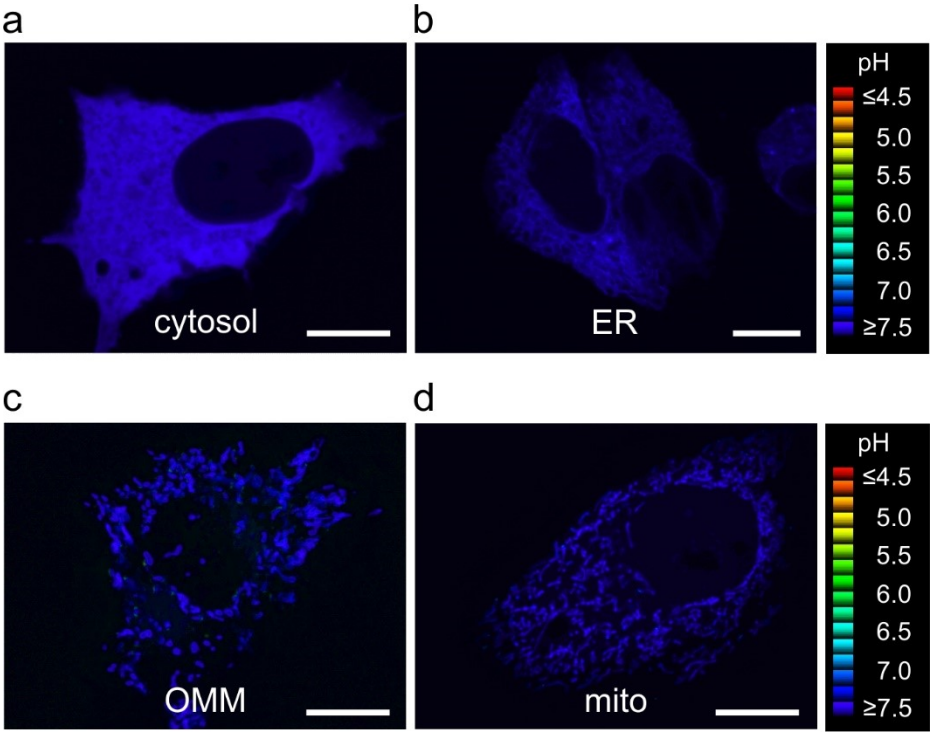

Figure 10: Targeting of pH-Lemon to intracellular compartments for the visualization of pH levels. **(a)** Representative pseudo-colored ratio image of HeLa cells transfected with cytosolic targeted pH-Lemon. Cytosolic targeting was achieved using a nuclear exporting sequence (NES). **(b)** Representative pseudo-colored ratio image of HeLa cells expressing pH-Lemon targeted to the ER. Targeting to the lumen of the ER was achieved using an N-terminal targeting sequence of Calreticulin (CaR) and a C-terminal ER-retention site (KDEL). **(c)** Representative pseudo-colored ratio image of the pH at the outer mitochondrial membrane (OMM) in HeLa cells transfected with pH-Lemon fused to OMP25. **(d)** Mitochondrial (mito) targeting of pH-Lemon expressed in HeLa cells was achieved using a tandem dimeric repeat of the COX8 targeting sequence. Image displays a representative pseudo-colored ratio image. The corresponding pH values to the pseudo-coloration are displayed in the ratio scale bars on the right. All images were acquired using an automated Nipkow-spinning-disk-based array confocal laser scanning microscope. Scale bars indicate 10 µm. Reproduced in part & modified with permission from Burgstaller et al., 2019; © American Chemical Society

Fusion of pH-Lemon to Calreticulin (CaR) on the N-terminal end and to an endoplasmic reticulum retention site with the amino acid sequence KDEL at the C-terminal end forced the probe to enter the ER lumen (182). pH-Lemon targeted nicely to the ER, without any unspecific signals detectable. As expected, the ER showed pH levels similar to that found within the cytosol (**Fig. 10b**)(176). Considering the high metabolic activity at the mitochondrial membrane as well as the intermembrane space (IMS), pH-Lemon was fused to OMP25, a protein located at the outer mitochondrial membrane (OMM)(183). This caused membrane staining of mitochondria without signals coming from the mitochondrial matrix. Interestingly, although there are many metabolic processes occurring at the mitochondrial membrane, no acidic pH values were detected at the OMM of HeLa cells (**Fig. 10c**)(176). In order to generate a sensor, that is located in the mitochondrial matrix, pH-Lemon was fused to a tandem dimeric repeat of the commonly used mitochondrial targeting sequence of COX8 (184). Again, the ratio signal of pH-Lemon confirmed the neutral to alkaline pH in the mitochondrial matrix of HeLa cells (**Fig.10d**)(176). These experiments indicated, that pH-Lemon might be suitable to confirm pH levels in the alkaline range, however, a precise determination of alkaline pH levels cannot be made.

4.11 pH-Lemon fused to LC3B detects autophagic vesicles

The application of pH-Lemon already confirmed neutral to alkaline pH values in the cytosol, the ER, the mitochondrial matrix as well as at the OMM (176). However, considering a slightly acidic pKa of 6.3, applications within acidic compartments might be even more interesting. Acidic pH values are mainly found in intracellular vesicular structures like lysosomes, secretory or endosomal vesicles (64,176,185). To achieve vesicular targeting of pH-Lemon, the probe was fused to the N-terminal end of LC3B, which is a commonly used targeting sequence for the autophagic pathway (**Fig. 11a**)(176,179). LC3B fulfills an essential role in the formation of the phagophore to build up autophagosomes for subsequent fusion with acidic, hydrolase containing lysosomes to re-use the amino acids or fatty acids as building blocks (179,186). We hypothesized, that pH-Lemon fused to LC3B might be suitable to detect pH changes resulting from fusion events of neutral autophagosomes with acidic lysosomes. In order to test our hypothesis, high resolution images of pH-Lemon - LC3B were acquired (**Fig. 11b** & **Fig. 11c**). The fluorescence emission images of mTurquoise2 and EYFP display mild cytosolic and nuclear staining (**Fig. 11b**)(176). While many small roundish structures with strong mTurquoise2 fluorescence were detectable, only some of these structures displayed EYFP fluorescence **(Fig. 11b**)(176). We concluded that small structures possessing both fluorescent signals might be autophagosomes, which should have neutral pH values (176).

In contrast, structures possessing only mTurquoise2 fluorescence might be autophagosomes that underwent fusion with lysosomes (=autolysosomes), indicated by the reduction of EYFP signal due to the acidic lysosomal pH. The majority of the vesicles could be found in a perinuclear region in a high density with some single vesicles also in the periphery (176). Analysis of the images upon pseudo-coloration revealed a huge pH heterogeneity of LC3B positive vesicles, with many vesicles possessing mild acidic pH values (green and yellow vesicles) and some structures with extremely acidic pH levels (red vesicles) as well as almost neutral pH, possible neutral autophagosomes (**Fig. 11b**)(176). A zoom into vesicles confirmed the dependency of the two fluorescence emission signals on the proton concentration. While acidic pH caused a reduction of the EYFP signal, the mTurquoise2 was clearly detectable. In contrast, alkalization of the vesicles led to an increase of the EYFP fluorescence, resulting in a reduced donor fluorescence (**Fig. 11c**).

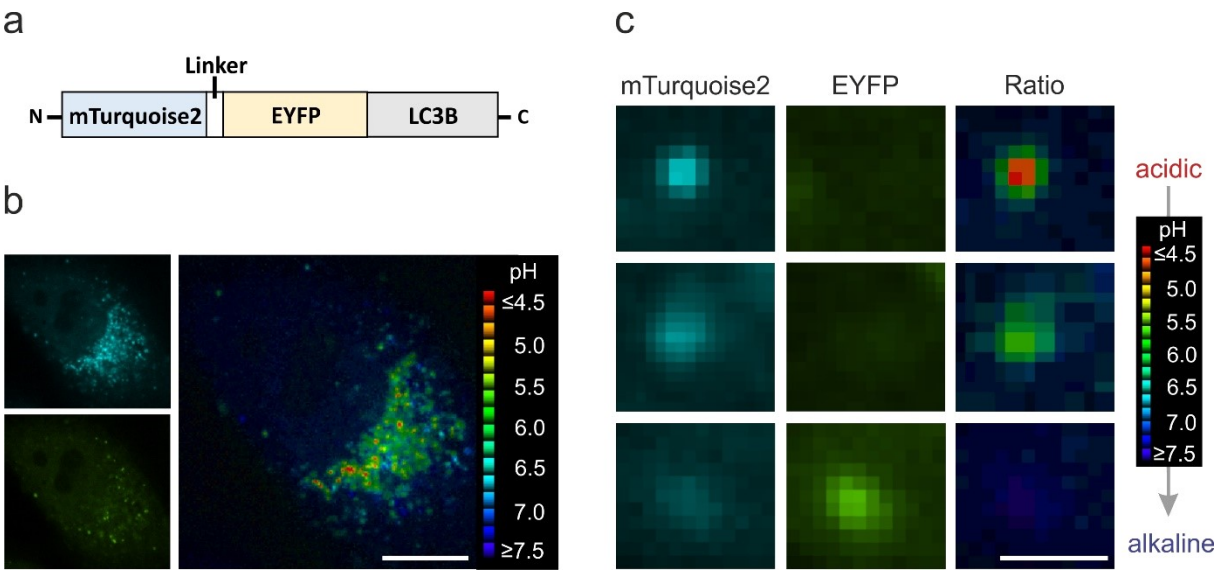

Figure 11: pH-Lemon is targeted to autophagic vesicles upon fusion to LC3B. (a) Schematic drawing of pH-Lemon-LC3B, consisting of mTurquoise2 (blue square) and EYFP (yellow square) connected via a linker (white square) at the N-terminal end and LC3B (grey square) at the C-terminal end of the construct. **(b)** Representative ACLSM images of starved HeLa cells expressing pH-Lemon-LC3B. Fluorescence emission images of mTurquoise2 (upper left image) and EYFP (lower left image) are shown. Respective pseudo-colored ratio image (right,) was generated by division of mTurquoise2 by EYFP fluorescence emission signals. **(c)** Zoom of vesicular structures in HeLa cells expressing pH-Lemon-LC3B. Fluorescence emission signals of mTurquoise2 (left column), EYFP (middle column) and the corresponding pseudo-colored ratio images (right column) are shown. Estimated pH values of the ratio image are displayed. Scale bar represents 5 µm **(b)** and 1 µm **(c)**. Reproduced in part & modified with permission from Burgstaller et al., 2019; © American Chemical Society

4.12 pH-Lemon is suitable for the real-time visualization of autophagy

For the previously described experiments, HeLa cells were starved for two hours prior to measurements, which resulted in the detection of many acidic vesicles thought to be autolysosomes. However, the induction of autophagy caused by either starvation or other stimuli represents an important event in cell metabolism (187). Hence, monitoring the induction of autophagy in real-time is of great importance and interest. To test the suitability of pH-Lemon to track the autophagic flux in real-time, i.e. the fusion of autophagosomes with lysosomes, HeLa cells were imaged using wide-field microscopy upon starvation. Interestingly, the number of vesicles did not change within 30 minutes of starvation (**Fig. 12**). However, the appearance of some acidic vesicles after 45 minutes points to the formation of (probably) autolysosomes. During prolonged starvation, the number of vesicular structures increased with many red and green vesicles detectable in a perinuclear region after 105 minutes (**Fig. 12**).

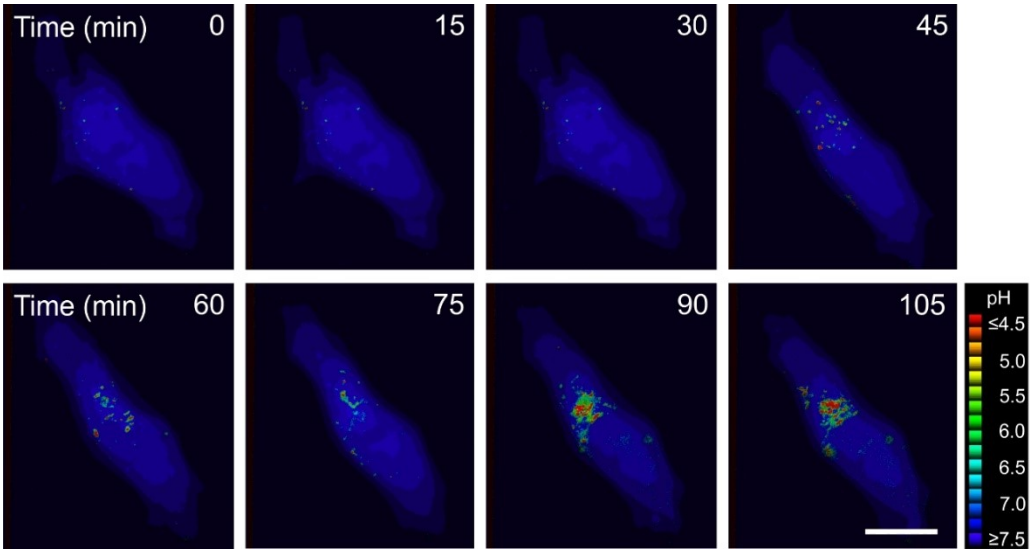

Figure 12: Dynamic visualization of autolysosome formation. HeLa cells expressing pH-Lemon-LC3B were imaged using wide-filed microcopy and kept in a physiological buffer with 2 mM glucose, without amino acids or fetal calf serum. Images were acquired every 15 minutes for the duration of 105 minutes. Ratio images were generated by division of mTurquoise2 by FRET emission. Scale bar represents 10 µm. Estimated pH values according to the respective ratios are displayed.

4.13 Targeting pH-Lemon to the secretory pathway

Besides autophagy, acidic pH values are furthermore a hallmark of the secretory pathway, as secretory vesicles acidify on their way to the plasma membrane (176,188). To target the pH probe to the secretory pathway, we fused pH-Lemon to the targeting sequence of CDH13 on the N-terminal end and a GPI-anchor on the C-terminal end (**Fig. 13**)(176).

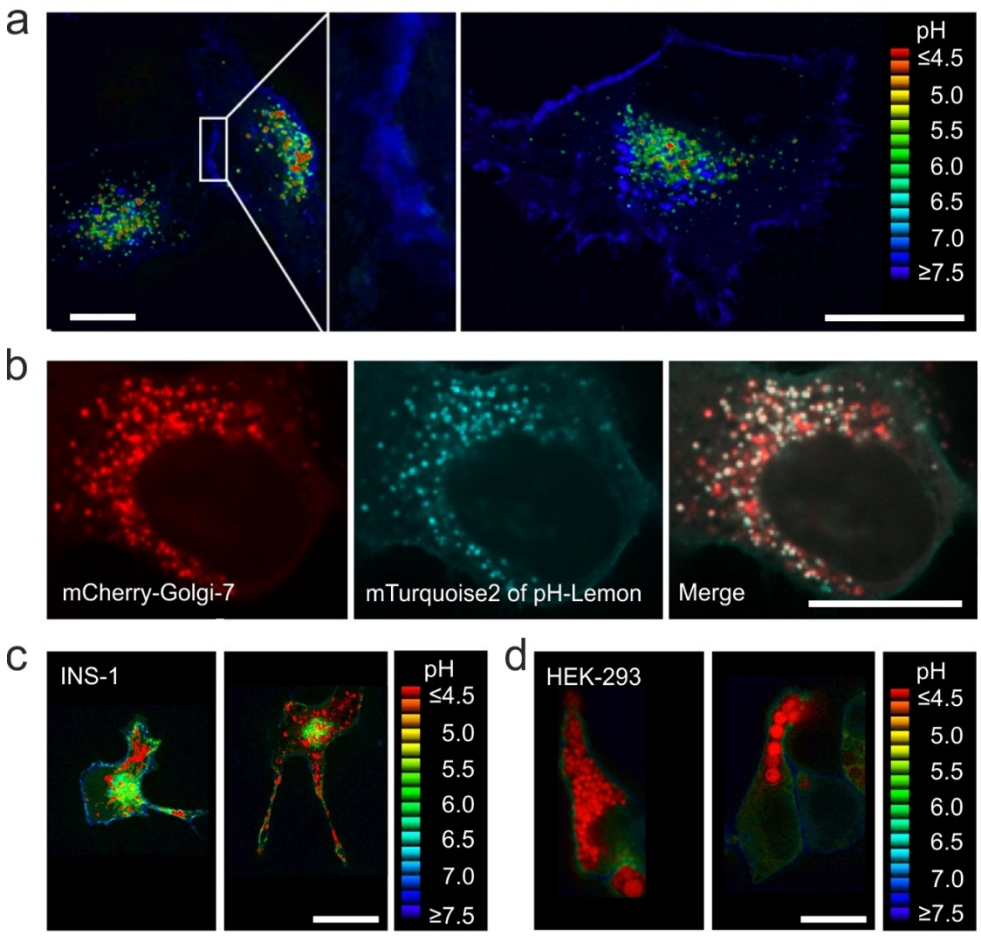

Figure 13: Targeting the secretory pathway by expression of pH-Lemon – GPI. (a) Representative pseudo-colored ratio images of HeLa cells expressing pH-Lemon – GPI with a zoom at the plasma membrane indicated by the white square (zoom in left panel). Scale bar represents 10 µm. **(b)** HeLa cell co-expressing mCherry-Golgi-7 and pH-Lemon - GPI. Shown are the mCherry signals (left image), the mTurquoise2 signals of pH-Lemon (middle image) and the respective overlay (right image). Sale bar represents 10 µm. **(c)** Pseudo-colored ratio images of INS-1 cells expressing pH-Lemon – GPI. Sale bar represents 10 µm. **(d)** Representative pseudo-colored ratio images of HEK-293 cells transfected with the pH-Lemon – GPI construct. Estimated pH values are indicated beside the ratio bars. Sale bar represents 10 µm. All images were acquired using ACLSM. Reproduced in part & modified with permission from Burgstaller et al., 2019; © American Chemical Society

Upon expression, the probe first entered the ER, leading to a weak ER signal, with subsequent transport into the Golgi apparatus. Due to the GPI-anchor fused to the probe, the sensor was packed into secretory vesicles emanating from the Golgi complex and transported towards the plasma membrane, where the GPI-anchor was integrated into the cell membrane. Since the probe was facing the extracellular space, the sensor reported the pH of the extracellular buffer of 7.4, leading to a blue membrane color. Interestingly, a huge portion of the probe could be found in secretory vesicular structures that were mainly located in a perinuclear region (**Fig.13a**)(176).

Similar to the LC3B construct, the GPI-fusion construct revealed a huge pH heterogeneity of secretory vesicles in HeLa cells, i.e. different colors in the ratio images, possibly due to the acidification that is necessary for secretory vesicle maturation (**Fig. 13a**)(176). To prove that the vesicular structures were indeed intracellular vesicles and not caused by sensor accumulation, we co-expressed mCherry-Golgi-7, a frequently used marker for the Golgi apparatus, with pH-Lemon – GPI in HeLa cells. Due to its targeting sequence, the mCherry construct was found in the Golgi complex, but also within vesicles (176). The generation of overlays of the mCherry construct and the mTurquoise2 fluorescence image of pH-Lemon confirmed our assumption that pH-Lemon – GPI is located in secretory vesicles, since the majority of the vesicles showed a clear overlay of the two signals. The intracellular structures were hence caused by transporting pH-Lemon towards the plasma membrane within secretory vesicles and were not the result of accumulating sensor proteins within the cytosol (**Fig. 13b**)(176). To exclude the possibility of HeLa cell line specific effects, the construct was tested in two other cell lines. Therefore, the pancreatic beta cell line INS-1 832/13 (INS-1) (**Fig. 13c**) and the human embryonic kidney cell line HEK-293 (**Fig. 13d**) was transfected with the construct (176). In contrast to HeLa cells where single vesicles could be distinguished also in the high-density vesicular region, in INS-1 cells, this region seemed blurred green, which may represent the Golgi apparatus. Some acidic vesicles were found in the branching arms of the cells (**Fig. 13c**). The previously seen heterogeneity with different colored vesicles could not be observed in HEK-293 cells (**Fig. 13d**). Surprisingly, the sensor unveiled huge, highly acidic vesicles that take up excessive amounts of intracellular space. Furthermore, the amount of sensor that traversed the entire cell and was exposed on the cell surface seemed to be less in both cell lines compared to HeLa cells (**Fig. 13a** & **Fig. 13b**)(176).

4.14 Revealing the pH heterogeneity of secretory vesicles using pH-Lemon

Considering the different pH values of intracellular vesicles, we analyzed these different populations in more detail. Expression of the probe in HeLa cells led to the previously observed localization within vesicles bearing different pH values (**Fig. 14a**)(176). Within one single cell, the vesicles could be divided into different sub-groups of red, yellow, green, cyan and blue vesicles, based on their color, i.e. pH values (**Fig. 14a**). Interestingly, red vesicles, and to some extent also the other vesicles, seemed to have a different pH at the border (**Fig. 14a**)(176).

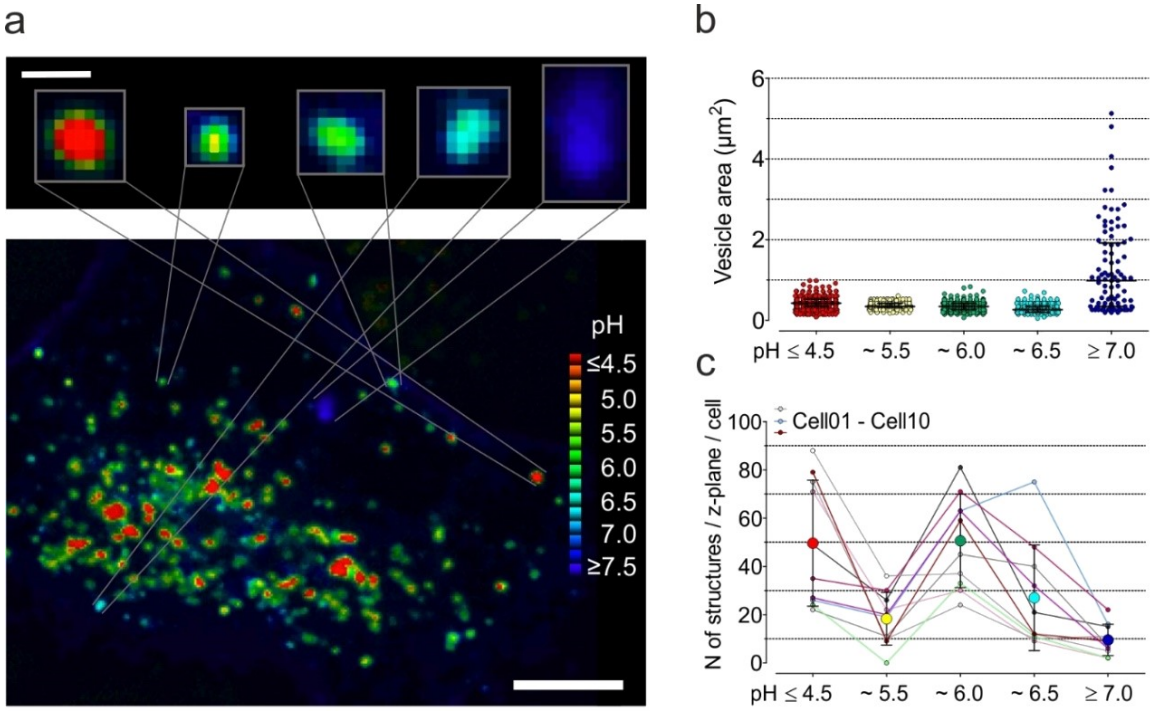

Figure 14: Classification of vesicles into different sub-categories based on their pH values. (a) Representative pseudo-colored ratio image of a region with high vesicular density in a HeLa cell expressing pH-Lemon – GPI. Pseudo-coloration revealed vesicles with different ratio, i.e. pH values displayed as differently colored structures (lower panel, scale bar indicates 10 µm). Upper panel displays a zoom of single representative vesicles with different colors, red, yellow, green, cyan and blue, i.e. acidic to alkaline pH. Scale bar indicates 1 µm. **(b)** Scatter dot plot of the vesicles of 10 cells divided into different categories with estimated pH values of ≤4.5 (red dots), ~5.5 (yellow dots), ~6.0 (green dots), ~6.5 (cyan dots) and ≥7.0 (blue dots). The vesicle area in μm^2 is shown on the Y-axis. Values are displayed as median ± interquartile range, n=1150 vesicles in total of 10 different cells. **(c)** Scatter dot plot of the number of vesicular structures per z-plane per cell of the vesicles analyzed in **(b)**. The vesicles of one cell are displayed as small dots with the same color and connected via a thin line, while big dots (red, yellow, green, cyan, blue) represent the average (average ± SEM) of the vesicle number in each category, n=1150 vesicles in total. Reproduced in part & modified with permission from Burgstaller et al., 2019; © American Chemical Society

To determine a possible connection between the pH and the size of the vesicles, 1150 vesicles of 10 different cells expressing pH-Lemon - GPI were analyzed. The vesicles were assigned to one of five groups according to their ratio vales (i.e. pH values) and plotted against the vesicle area. Red, yellow, green and cyan vesicles seemed to have similar size between 0.2 and 1 μm^2 (**Fig. 14b**)(176). In contrast, the size of blue, i.e. alkaline vesicles and structures within the analyzed cells ranged from 0.5 μm^2 to 6 μm^2 (**Fig. 14b**)(176). The majority of intracellular vesicles belonged to the category with estimated pH values of ≤4.5 (red) and ~6.0 (green), with approximately 50 structures per z-plane per cell in the average. The number of yellow, cyan and blue vesicles was lower with average 20, 30 and 10 structures per z-plane per cell, respectively (**Fig. 14c**)(176).

4.15 Visualization of vesicles with different pH values using fluorescence lifetime imaging microscopy

pH-Lemon has already proven suitable for the detection of intracellular pH alterations using fluorescence lifetime imaging microscopy (FLIM) (176). However, the possibility to visualize the pH level of small structures like secretory vesicles and the Golgi apparatus using other techniques than array confocal laser scanning microscopy and fluorescence wide-field microscopy would drastically expand the applications of the probe. For this purpose, we transfected HEK-293 cells with pH-Lemon – GPI followed by further analysis using FLIM.

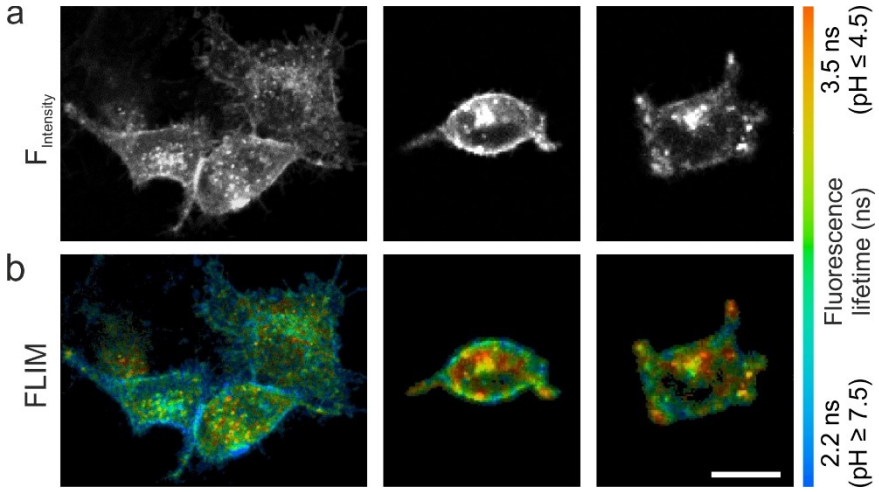

Figure 15: Detection of vesicular pH levels using FLIM. (a) Representative images of the mTurquoise2 fluorescence intensity of HEK-293 cells expressing pH-Lemon – GPI. **(b**) Corresponding pseudo-colored fluorescence lifetime images of the cells shown in **(a)** based on the different fluorescence lifetimes caused by different intra- and extracellular pH levels. Scale bar represents 10 µm for **(a)** & **(b)**. Ratio scale of the fluorescence lifetimes with estimated pH values is indicated on the right. Reproduced in part & modified with permission from Burgstaller et al., 2019; © American Chemical Society

As observed previously, the construct was located at the cell surface and within vesicles, causing a bright fluorescence signal detected at the cell border, within vesicles and the Golgi apparatus (**Fig. 15a**)(176). As expected, a pseudo-coloration of the fluorescence lifetime of mTurquoise2 of pH-Lemon – GPI displayed a similar color-coding as observed previously using ACLSM, indicating the different pH values of the different subcellular structures (**Fig. 13, Fig 14** & **Fig. 15b**)(176). Importantly, a comparison of the fluorescence intensity image with the fluorescence lifetime image demonstrated that there was no correlation between the brightness caused by high abundances of mTurquoise2 at various subcellular structures and the fluorescence lifetime of the FP (**Fig. 15**)(176). While the cell surface showed a short fluorescence lifetime of approximately 2.2 ns (blue), some intracellular vesicles possessed a long fluorescence lifetime of up to 3.5 ns (red). Similar to the experiments using conventional, high resolution fluorescence intensity imaging on an ACLSM, intracellular vesicles covered the whole range of fluorescence lifetimes (yellow and green) (**Fig. 13, Fig 14** & **Fig. 15b**)(176). These experiments indicate the suitability of pH-Lemon – GPI for subcellular pH quantifications of small cellular structures using FLIM, and confirmed the pH heterogeneity of intracellular vesicles as observed by ACLSM.

4.16 pH-Lemon features high stability in acidic environments

Targeting pH probes to either autolysosomes or the secretory pathway bears the risk of sensor degradation due to acidic pH levels in these environments (189,190). These acidic vesicles represent an extremely hostile environment for genetically-encoded sensors. The high activity of H^+ pumps acidifying the vesicular lumen and the possible presence of proteases could damage the sensor (190). To minimize the risk of potentially non-functional sensor within acidic vesicles, the FPs need to be stable in terms of degradation or proteolysis. Our previous analysis of pseudo-colored ratio images resulted in red color for acidic structures and blue for neutral compartments. However, false positive red colored vesicles within the ratio images would also be observed, if the EYFP would be non-fluorescent as a consequence of degradation or misfolding. To confirm that the red color in these ratio images indeed resulted from quenching of the fluorescence due to acidic pH and not from degradation of the EYFP, we aimed to neutralize acidic vesicles to regain EYFP fluorescence (**Fig. 16a**)(176). We hypothesized that the addition of a mixture consisting of sodium azide (NaN_3) and ammonium chloride (NH_4Cl) might result in neutralization of intravesicular pH values, as it has been described previously (**Fig. 16a**)(191).

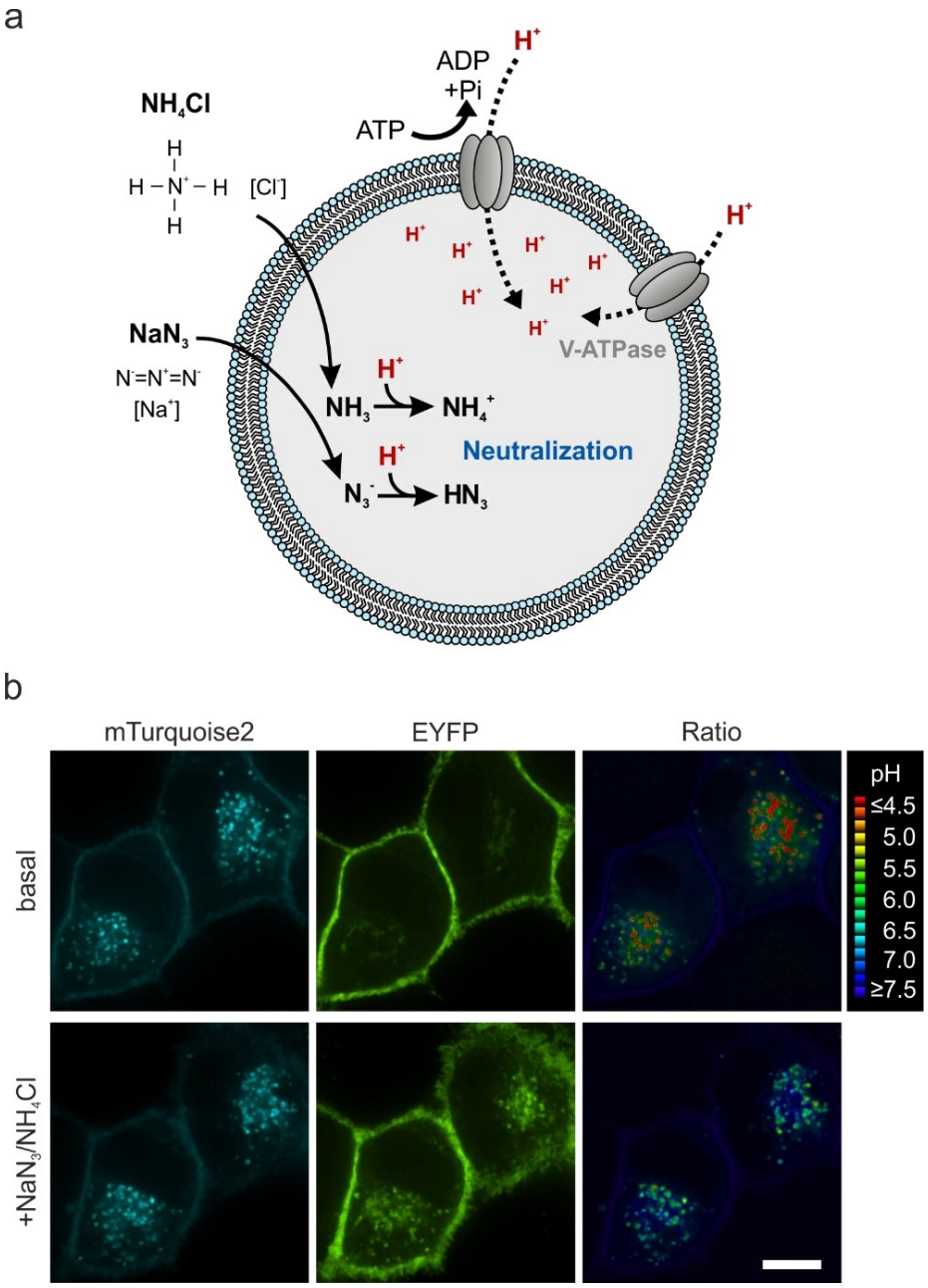

Figure 16: EYFP fluorescence was restored upon neutralization of vesicular pH levels. (a) Schematic drawing of the proposed mechanisms of the neutralization of acidic vesicles. V-ATPases (grey) located at the vesicular membrane function as proton pumps (H^+, red) by hydrolyzing ATP in order to generate an acidic lumen. Addition of sodium azide (NaN_3) and ammonium chloride (NH_4Cl) potentially neutralizes acidic vesicles by diffusion of azide and ammonia through the membrane, buffering the high vesicular proton concentration, thereby possibly generating hydrazoic acid and ammonium, respectively. **(b)** ACLSM images of HeLa cells expressing pH-Lemon – GPI. Shown are the mTurquoise2 and EYFP fluorescence images, as well as the respective pseudo-colored ratio images of untreated cells (basal, upper row) and the same cells after treatment with NaN_3 and NH_4Cl for 10 minutes (+NaN_3/NH_4Cl, lower row). Scale bar indicates 10 µm. Reproduced in part & modified with permission from Burgstaller et al., 2019; © American Chemical Society

We suggested that, when administered to cells, azide and ammonia might diffuse into the lumen of the vesicle, thereby buffering high [H^+] (**Fig. 16a**)(176). To test our assumption, HeLa cells expressing pH-Lemon – GPI were analyzed using high resolution microscopy. As expected, the comparison of the mTurquoise2 and EYFP signals of untreated cells revealed many acidic vesicles, possessing strong mTurquoise2 fluorescence, but weak or no EYFP signal, leading to the previously observed color-coding including all five differently colored vesicle groups (**Fig. 16b**). The same cells were subsequently imaged after addition of an alkaline buffer containing NaN_3 and NH_4Cl. This mixture strongly affected the intracellular pH, as it increased vesicular pH levels remarkably (**Fig. 16b**)(176). Upon image acquisition 10 minutes after treatment, the formerly quenched EYFP signal was retained, while the mTurquoise2 signal was mildly decreased (176). The increase of vesicular pH levels was clearly visible in pseudo-colored ratio images that displayed mainly blue, cyan and some green vesicles. Highly acidic, red vesicles could not be detected in cells that were treated with NaN_3 and NH_4Cl (**Fig. 16b** & **Fig. 17b**)(176). Interestingly, zooming into the vesicular region revealed that the effect of these compounds seemed to be quite heterogeneous. Although the neutralizing effect of the compound is rather strong, not every vesicle was completely neutralized, and some vesicles possessing a mild acidic pH can still be observed (**Fig. 17b**)(176). However, this experiment confirmed our hypothesis that pH-Lemon is highly stable and not degraded in acidic environments, which favors dynamic long-time pH imaging using vesicular targeted pH-Lemon.

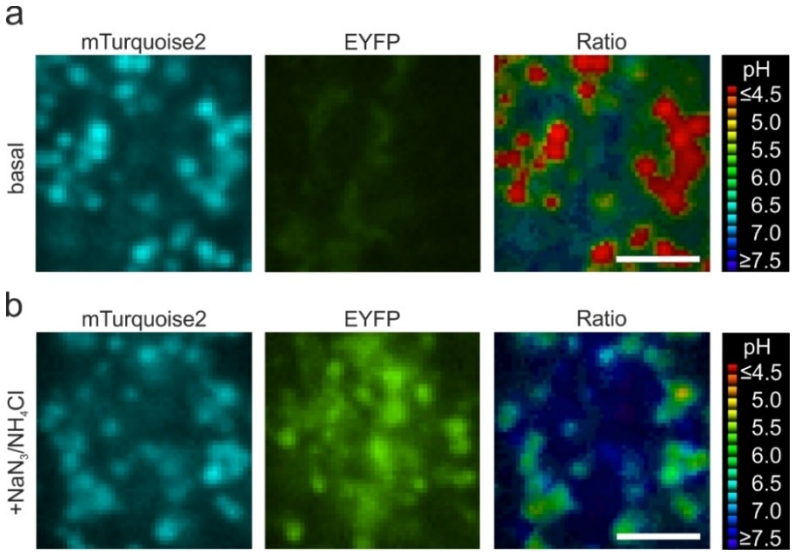

Figure 17: Heterogeneous response of intracellular vesicles upon treatment with neutralizing agents. Representative images of HeLa cells transfected with pH-Lemon – GPI with zoom into a region of high vesicular density. mTurquoise2 (left panels), EYFP (middle panels) and pseudo-colored ratio image (right panels) are displayed under untreated control conditions (basal) **(a)** or after treatment with NaN_3/NH_4Cl for 10 minutes **(b)**. Scale bars represent 10 µm. Estimated pH values according to the ratio are given. Reproduced in part & modified with permission from Burgstaller et al., 2019; © American Chemical Society

4.17 Precise real-time determination of vesicular pH values using pH-Lemon - GPI

Our previous experiments already proved the stability of pH-Lemon – GPI in acidic environments and the ability of the probe to detect pH alterations in extremely small structures. Nevertheless, these protocols represent end-point measurements with high-resolution. In order to test the suitability of pH-Lemon to resolve pH changes in real-time, HeLa cells transfected with pH-Lemon – GPI were analyzed on a wide-field microscope over-time. Despite the significant lower resolution of the wide-field microscope, the region of high vesicle density (i.e. ROI, region of interest) as well as single vesicles possessing different pH values from acidic to almost neutral could be detected (**Fig. 18a**)(176). Over a period of 10 minutes, the average pH of the ROIs slightly decreased (**Fig. 18b**). While the pH seemed rather stable and did not show spontaneous and obvious alterations, the basal pH of the vesicular regions differed from cell to cell. Interestingly, we could observe a huge heterogeneity of the average vesicular pH, with pH values ranging from 5.3 to 5.8 (**Fig. 18b**)(176). In order to test the responsiveness and the velocity of vesicle targeted pH-Lemon to detect pH alterations, we again neutralized these vesicles using NaN_3/NH_4Cl. Upon administration of NaN_3/NH_4Cl, a similar effect as observed using high-resolution microscopy was measured. Administration of these compounds resulted in a decreased number of acidic, i.e. red, vesicles (**Fig. 18a**), and the pH increased within a few seconds, resulting in an increase of around 0.3 pH units in the average vesicular region (**Fig. 18c**)(176). Due to the prominent effect of NaN_3/NH_4Cl, we expected the neutralization to be irreversible. Unexpectedly, a wash-out of the chemicals resulted in a decrease (i.e. re-acidification) of the vesicular pH that was significantly slower than the neutralization (**Fig. 18c**)(176). After wash-out, the basal pH levels were reached again after ~3 minutes (**Fig. 18c**) and the number of red, acidic vesicles seemed to be increased (**Fig. 18a**)(176). Furthermore, we aimed to compare the response of pH-Lemon – GPI to LysoTracker Red DND-99, representing a frequently used staining method for acidic vesicles. The dye functions in an intensiometric manner, which strongly depends on the pH (192). Due to very heterogenous staining efficiencies, the measured intensities of HeLa cells stained with LysoTracker Red DND-99 scattered a lot (**Fig. 18d**). Upon vesicle neutralization, the intensity dropped unitl no fluorescence was measurbale any more (**Fig. 18d** & **18e**)(176). Wash-out of NaN_3/NH_4Cl did not restore LysoTracker Red DND-99 fluorescence, probably due to its irreversible loss upon neutralization (**Fig 18d** & **18e**)(176). These experiments clearly indicated the advantages of the genetically-encoded pH sensor pH-Lemon for staining of vesicles and precise, dynamic and reversible pH measurements.

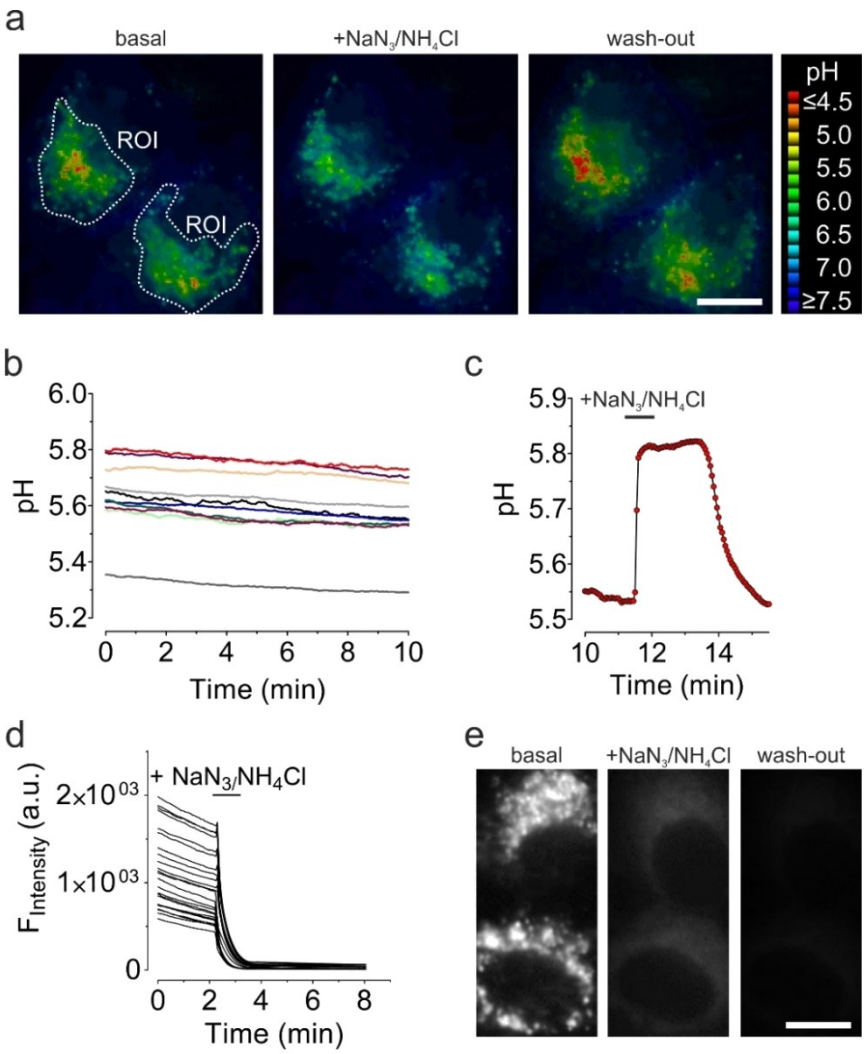

Figure 18: Dynamic real-time measurements of vesicular pH changes. (a) Pseudo-colored ratio images of HeLa cells transfected with pH-Lemon – GPI under resting conditions (basal, left panel), in response to NaN_3/NH_4Cl (middle panel) and after wash-out (right panel). The measured region of interest (ROI) is displayed. Scale bar represents 10 µm. n=10 cells from 3 independent experiments. **(b)** Representative single cell responses of cells transfected with pH-Lemon – GPI over-time. The average pH of the intracellular region with high vesicle density (ROI) was determined using wide-field microscopy over a period of 10 minutes. n=3 **(c)** Representative pH curve of a single cell in response to NaN_3/NH_4Cl with subsequent wash-out and re-acidification of the vesicles. n=3 **(d**) Representative single cell responses of HeLa cells stained with LysoTracker Red DND-99 using the same protocol as in **(b)**. n= 45 cells from 3 independent experiments. **(e)** Representative fluorescence intensity images of LysoTracker Red DND-99 stained HeLa cells under basal conditions (left panel), treated with NaN_3/NH_4Cl (middle panel) and after wash-out (right panel). Scale bar represents 10 µm. Reproduced in part & modified with permission from Burgstaller et al., 2019; © American Chemical Society

4.18 pH-Lemon is suitable to monitor V-ATPase activity

The activity of V-ATPases in the vesicular membrane is essential for the generation of an acidic lumen (99)(**Fig. 19a**). Inhibition of the H^+ pump is known to cause defects in vesicular acidifiction, leading to an increased luminal pH (110). To test the suitability of pH-Lemon for the detecetion of V-ATPase activity by monitoring the vesicular pH, we aimed to alter the luminal pH levels via application of the commonly used V-ATPase inhibitor Baf-A (110,176) (**Fig. 19a**).

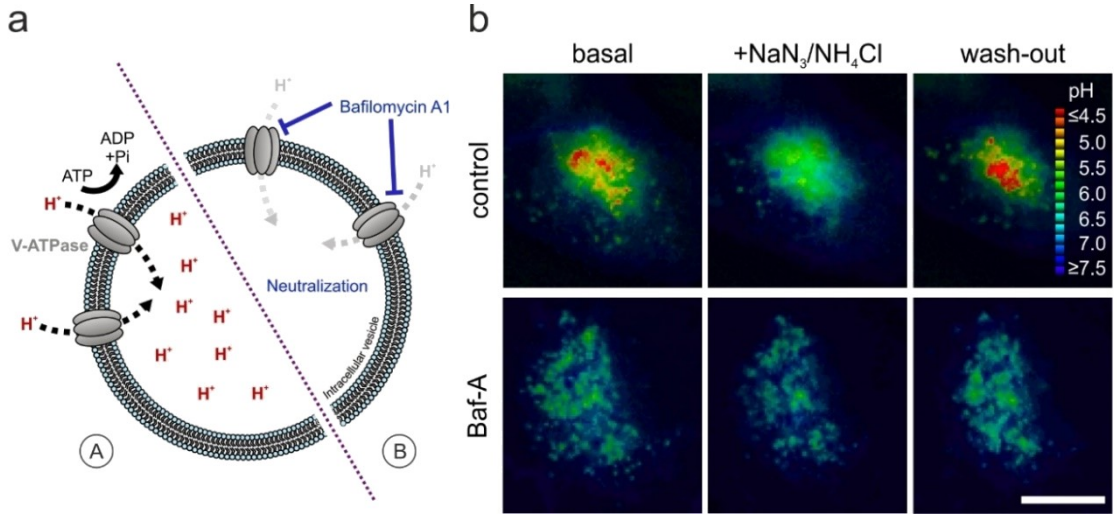

Figure 19: Monitoring vesicular pH as a measure of V-ATPase activity. (a) Schematic drawing of the proposed mechanism by which V-ATPases (grey) located in the vesicular membrane pumps H^+ into the lumen, thereby acidifiying the vesicle (A). Application of Baf-A is thought to inhibit V-ATPase activity, thereby leading to an increased luminal pH (B). **(b)** Representative pseudo-colored ratio images of control HeLa cells (upper row) and Baf-A treated cells (lower row) expressing pH-Lemon – GPI. Images are representative for the vesicluar pH levels in basal conditions (left column), after treatment with NaN_3/NH_4Cl (middle column) and after wash-out (right column). Scale bar respresents 10 µm, estimated pH levels are indicated. n=8 for both conditions. Reproduced in part & modified with permission from Burgstaller et al., 2019; © American Chemical Society

In comparison to control HeLa cells, treament with Baf-A caused an increased basal pH in intracellular vesicles (176). While control cells possessed a huge heterogeneity concerning their vesicluar pH levels, ranging from an estimated pH of 6.5 to 4.0, Baf-A treated cells mainly contained vesicles with an estimated pH of 6.0 or higher (**Fig. 19b**)(176). We assumed that the substances might have only a small or no effect in Baf-A treated cells, due to vesicular pre-neutralization by Baf-A. As expected, control cells responded to neutralization by NaN_3/NH_4Cl with a clear increase of vesicular pH levels with a subsequent re-acidification upon wash-out (**Fig. 19b**)(176). In contrast, the pH alteration in Baf-A treated cells was hardly visible in pseudo-colored ratio images.

Due to the constant inihibition of the V-ATPase, the vesicles re-acidified only to their basal pH levels, but did not reach extremely acidic values (**Fig. 19b**)(176). Using real-time imaging, we aimed to determine the exact pH values of the measured vesicular regions (**Fig. 20**). Compared to control cells, possessing average basal pH levels of the vesicular region of 5.9 ± 0.02, the pH of Baf-A treated cells was found to be significatly increased to 6.2 ± 0.02 (**Fig. 20a**)(176). Due to the already neutralized vesicles in Baf-A treated cells, addition of NaN_3/NH_4Cl caused a milder increase of the pH compared to control cells (**Fig. 20c** & **Fig. 20d**)(176). Noteworthy, there was still a neutralizing effect of NaN_3/NH_4Cl in both groups, that showed the same kinetics upon NaN_3/NH_4Cl administration. Removal of NaN_3/NH_4Cl led to the already previously observed re-acidification in control cells, while the effect was hampered in Baf-A treated cells (**Fig. 20a**, **Fig. 20c** & **Fig. 20d**)(176).

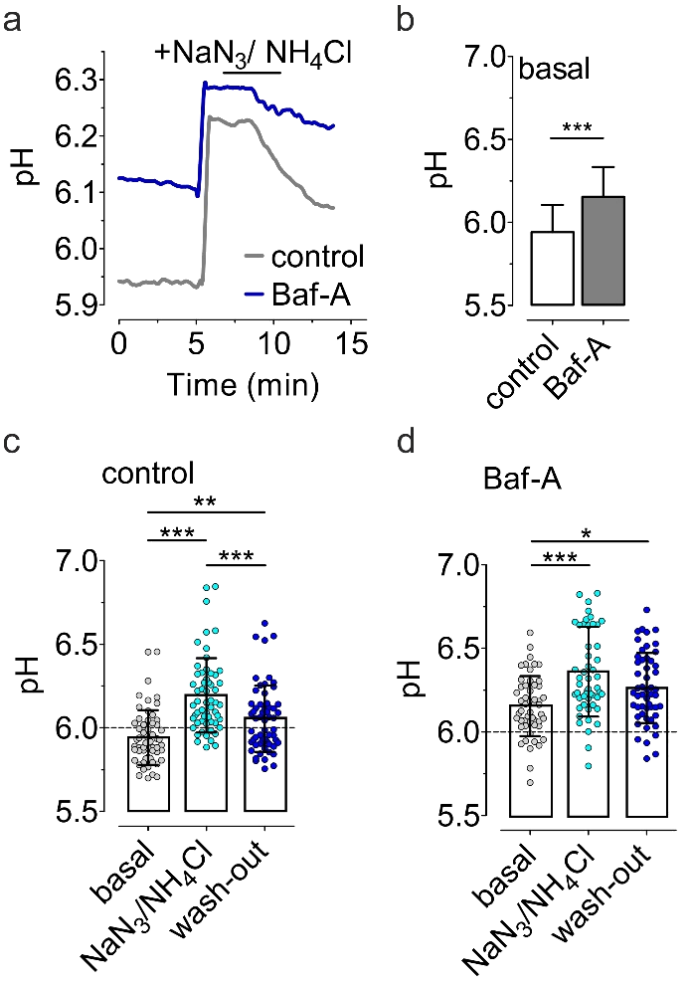

Figure 20: Dynamic real-time determination of pH values to resolve V-ATPase activity. (a) Representative real-time pH curve over-time of a control (grey curve) and a Baf-A treated cell (blue curve) in response to administration of NaN_3/NH_4Cl, followed by a subsequent wash-out as indicated in the panel. **(b)** Average pH values ± SD of the vesicular region of HeLa cells transfected with pH-Lemon – GPI in control (white bar) and Baf-A treated cells (grey bar). n=8 for both conditions, unpaired t-test, ***p<0.001. **(c)** Average pH values ± SD (bars) with each replicate (dots) of the pH values of control cells under basal conditions (grey dots), neutralized (cyan dots) and after wash-out (blue dots). n=8, **p<0.01, ***p<0.001, one-way ANOVA with Tukey's post-hoc test. **(d)** Average pH values ± SD (bars) with each replicate (dots) of the pH values of Baf-A treated cells under basal conditions (grey dots), neutralized (cyan dots) and after wash-out (blue dots). n= 8, p*<0.05, p***<0.001, one-way ANOVA with Tukey's post-hoc test. Reproduced in part & modified with permission from Burgstaller et al., 2019; © American Chemical Society

4.19 Extracellular pH strongly affects vesicular pH levels

The pH of intracellular vesicles seems to respond quickly, but reversibly to events causing vesicular pH neutralization, under conditions where the V-ATPases are not inhibited. Considering the metabolic settings within the TME, the pH_{ex} levels are lowered due to increased export of H^+ and lactate (129,130). As these decreased pH levels might distress the surrounding cells, we aimed to investigate, to which extend the intracellular vesicles are affected and how they respond to pH_{ex} changes (**Fig. 21**)(176). To test the effect of different pH_{ex} levels on the vesicular pH, images of HeLa cells transfected with pH-Lemon – GPI were acquired in response to various, acidic pH_{ex} levels.

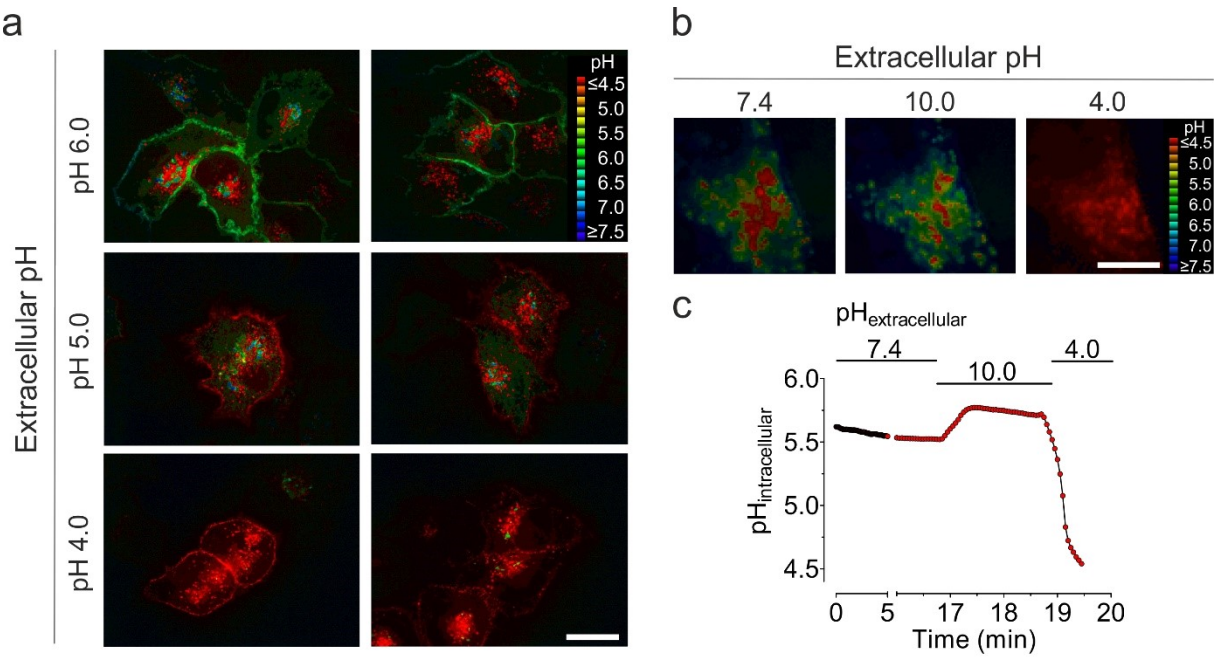

Figure 21: Effect of extracellular pH alterations on vesicular pH levels. (a) Pseudo-colored ratio images of HeLa cells expressing pH-Lemon – GPI, acquired using high-resolution microscopy, in response to pH_{ex} levels of 6.0 (upper row), 5.0 (middle row) and 4.0 (lower row). Scale bar represents 10 µm. **(b)** Representative pseudo-colored ratio images of intracellular vesicles containing pH-Lemon – GPI in response to switching pH_{ex} values of 7.4 (left image), 10.0 (middle image) and 4.0 (right image) as indicated in the panel. Scale bar represents 10 µm. **(c**) Representative pH response of the vesicular region of a single living cells displayed in **(b)** upon changing the pH_{ex} from 7.4, to 10.0 and 4.0 over time. n=5. Reproduced in part & modified with permission from Burgstaller et al., 2019; © American Chemical Society

As expected, the sensor located at the outer plasma membrane displayed the pH values of 6.0, 5.0 and 4.0 that were adjusted in the buffer. At a pH of 6.0, many acidic vesicles having a pH ~4.0 and several vesicles having a pH ~6.0 could be observed within these cells. Upon acidification, the vesicular pH levels acidified rapidly, with some less acidic structures of bigger size visible within the cytosol at a pH_{ex} of 5.0 (176).

Finally, acidic pH_{ex} values of 4.0 strongly affected intracellular pH levels, resulting in acidification of nearly all structures containing the sensor, i.e. the Golgi complex and the vesicles (**Fig. 21a**). Dynamic wide-field measurements displayed the strong pH dependent effect on the vesicles upon changing pH_{ex} levels. While there were some acidic vesicles visible at the beginning of the measurements with extracellular pH 7.4, which represents physiological pH_{ex} values, the number of highly acidic vesicles decreased upon changing to an alkaline buffer (**Fig. 21b**)(176). Interestingly acidic pH values had a more prominent effect on the vesicular pH compared to alkaline pH levels, rapidly acidifying all pH-Lemon – GPI positive structures (**Fig. 21b**)(176). This effect was confirmed during dynamic recordings of the vesicular pH levels, where administration of a buffer with pH 10.0 led to a small, slow increase of the average vesicular pH from 5.5 to 6.0, whereas changing the pH to 4.0 caused a fast, massive drop of the pH to 4.5 within some seconds (**Fig. 21c**)(176). These experiments indicate, that extracellular acidic pH levels, as they occur within the TME, might affect pH_i levels and therefore, hamper or even re-program cell metabolism.

4.20 Novel approach for targeting pH-Lemon solely to the plasma membrane

Monitoring pH_{ex} levels in terms of cell metabolism alterations or cell-to-cell signaling might represent a valuable tool to gain a better understanding of the cascades occurring within the TME or during intercellular communication (193,194). However, precise measurements of pH_{ex} levels are challenging using conventional targeting signals, such as the GPI-anchor, due to a high background signal arising from the intracellular vesicles (176). In order to measure accurately on the plasma membrane, we re-designed a sophisticated approach for exploiting the biotin-avidin interaction (160,163,164). Considering the fact that many genetically-encoded sensors are still fully functional as purified proteins extracted from *E.coli*, we hypothesized, that coupling recombinant purified pH-Lemon to a biotin residue located at the plasma membrane might represent the first method to obtain an immobilized, fully functional sensor measuring pH_{ex} levels (134,137,195). For that purpose, we generated two constructs for transfection into mammalian cells. The first construct encoded for the mCherry tagged AviTag fused to CDH13 and a GPI-anchor for membrane localization (**Fig. 22a**).

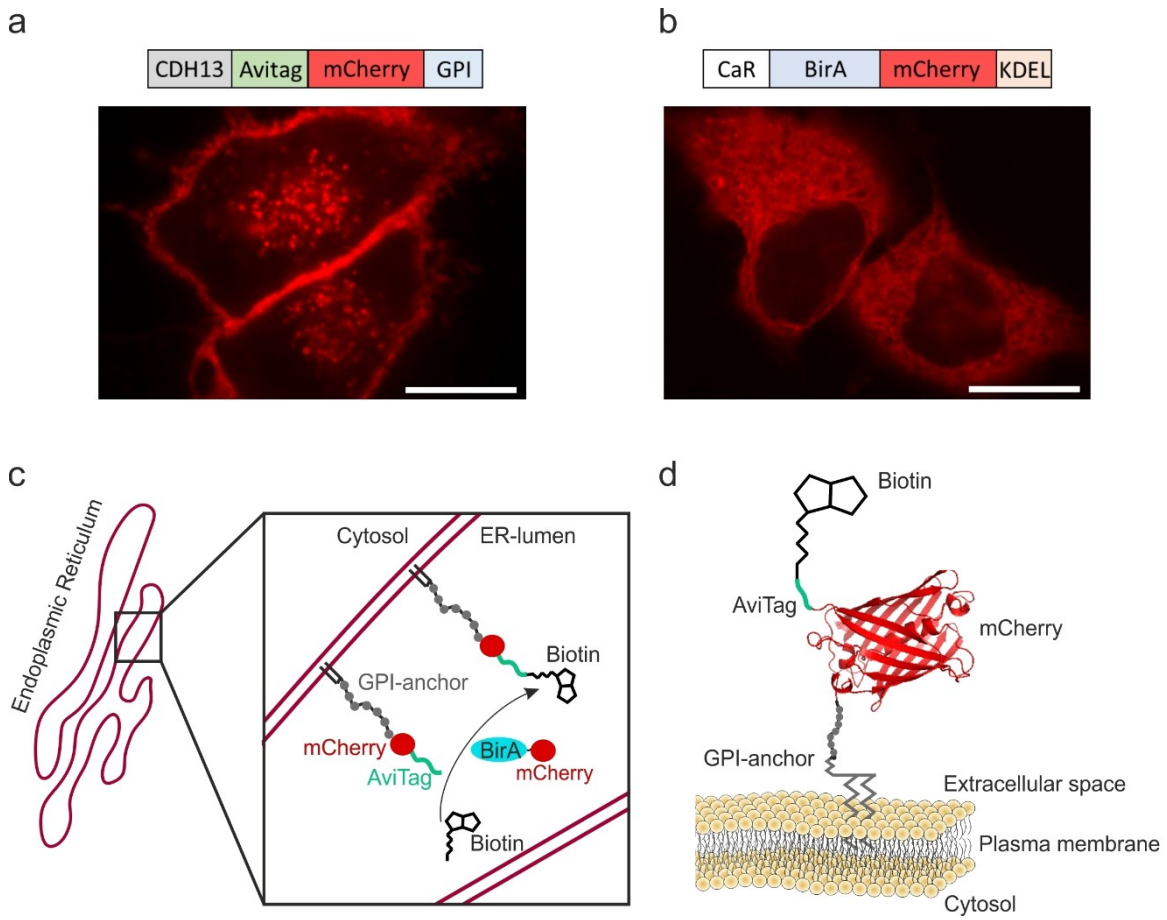

Figure 22: Expression of AviTag and the enzyme biotin ligase (BirA) to obtain membrane-bound biotin. (a) Schematic drawing (upper panel) of a construct encoding for the CDH13 targeting sequence (grey square), followed by the 15 amino acid long AviTag (green square), the fluorescent protein mCherry (red square) and the GPI-anchor signal (blue square) on the C-terminal end. Lower panel displays a representative fluorescence image of HeLa cells expressing the the AviTag-mCherry construct. Scale bar indicates 10 µm. **(b)** Schematic illustration (upper panel) of a construct encoding for the Calreticulin targeting sequence (CaR, white square), BirA (blue square), mCherry (red square) and four amino acids acting as ER retension signal (KDEL, orange square). Representative fluorescence image of HeLa cells expressing the BirA-mCherry construct, acquired using high-resolution microscopy. Scale bar indicates 10 µm. **(c)** Proposed mechansim and zoom of the events occuring in the ER upon expression of the constructs described in **(a)** and **(b)**. The ER targeted BirA (cyan) fused to mCherry (red) is located in the lumen of the ER. Due to the CDH13 targeting signal, the AviTag-mCherry-GPI construct is transpoted into the ER, where the GPI-anchor binds to the membrane. If biotin is present, BirA catalyses the reaction to bind biotin to the AviTag (green). **(d)**. After adding biotin to the AviTag **(c)**, the construct is transported to the plasma membarne via the Golgi complex and the secretory vesicles to reach its final localization at the outer side of the plasma membrane (yellow). The GPI-anchor is inserted into the membrane, followed by mCherry (red) and the biotinylated AviTag (black and green).

Expression of this construct led to the known pattern of mild ER and high vesicle, as well as high plasma membrane staining, as previously observed expressing pH-Lemon – GPI (**Fig. 14a** & **Fig. 22a**). The second construct encoded for BirA, an enzyme derived from *E.coli* that is capable of biotinylating the AviTag, fused to mCherry (**Fig. 22b**)(196). Due to the CaR and ER retention signal KDEL fused to BirA, mCherry fluorescence was detected within the ER in HeLa cells expressing the construct (**Fig. 22b**). Co-transfection of these two constructs should finally result in the events displayed in **Fig. 22c**. The mCherry tagged BirA enzyme can be found in the ER due to the ER-targeting sequence. Before the AviTag-mCherry-GPI construct is packed into vesicles in order to be transported to the plasma membrane, it is also localized at the ER, where it is glycosylated. If biotin is present, BirA is responsible for the biotinylation of the AviTag (**Fig. 22c**). Afterwards, the biotinylated AviTag is transported to the Golgi complex, packed into secretory vesicles and trasported towards the plasma membrane. On the outer cell surface, the GPI-anchor is inserted into the plasma membrane, followed by mCherry, which favors the selection of transfected, fluorescent cells during fluorescence microscopy (**Fig. 22d**). The biotinylated AviTag, representing the N-terminal end of the construct, can be found exposed to the extracellular space (**Fig. 22d**).

4.21 Immobilization of purified sensors at the cell membrane using the traptavidin-biotin interaction

After expression of the respective constructs, biotinylation of the AviTag in the ER and transport to the outer side of the plasma membrane, the cells harbor a highly biotinylated surface, that, in theory, will be recognized by avidin counterparts. The non-covalent binding of biotin and avidin is the strongest known in nature, however, we aimed to further enhance the force of binding in order to minimize dissociation during dynamic measurements over-time using extracellular perfusion (156). Therefore, we took advantage of the recently developed traptavidin, with minimal dissociation rates and high stability over a wide pH range (166). This traptavidin was fused to pH-Lemon, the construct was expressed recombinantly in *E.coli* and purified. Incubation of the biotinylated cells with the purified sensor in solution should result in binding of traptavidin to biotin only at cells expressing both, the enzyme BirA and the biotinylated AviTag (**Fig. 23a**). Expression of both contructs resulted in a high mCherry fluorescence signal within vesicles and at the plasma membrane. The weaker ER signal of the BirA enzyme could not be distinguished from the the AviTag construct, since both mCherry-tagged constructs displayed mild ER signal. In accordance with our expectation, incubation of HeLa cells expressing BirA and the AviTag resulted in accurate staining of the cell surface after incubation with recombinant purified traptavidin-pH-Lemon (**Fig. 23b**).

Both fluorescence signals, the mTurquoise2 as well as the EYFP signal, were clearly detectable, regardless of a high or weak expression level of the mCherry constructs (**Fig. 23b**). The precise staining solely at the cell border favors measurements at the cell surface, as the background signals are minimized. Compared to the pH-Lemon – GPI construct, that could be found to a great extent also in intracellular vesicles, the purified sensor bound to biotin should only display pH changes occuring in the extracellular space (**Fig. 23b**). Importantly, no unspecific binding of the sensor could be detected, as cells lacking AviTag-mCherry and BirA-mCherry did not show any mTurquoise2 or EYFP fluorescence after coupling (**Fig. 23b**).

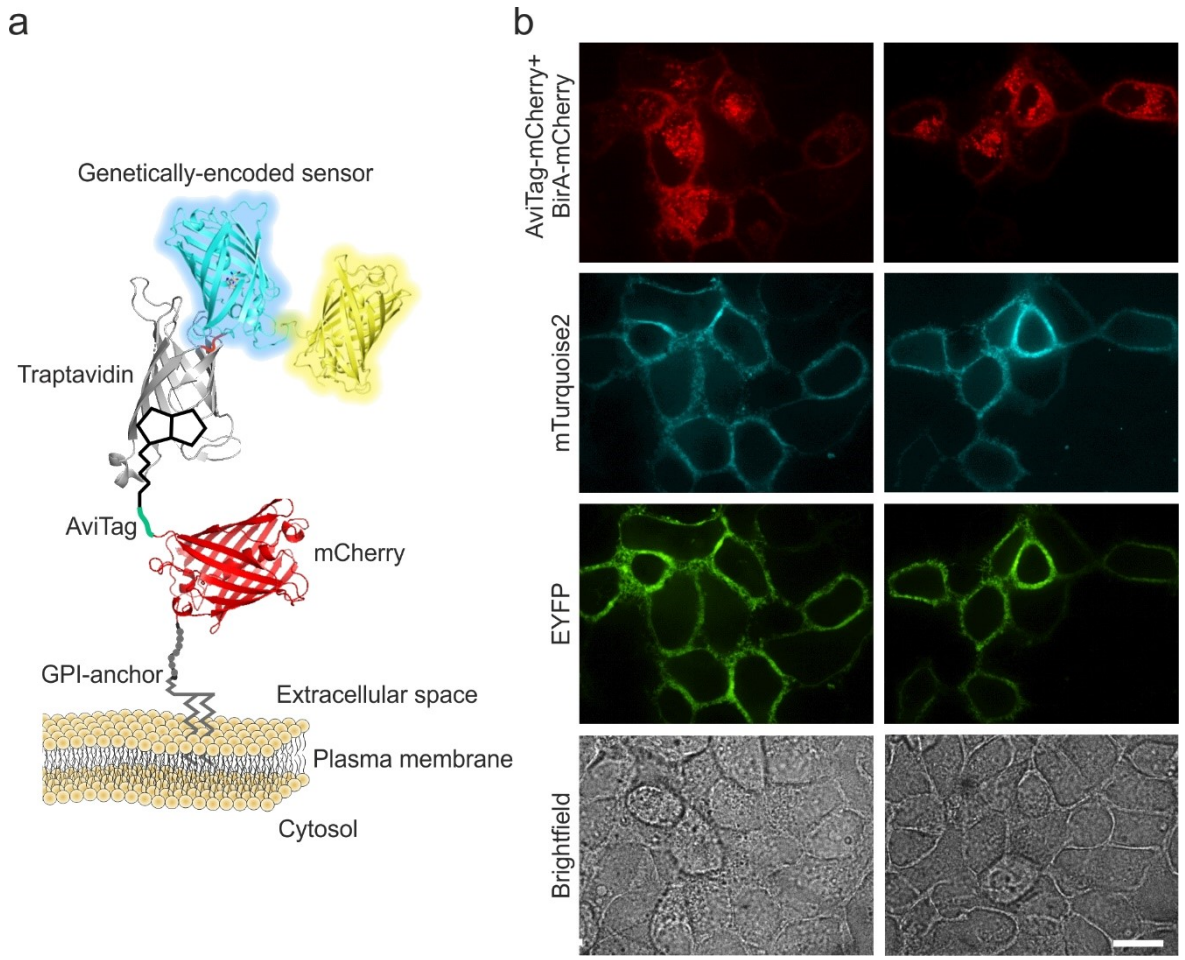

Figure 23: Cell surface labelling with traptavidin-pH-Lemon. (a) Schematic drawing of the purified construct consisting of traptavidin (grey) fused to pH-Lemon (cyan+yellow) with a flexible $(GGGGS)_2$-linker (red). Traptavidin is able to bind the biotinylated AviTag (black and green), which can be found on the N-terminal end of mCherry (red). The C-terminal end of the FP is connected to the GPI-anchor (grey), which is inserted into the plasma membrane (light yellow). **(b)** Representative fluorescence emission images of HeLa cells expressing BirA-mCherry and AviTag-mCherry-GPI using ACLSM. Displayed are the mCherry fluorescence (first row), the mTurquoise2 fluorescence (second row), the EYFP fluorescence (third row) and the brightfield image (fourth row). Scale bar indicates 20 µm.

4.22 Precise monitoring of extracellular pH alterations using purified traptavidin-pH-Lemon bound to biotin

After successfully attaching the purified sensor to the plasma membrane, as confirmed using ACLSM imaging, we aimed to measure pH_{ex} alterations in real-time. Therefore, we measured HeLa cells with bound traptavidin-pH-Lemon using wide-field microscopy in response to different pH_{ex} values. Until now, it has been challenging to measure sensor responses directly at the cell surface using wide-field microscopy with lower resolution, due to the blurring signals from the cell border and the intracellular vesicle background (176). Using our novel approach, the cell surface was clearly visible even at low resolution (**Fig. 24a**). Due to the restriction of the signal to the membrane, the whole cell can be measured as the region of interest (ROI) (**Fig. 24a**), without measuring any unwanted artefacts.

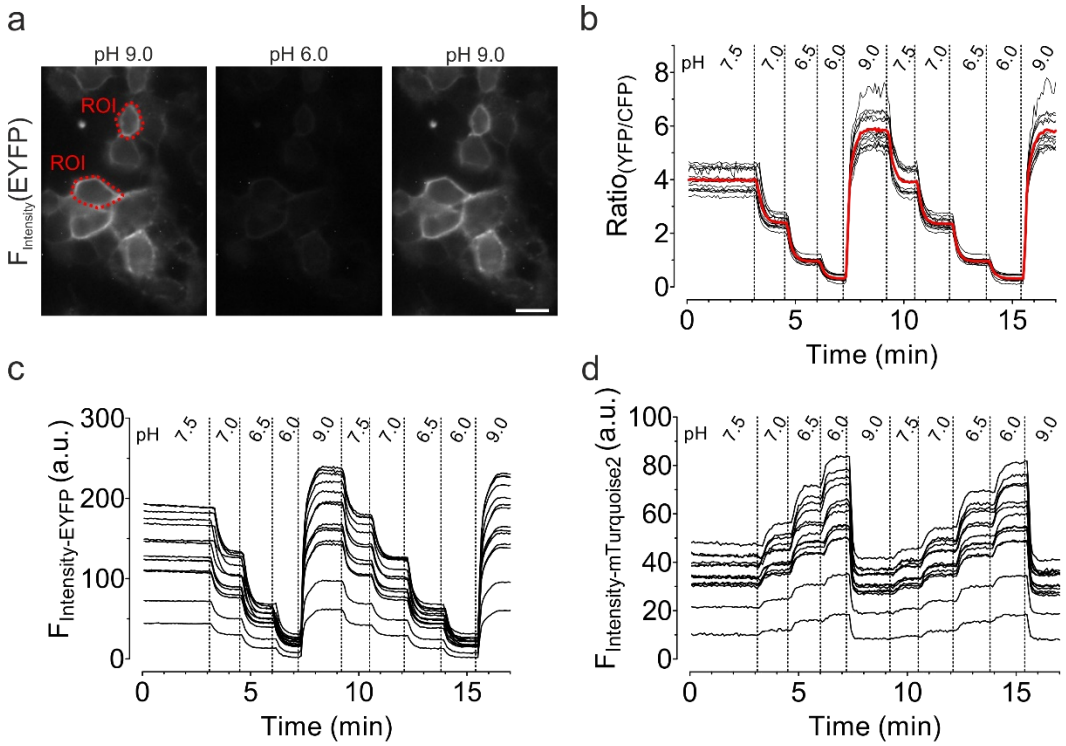

Figure 24: Dynamic real-time imaging of traptavidin-pH-Lemon bound to biotinylated AviTag. (a) Representative EYFP fluorescence signals of HeLa cells transfected with BirA-mCherry and AviTag-mCherry-GPI after coupling with traptavidin-pH-Lemon. Cells were perfused with buffers of different pH values and wide-field images were acquired at a pH of 6.0 or 9.0 Scale bar represents 20 µm. **(b)** pH responses over-time of HeLa cells coupled with traptavidin-pH-Lemon and ROIs as depicted in **(a)** in response to different pH values from 6.0 to 9.0. Single cell responses are displayed in black, average response is shown in red. **(c)** Fluorescence intensity over-time of EYFP of the ratio curves displayed in **(b)**. **(d)** Fluorescence intensity over-time of mTurquoise2 of the ratio curves displayed in **(b)**. n=3 for all panels.

Interestingly, the recombinant purified sensor totally retained its functionality upon immobilization at the cell surface. Traptavidin-pH-Lemon reported pH changes of extracellular buffers in a fast, accurate and repetitive way with a high signal-to-noise ratio (**Fig. 24b**). Importantly, the basal ratios of the cells were in a very narrow range, with an average ratio of 4.0 (**Fig. 24b**), indicating the accuracy of this method. The ratiometric design of pH-Lemon favors measurements with a low fluorescence intensity, as the sensor was sensitive to pH changes, regardless of the fluorescence intensities of EYFP (**Fig. 24c**) and mTurquoise2 (**Fig. 24d**), displaying a strong dependency on (de-)protonation (**Fig. 24b – Fig. 24d**).

4.23 Recording extracellular K^+ changes at the cell surface

Besides pH alterations occurring as a result of the metabolic setting of cells, for example, within the TME, especially extracellular K^+ alterations are of great importance (129,197). The highly K^+ sensitive and recently developed genetically-encoded K^+ ion indicators (GEPIIs) led to new insights into intracellular K^+ homeostasis, by recording K^+ changes as a result of de- or increased FRET efficiency upon K^+ binding to Kbp, the K^+ binding protein (134,198). Especially GEPII 1.0, a highly sensitive K^+ variant, has the potential to monitor K^+ changes that might occur within the extracellular environment, due to its high K^+ affinity (134,197). However, although GEPII 1.0 expressed in the cytosol of HeLa cells responded to K^+ changes from 0 mM to 100.0 mM accurately (**Fig. 25a** & **Fig. 25b**), measuring K^+ in the extracellular space remained impossible. Using the GPI-anchor, GEPII 1.0 was successfully targeted to the outer side of the plasma membrane, as confirmed using wide-field imaging microscopy (**Fig. 25a**). However, although the fluorescence of both FPs was detectable, the sensor did not respond upon changing the $[K^+]$ in the extracellular space from 0 mM to 100.0 mM, suggesting that intracellular modifications might result in fluorescent, but non-functional sensors. Interestingly, the number of vesicles seemed to be reduced, compared to cells expressing pH-Lemon – GPI, but instead of localization within vesicles, a higher signal of sensor localized within or at the ER could be detected (**Fig. 25a**).

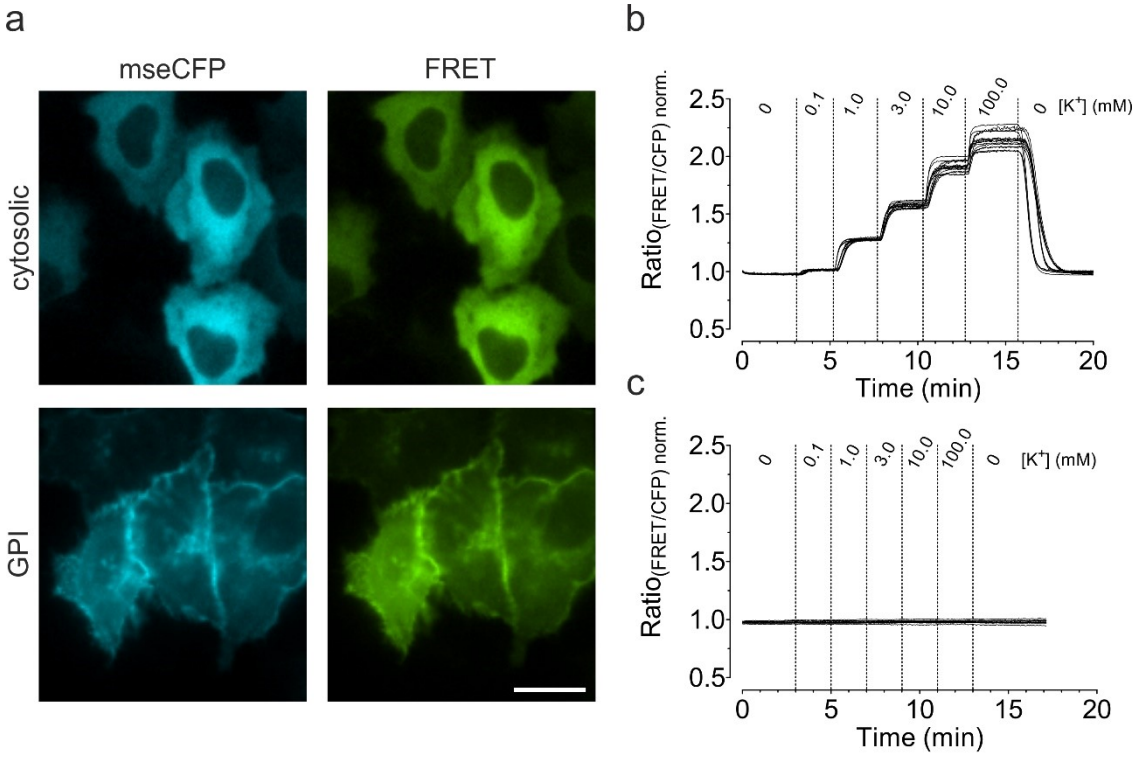

Figure 25: Targeting of GEPII 1.0 to the plasma membrane via a GPI-anchor caused K^+ insensitivity. (a) Representative wide-field images of the mseCFP and FRET fluorescence emission signals of HeLa cells expressing cytosolic GEPII 1.0 (upper panels) and GPI-anchored GEPII 1.0 (lower panels). Scale bar indicates 10 µm. **(b)** Single cell responses of 3 independent measurements of HeLa cells expressing cytosolic GEPII 1.0 in response to increasing K^+ levels as indicated in the panel. Cells were permeabilized using 15 µM gramicidin. **(c)** Single cell responses of HeLa cells expressing GPI-anchored GEPII 1.0 in response to increasing K^+ levels over-time as indicated in the panel. n=3.

4.24 Fusion of traptavidin to GEPII does not impair structural rearrangement *in vitro*

Considering the successful application of purified pH-Lemon to measure pH at the cell border, we hypothesized, that the binding of recombinant traptavidin-GEPII 1.0 to the biotinylated AviTag may allow extracellular K^+ measurements directly at the cell membrane for the first time. For this purpose, we generated a fusion construct of traptavidin and GEPII 1.0, which was purified analogously to the pH sensor. In contrast to pH-Lemon, which does not rely on a conformational rearrangement of the two FPs to measure pH alterations, K^+ sensing by GEPII 1.0 requires a structural rearrangement altering FRET-efficiency (134,176). However, the addition of a rather huge traptavidin protein might have a negative impact on the sensor functionality or even impair K^+ binding. In order to exclude these possibilities, the protein was analyzed on a fluorescence plate reader in response to various [K^+].

Despite addition of the rather huge traptavidin protein, the size of the additional fusion construct seemed to have no impact on K^+ sensing, as spectral analysis of the protein confirmed a strong dependency on [K^+] *in vitro* (**Fig. 26a**). The estimated EC_{50} of recombinant traptavidin-GEPII 1.0 of 544 µM (501.4 - 590.8) seemed to be perfectly suitable for the detection of extracellular K^+ changes (**Fig. 26b**), that are thought to occur in the µM or small mM range.

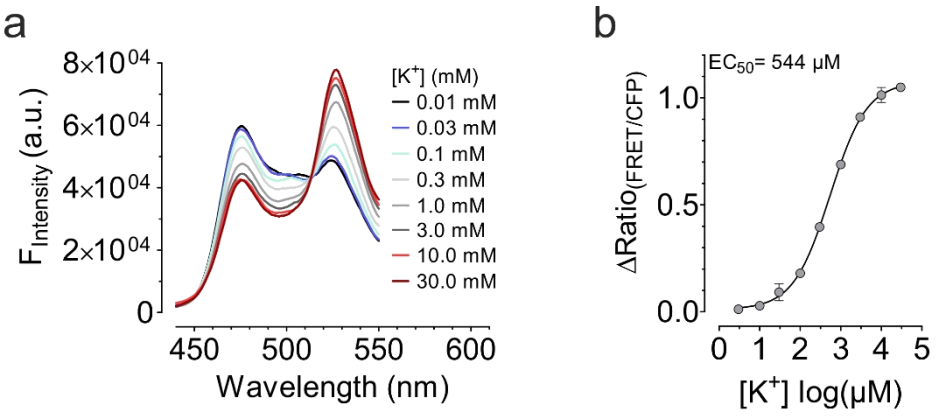

Figure 26: Purified traptavidin-GEPII 1.0 accurately measures [K^+] *in vitro*. (a) Fluorescence emission spectrum of purified traptavidin-GEPII 1.0. The protein was measured in aqueous solution using fluorescence spectrometry in response to different [K^+] of 10 µM, 30 µM, 100 µM, 300 µM, 1 mM, 3 mM, 10 mM and 30 mM. **(b)** Concentration response curve of traptavidin-GEPII 1.0 determined using the same [K^+] as displayed in **(a)**.

4.25 Traptavidin-GEPII 1.0 remains functional upon immobilization at the cell surface

We could show that addition of traptavidin does not hamper the sensitivity of GEPII 1.0 for K^+. Nonetheless, the protein was measured *in vitro* with the ability to move and adapt to essential conformational changes upon K^+ binding. To test the suitability of the construct to measure K^+ upon its immobilization *in situ*, we aimed to bind the traptavidin-GEPII 1.0 protein on biotinylated surfaces of HeLa cells. As expected, BirA and AviTag expressing cells displayed a clear membrane staining of mseCFP and FRET fluorescence upon incubation with the purified traptavidin-GEPII 1.0 (**Fig. 27a**). The signals received from traptavidin-GEPII 1.0 seemed to be homogenously distributed among the cell border of single cells, with variable intensities detected on different cells (**Fig. 27a**). In contrast to the measurements *in vitro*, the sensor bound to the cell surface might be forced to stay in a restricted place with a decreased ability to move, due to a high abundance of sensor proteins within a small membrane area. In order to test the functionality of the sensor, the cells were measured using wide-field microscopy.

Exploiting the traptavidin-biotin interaction, it was possible for the first time to obtain functional K^+ sensitive GEPII 1.0 on the cell membrane, as extracellular K^+ changes could be measured precisely in real-time (**Fig. 27b**). The FRET ratio changes were clearly detectable with a low signal-to-noise ratio (**Fig. 27b**). Possessing an EC_{50} for K^+ of 3.2 mM (2.6 - 4.6) when bound to the cell surface (**Fig. 27c**), the sensor might be able to distinguish between slight changes of K^+ within cellular environments.

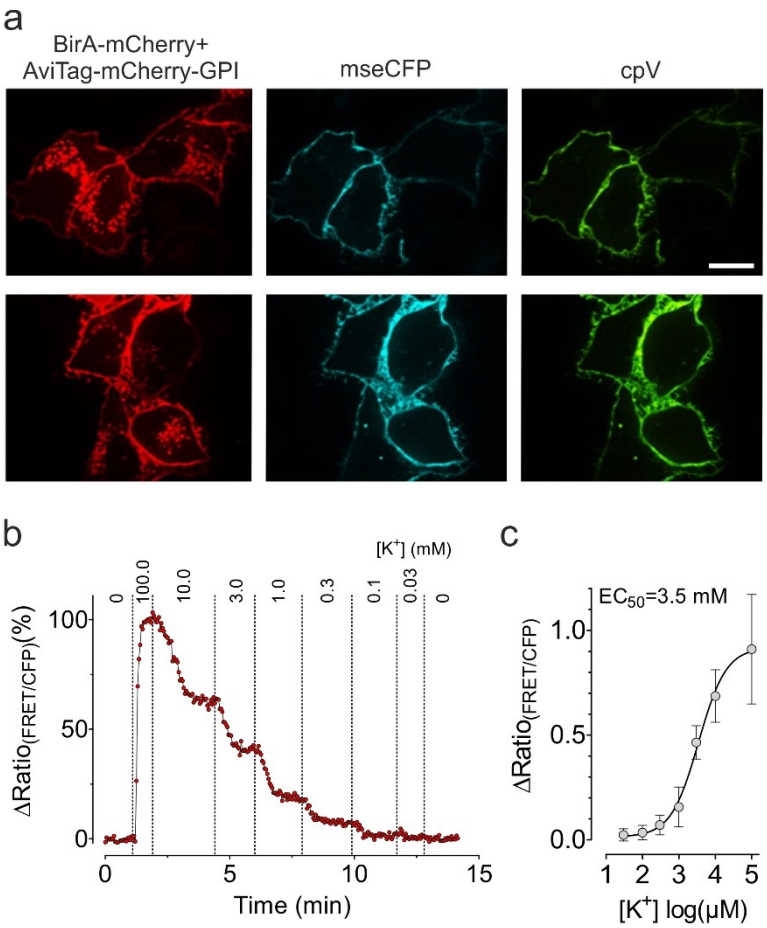

Figure 27: Traptavidin-GEPII 1.0 detects extracellular K^+ alterations at the cell surface. (a) Representative fluorescence emission images of HeLa cells expressing BirA-mCherry and AviTag-mCherry-GPI (left column). Middle and right images show the fluorescence of mseCFP (middle column) and FRET (right column) after incubation with traptavidin-GEPII 1.0. Scale bar represents 10 µm. **(b)** Dynamic real-time measurements of traptavidin-GEPII 1.0 bound to the surface of HeLa cells using wide-field microscopy. Representative single cell response of the K^+ sensor located at the cell membrane of a single living HeLa cell in response to different [K^+] administered using a perfusion system. n=3. **(c)** EC_{50} curve of the construct immobilized on the cell surface generated using measurements as shown in **(b)**. Values show average ± SD, n=3.

4.26 Immobilization of traptavidin fusion constructs on glass surfaces allows pH and K^+ determinations within fluids

Especially the field of biotechnology and biomedical analysis is constantly growing and in need of new designs and measurement techniques that improve and simplify the determination of biotechnologically and medically relevant parameters. Considering the strong binding of purified sensors fused to traptavidin on biotinylated cell surfaces, we hypothesized, that these purified sensors might also be stable on planar biotinylated surfaces like glass. Addition of the sensor of choice, would, in theory, result in immobilized sensors present on a glass slide to determine distinct parameters within biological samples. Contact of the fluids with the glass slides using perfusion might result in detectable FRET alterations, similar to the approach used on the cell surface (**Fig. 28a**).

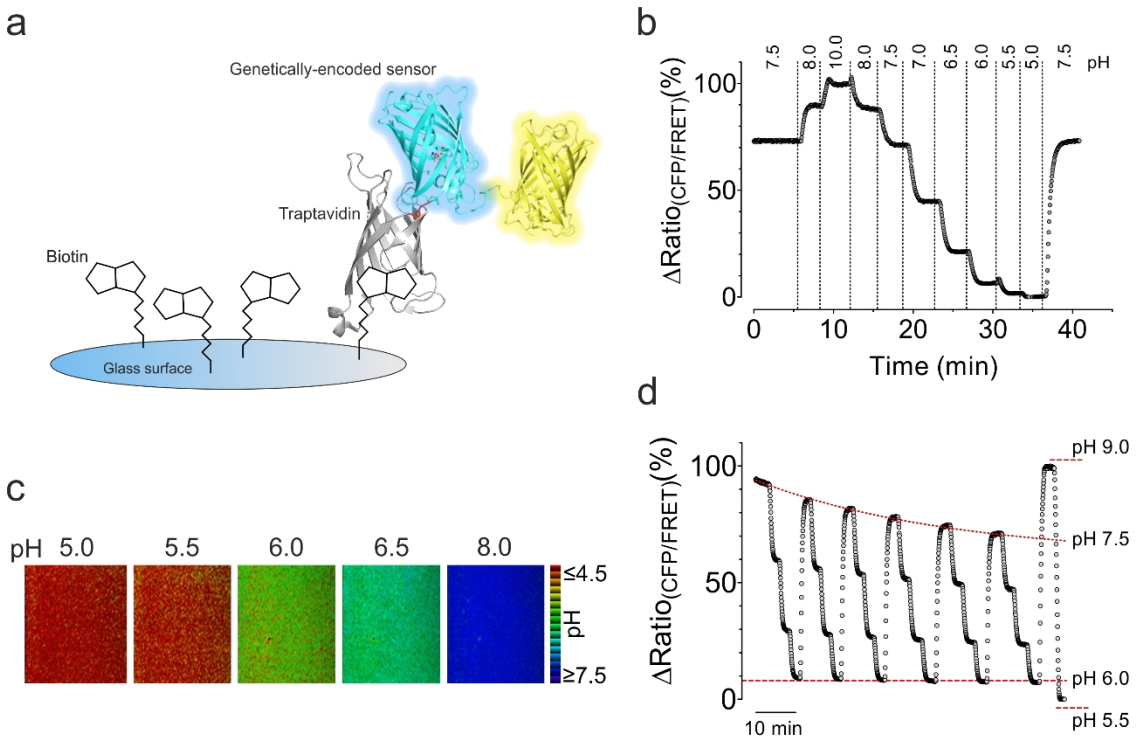

Figure 28: Binding traptavidin-pH-Lemon to glass surfaces allows long-term measurements and storage. (a) Schematic illustration of a biotinylated glass slide (light blue). Addition of a recombinant purified, genetically-encoded sensor fused to traptavidin should result in strong non-covalent binding and yield an immobilized sensor on the glass surface. **(b**) Representative pH response of immobilized pH-Lemon on a glass slide upon perfusion of distinct pH buffers over-time, as indicated in the panel. n=3. **(c)** Pseudo-colored ratio images of the area measured in **(b)** in response to different buffers with distinct pH values. **(d)** pH response of the glass slide measured in **(b**) after lyophilization and rehydration after 2 days of storage at -80°C.

First, we performed experiments using traptavidin-pH-Lemon and incubated biotinylated glass slides with the recombinant purified probe. As expected, the incubation of the biotinylated glass surfaces with purified sensor resulted in the binding of the sensor to the planar glass surface. Also on the glass surface, traptavidin-pH-Lemon responded to alterations in pH levels, with an extremely high signal-to-noise ratio (**Fig. 28b**). Although measuring for a long time with constant perfusion, the dissociation was negligible and the traptavidin-biotin interaction seemed to be pH stable over a pH range from 5.0 to 10.0 (**Fig. 28b**). Generation of pseudo-colored ratio images showed a similar color pattern as previously observed using different cell lines expressing pH-Lemon (**Fig. 28c**). It has already been demonstrated earlier, that GEPII 1.0 is suitable to do such measurements (134,195). However, still lots of recombinant protein had to be used and disposed after each single determination (134,195). Therefore, measuring K^+ by simply adding biological fluids to GEPII 1.0 immobilized on glass might represent a suitable tool to do such determinations in a high-throughput manner. Our experiments emphasize, that GEPII 1.0 is also suitable to measure K^+ alterations after immobilization on glass surfaces. Traptavidin-GEPII 1.0 was able to discriminate between different [K^+] ranging from 0.1 mM to 100 mM, covering the whole range of physiologically relevant extracellular [K^+] (**Fig. 29a**). Interestingly, the EC_{50} of traptavidin-GEPII 1.0 immobilized on glass was slightly elevated to 9.0 mM (5.8 – 14.0) in comparison to *in situ* experiments where the probe was immobilized on the cell surface (**Fig. 27c** & **Fig. 29b**).

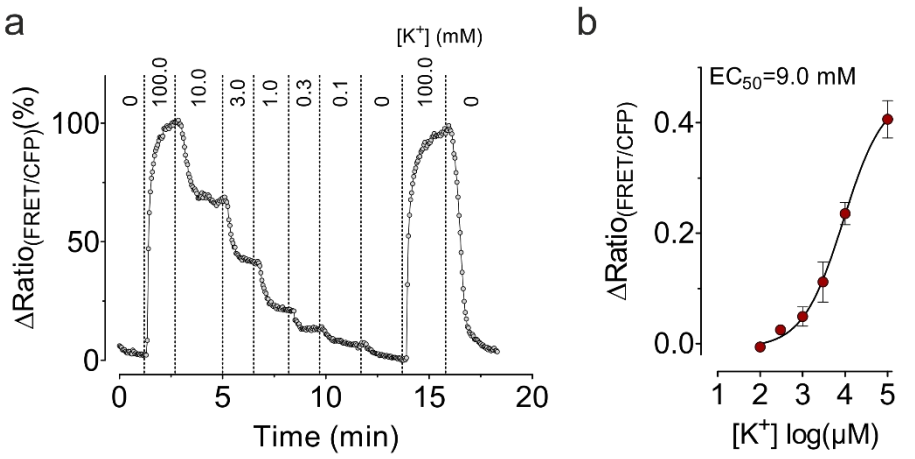

Figure 29: Immobilized traptavidin-GEPII 1.0 enables the determination of K^+ levels in fluids. (a) Representative response of traptavidin-GEPII 1.0 immobilized on biotinylated glass slides. Data were acquired using wide-field microscopy upon perfusion with buffers containing different [K^+]. n=3 independent experiments. **(b)** EC_{50} curve (n=3, average ± SD) of immobilized traptavidin-GEPII 1.0 on glass, determined from measurements as demonstrated in **(a)** in response to different [K^+].

Considering the experimental setup where one biotinylated glass slide is coupled with a large amount of recombinant protein to covering the whole glass surface, we aimed to reduce the coupling area and the protein volume to a minimum. We hypothesized, that this technique might be suitable to generate glass surfaces with several different sensors bound to it to determine many different parameters at once. This approach would represent a big improvement in terms of the experimental design, leading towards high-throughput analysis. Therefore, we first re-designed the method of protein application to the glass surface. During the first experiments described in **Fig. 28** and **Fig. 29**, the whole biotinylated glass slide was covered with a big volume of purified sensor protein (~600 µL), offering a surplus of the sensor in order to guarantee a high binding rate. We aimed to reduce the area, as well as the sensor amount by pipetting the sensor onto the glass surface using drops of 2 µL that were air dried to guarantee high binding efficiency. These highly fluorescent drops were then washed to remove excess sensor protein and observed using a 10x objective (**Fig. 30a**).

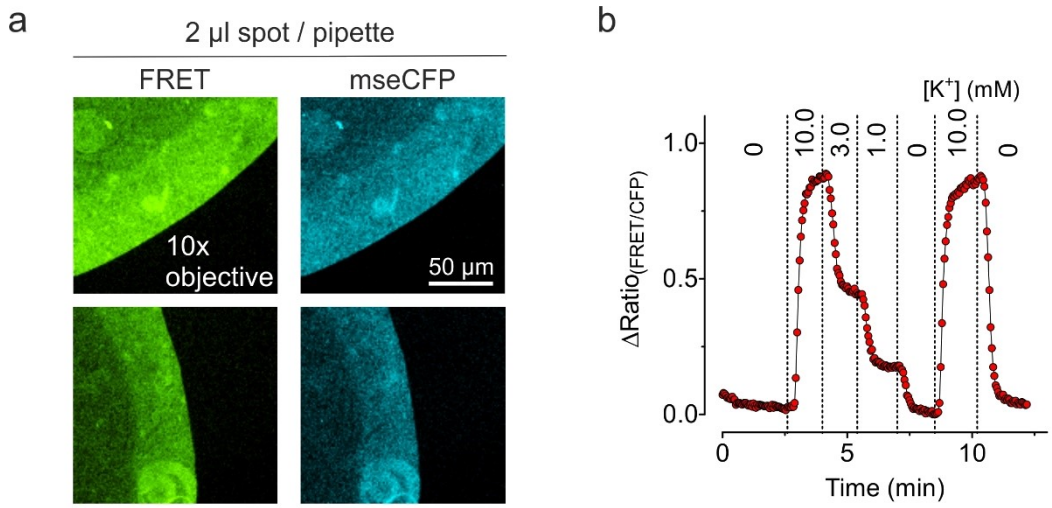

Figure 30: Measuring K^+ alterations in a defined area of immobilized protein. (a) Representative images of the mseCFP signal (left images) and the FRET emissions (right images) of a traptavidin-GEPII 1.0 spot on a biotinylated glass slide. A pipette was used to apply 2 µL of purified protein onto a selected area of the 30 mm circular biotinylated glass slide. The images were acquired using a 10x magnification on a fluorescence wide-field microscope.Scale bar indicates 50 µm. **(b)** Representative single cell response of an area as demonstrated in (**a**) upon alteration of K^+ levels using real-time wide-field FRET measurements. Buffers were exchanged using a gravity based perfusion system. n= 9.

In contrast to the background, the sharp edges of the applied spot were striking, with a brighter fluorescence at the border and a slightly decreasing fluorescence signal when coming towards the center of the spot. Due to the size of a 2 µL spot, although using a 10x magnification, it was not possible to image the whole area that was covered by the protein. Nevertheless, the sensor performed in response to various [K^+] with high precision, and a big dynamic range, as expected (**Fig. 30b**).

4.27 Traptavidin-GEPII 1.0 is functional after immobilization via microperfusion

Considering the generation of glass surfaces suitable for multi-parameter imaging, the methods of application still had to be improved, since it was not possible to image the whole area of the applied spot, although an already low magnification was used. In order to further improve our setup, we decided to use a novel, sophisticated device called BioPen, which represents a microperfusion system. This system enbles perfusion with a few microliters of fluid over a long time. The use of the BioPen in combination with a micromanipulator enabled the precise application within a distinct, selected area. This generated a demarcated perfusion "bubble", that comprised only a few µm in diameter, with a precision, that cannot be achieved using spot-application by hand. As a result of this bubble, an extremely small region was coupled with traptavidin-GEPII 1.0, that could even be observed as a whole using a 40x magnification (**Fig. 31a**).

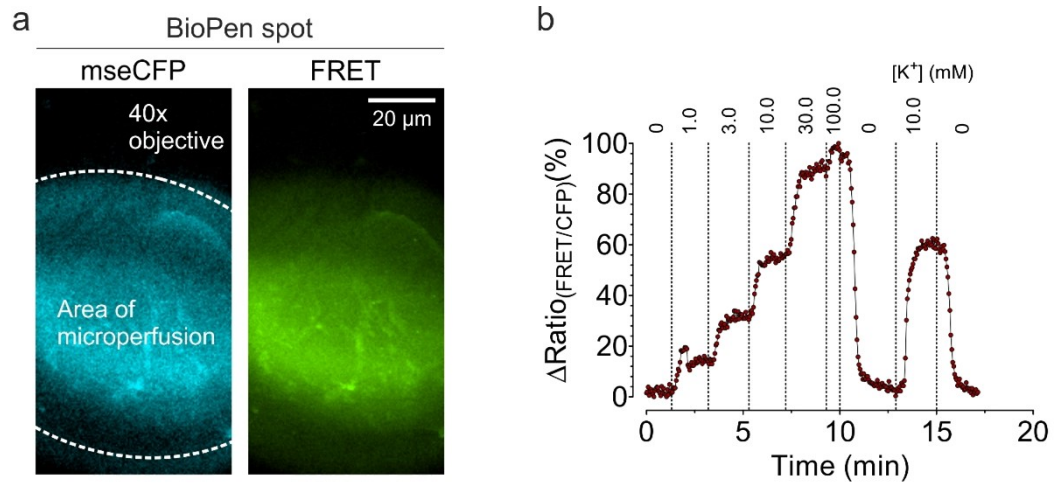

Figure 31: Generation of sensor patterns via a microperfusion enables K^+ meaurements within a small, defined region. (a) mseCFP (left image) and FRET fluorescence signals (right image) of traptavidin-GEPII 1.0 applied onto biotinylated glass using a microperfusion system. Images were acquired using a 40x magnification. Scale bar represents 20 µm. **(b)** Representative FRET ratio signal over time of the spot displayed in **(a)** upon perfusion with buffers possessing different [K^+] as indicated in the panel. n=3.

The fluorescence area did not display sharp edges, as observed previously putting a pipette drop onto the glas (**Fig. 30a**), but instead seemed to be blurred at the border with a higher fluorescence intensity in the center (**Fig. 31a**). Nevertheless, when measuring the response of the spot to different [K^+], we could observe that the sensor was functional and responded to increasing [K^+] in a concentration dependent manner (**Fig. 31b**). These experiments demonstrated, that our approach might be suitable to generate glass slides possessing many spots of different sensors in a small area, that can be observed at the same time for the simultaneous determination of parameters relevant for medical analysis or biotechnological use.

4.28 Coupling of selected cells using microperfusion

Another major advantage of the microperfusion system was its application *in situ*, to reduce protein volume and to facilitate the possibility to select a few single cells that should be coupled with the sensor. In future, this might lead to the possibility to use different sensors to adjecent cells for monitoring cell-to-cell communication and cell signalling. In analogy to the glass surface, the area of choice containing living cells was perfused using the BioPen. INS-1 cells were infected with a virus simultaneously encoding the GPI-anchored AviTag fused to mCherry and the ER targeted BirA, separated via an IRES, respectively. In analogy to the lipid based co-transfection, the viral infection yielded high expression levels as measured by the red fluorescence observed at the plasma membrane (**Fig. 32a**). Importantly, cells did not show any mseCFP or FRET fluorescence prior to the coupling (**Fig. 32a**). After 10 minutes of microperfusion, the same cells were imaged, showing a bright fluorescence signal of bound traptavidin-GEPII 1.0 at the cell border (**Fig. 32a**). Similar results were obtained using HeLa cells (**Fig. 32b**). During perfusion, the size and position of the perfusion bubble can easily be controlled, due to the highly fluorescent protein that is perfused (**Fig. 32b**). Within 10 minutes of perfusion, cells that were covered with the bubble displayed a strong fluorescent staining coming from traptavidin-GEPII 1.0. In contrast, cells at the bottom of the image which were located outside of the microperfusion area did not display a signal of traptavidin-GEPII 1.0, although infected with the virus (**Fig. 32b**). This met our expectation of a highly restricted perfusion zone, that facilitates single cell staining for yet challenging measurement approaches using different cell lines.

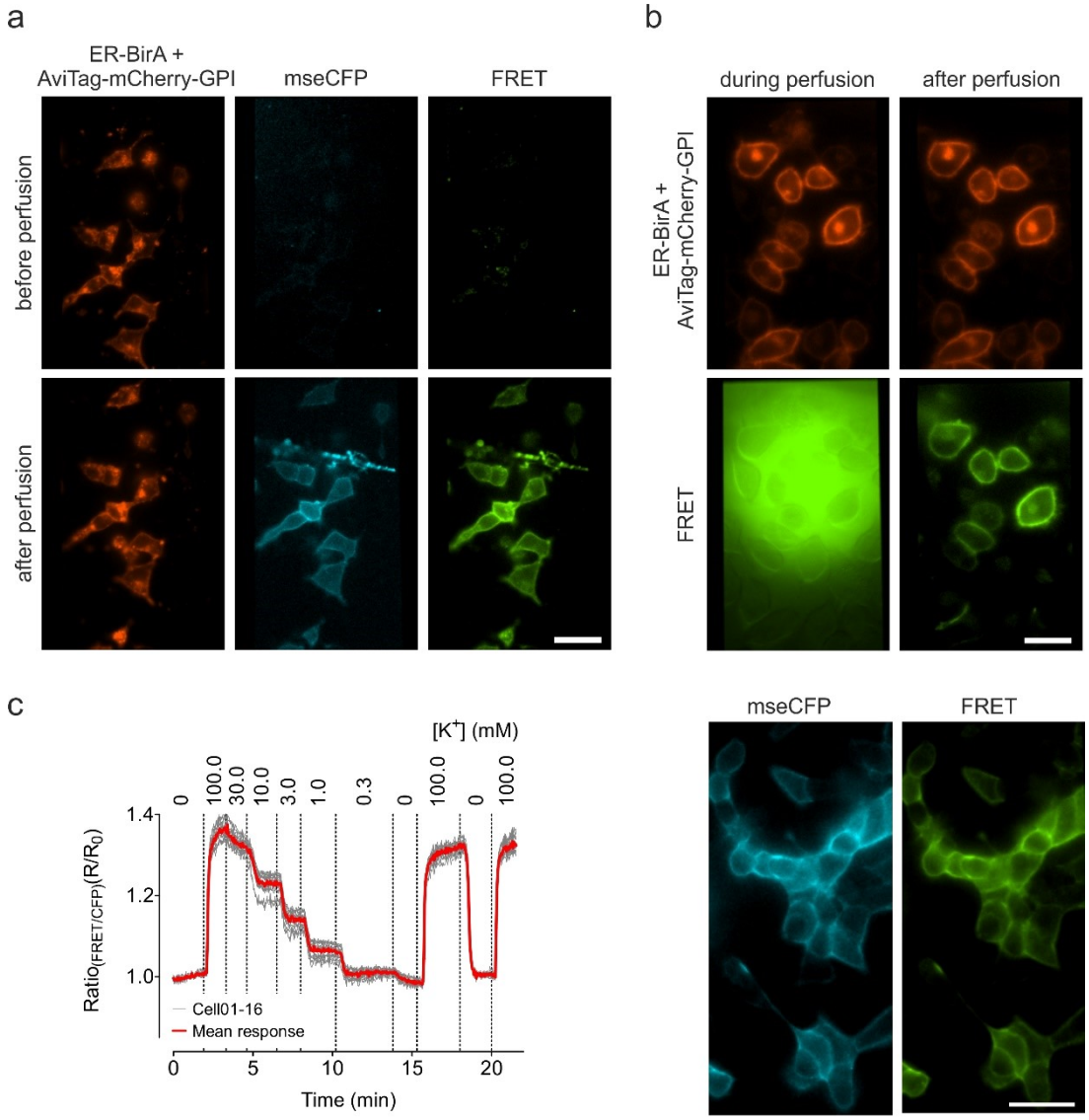

Figure 32: Living cells are highly accessible to be coupled with traptavidin-GEPII 1.0 using the microperfusion system. **(a)** Representative fluorescence emission images of INS-1 cells infected with the virus encoding for the ER-BirA and mCherry tagged AviTag (left images) before (upper row) and after (lower row) perfusion with traptavidin-GEPII 1.0. The mseCFP (middle row) and FRET signals (right row) were acquired before and after perfusion with traptavidin-GEPII 1.0. Scale bar indicates 20 µm. **(b)** Representative fluorescence emission images of HeLa cells infected with the virus during (left images) and after (right images) microperfusion with traptavidin-GEPII 1.0. The mCherry signal of AviTag-mCherry-GPI as well as the FRET fluorescence of traptavidin-GEPII 1.0 is shown. Scale bar indicates 20 µm. **(c)** Single cell responses of INS-1 cells upon titration of increasing levels of K^+ over a period of 22 minutes. Right panels display representative images of INS-1 cells with purified traptavidin-GEPII 1.0 bound on the cell surface. mseCFP (left image) and FRET (right image) fluorescence signals are demonstrated. Scale bar indicates 20 µm, n=3.

Importantly, the recombinant purified traptavidin-GEPII 1.0 was not only immobilized at the cell surfaces using the microperfusion system, but was also able to report extracellular K^+ alterations, with a similar accuracy and kinetics as determined using no microperfusion system (**Fig. 32c & Fig. 27b**). This indicates that the extraordinary strong interaction of biotin and traptavidin in combination with genetically-encoded purified sensors might be suitable for yet unknown applications in the field of fluorescence microscopy.

5 Discussion

Considering the metabolic imbalances that result in or are based on pH dyshomeostasis, the determination and tracking of pH values and alterations is of utmost importance (3,199,200). The development and progression of several neurodegenerative diseases that cause or are based on impairments in the autophagic- and/or secretory pathway are closely linked to a dysfunctional pH homeostasis (201–203). Also within the TME, acidification of the extracellular space leads to cellular metabolic imbalance and reprogramming (129,204). Although crucial, the determination of pH values within intracellular acidic vesicles and the extracellular space is challenging due to the hostile environments or the lack of targeting signals, suitable to specifically localize genetically-encoded probes (189).

To overcome the limitations of measuring pH levels within these compartments, we designed a novel pH probe referred to as pH-Lemon, which is suitable for the precise determination of pH alterations especially within the acidic pH range. pH-Lemon consists of two FPs with very different pH sensitivity (176). While mTurquoise2 is one of the most pH stable FPs available, possessing a pKa of 3.1, EYFP is extremely sensitive to pH alterations due to its pKa of around 6.5 (169–171). In our models, we confirmed these already published data concerning the pH sensitivity of the two FPs. Although mTurquoise2 is mildly affected by extremely acidic pH, the loss of fluorescence emission signal is negligible compared to EYFP (176).

We furthermore tested, whether the orientation of the two FPs has an effect on the dynamic range and functionality of our pH probes. The construct comprising an N-terminal EYFP and a C-terminal mTurquoise2 showed a slightly enhanced FRET efficiency. This might be due to a closer distance between the chromophores of two FPs if orientated this way. Hypothesizing that two mTurquoise2 might even further improve the FRET efficiency led to the generation of a triple FP-based construct with an EYFP flanked by one mTurquoise2 on each side, respectively. Unexpectedly, a dramatically reduced FRET signal could be detected, which might be caused by a misfolded EYFP due to the huge size of the fusion construct.

However, although the EYFP-mTurquoise2 sensor designed seemed to feature a slightly better dynamic range, we felt that the mTurquoise2-EYFP orientation might be better suitable to fit our aims of targeting the sensor to acidic vesicles using LC3B. The fusion protein to achieve autophagosomal targeting, LC3B, is cleaved at the C-terminal end, and, therefore, the sensor has to be located at the N-terminus of LC3B (179). Within the construct mTurquoise2-EYFP-LC3B, the pH sensitive FRET acceptor is flanked by two other proteins, which might, in theory, protect the EYFP, at least to some extend, from degradation. While degradation of the EYFP would lead to a misleading signal due to enhanced donor fluorescence, degradation of the mTurquoise2 would lead to a loss of both fluorescence signals in FRET measurements, excluding the possibility of result misinterpretation.

Using the mTurquoise2-EYFP fusion protein we proved, that the novel combination of the FPs resulted in a pH sensor suitable to measure a wide range of pH values from 4.0 to 8.0 with a pKa of 6.3 (176). Interestingly, the pKa of pH-Lemon expressed *in situ* was higher than *in vitro*, which might be due to the protein-rich environment when pH-Lemon is expressed in living cells (176). Considering the pKa *in situ*, the sensor is perfectly suitable to determine neutral to acidic pH values, but is inappropriate for the application if pH values higher than 7.5 are expected. Due to saturation of the senor in the alkaline pH range, distinct steady state pH values or pH alterations cannot be resolved by pH-Lemon, as differently targeted pH-Lemon variants could not discriminate between the alkaline pH levels of the mitochondrial matrix and the rather neutral cytosol. However, the probe acts as a precise pH reporter if targeted to acidic compartments, like autophagosomal or secretory vesicles, which is extremely important in terms of investigating impaired vesicular pH homeostasis in these organelles (176). While most genetically-encoded sensors rely on conformational rearrangements upon ion or analyte binding, yielding alterations in FRET efficiency, structural changes are not necessary for pH measurements (134,136). Many of the commonly used genetically-encoded pH probes rely on the principle of reversible (de-)protonation, which alters the fluorescence characteristics of the sensors (11,137,146). The presence of analyte binding domains, for example, within the GEPIIs or ATeams, might furthermore be responsible for the temperature sensitivity of these indicators, which altering their affinity for an analyte (134,136). This complicates the performance of different experiments using various cell lines or special experimental protocols that possibly require different temperatures. pH-Lemon, in contrast, features high temperature insensitivity over a wide temperature range, facilitating the measurement of special protocols like the effect of cold or heat stress on cell metabolic processes (176).

So far, there are several methods available for the determination of pH *in situ*. Noteworthy, ratiometric sensors are highly advantageous in terms of pH measurements, since intensiometric sensors strongly depend on their expression level (138). SypHer, ratiometric pHluorin and E^2GFP represent only some of the commonly used ratiometric single FP based probes, but their benefits lie mostly in the detection of neutral to alkaline pH levels (138,139,147). However, the palette of sensors suitable for acidic pH values seems limited. Under acidic conditions, Dendra2 turns from green to red caused by protonation of the phenolic group. The pKa of Dendra2 has been described to be at 7.2 and 7.5 (205). Another sensor that has already been applied for the visualization of endocytosis by measuring pH alterations represents the ratiometric E^1GFP, possessing a pKa of 6.0 (206). However, FRET-based sensors still represent the gold-standard for the precise quantification of ion concentrations and their alterations (207). A GFP-RFP FRET-pair fused to LC3B is already available to track pH fusion events during autophagy and is based on a similar working principle as pH-Lemon (142). Nevertheless, the use of this GFP-RFP construct bears some disadvantages, as the FRET donor is pH sensitive and quenched, leading to the loss of donor and acceptor emission signals (142).

Notably, another sensor using a CFP-YFP FRET-pair has been introduced in 2008, which is called pHlameleon (137). It consists of ECFP and EYFP to function as a FRET-based pH reporter. Although the design is similar to our developed pH sensor, there are still some major differences. A desirable feature of a pH sensor is the possibility to apply the sensor using FLIM. FLIM is a very useful technique to measure ion concentrations by determining the fluorescence lifetime of a fluorophore (181,208,209). If targeted into the lumen of acidic vesicles, the low pH values cause an increase in the fluorescence lifetime of mTurquiose2, while lifetimes become shorter under neutral to alkaline conditions. We successfully proved, that pH-Lemon can be applied using the FLIM technique for the precise quantification of subcellular pH values (176). In comparison to pHlameleons containing ECFP as the FRET donor with a reported lifetime of 3.0 ns, mTurquoise2 used in pH-Lemon has a longer fluorescence lifetime of 4.0 ns, making it more suitable for FLIM analysis and (169,210). In addition, pHlameleons were not targeted to intracellular vesicles, therefore, their suitability to function in intracellular acidic environments remains unknown (137). Besides using FLIM to observe intracellular vesicles, pH-Lemon can be measured using different fluorescence intensity imaging techniques, which extremely broadens the applicability of the probe. While one method comprises the classical FRET imaging technique with excitation of mTurquoise2 and detection of two emission signals, mTurqoiuse2 and FRET, simultaneously to determine their ratio, pH-Lemon can also be analyzed using separate excitation of the two FPs with detection of their emissions, respectively (176).

As the principle of FRET measurements requires a sophisticated set-up using beam-splitters and appropriate filter sets, the possibility to measure pH-Lemon using separate excitation expands the applicability a lot (211). Surprisingly, this technique incredibly increased the dynamic range, which facilitates tracking of very small pH changes (176). This confirms that the development of pH-Lemon closes a gap in the field of pH measurements.

To target the probe to the secretory pathway a GPI-anchor was used. The presence of the sensor on the plasma membrane functioned as an internal control and facilitated the calibration of the sensor without the need of cell- and vesicle-permeabilizing agents. On its way to the plasma membrane, pH-Lemon – GPI entered acidic vesicles that were easily detectable due to a high vesicular, but only weak ER staining. pH-Lemon – GPI revealed differently colored vesicles upon ratio-pseudocoloration, representing vesicles with different pH values (176). Interestingly, most clearly acidic, pH-Lemon containing vesicles showed a differently colored border (176). Due to the size of the vesicular membrane of only some nanometers, it is unlikely that this represents the membrane itself possessing a different pH. However, the surrounding of vesicles might be more acidic than the cytosol, due to an elevated [H^+] that is likely to be pumped into the lumen of the vesicle by the V-ATPases (98). Another possibility that might explain pH heterogeneity within vesicles is the formation of MVBs (212). These structures can be observed upon invagination of the vesicular membrane or fusion with EEs, which subsequently leads to the formation of ILVs. Most of these ILVs and their cargos are destined for degradation upon fusion of the MVB with a lysosome (212). Since MVBs are thought to fuse with vesicles that were previously formed from endocytosed plasma membrane, it is indeed possible that a portion of the GPI-anchored sensor is in the lumen of MVBs (75,212). Unexpectedly, pH-Lemon targeted vesicles seemed to possess a slightly bigger size compared to LC3B targeted vesicles. This might also point to the possible localization within MVBs, since their size has been reported to be larger in comparison to lysosomal vesicles (213–215). A localization of pH-Lemon – GPI within MVBs could, therefore, explain the slightly bigger size of some vesicular structure observed when expressing this construct (176). Notably, it is not possible to determine the proportional distribution of secretory- and endocytosed vesicles when using GPI-anchored pH-Lemon. Additional co-staining would be necessary to determine the amount of secreted vesicles, though, dyes like LysoTracker Red DND-99 are not applicable due to their accumulation within all acidic structures (192). Co-transfection with a FP tagged endosomal or lysosomal protein might result in specific staining, however, distinguishing between the different types of vesicles might be complex due to the high vesicle turnover, the recycling of membrane structures and the constant fusion of intracellular vesicles.

Compared to HeLa cells, the secretory pathway of HEK293 cells seemed to be strongly affected by the expression of pH-Lemon – GPI (176). The sensor abundance seemed to be strongly reduced at the plasma membrane, however, intracellular vesicles displayed an increased size as well as extremely acidic pH values and high abundance of the probe (176).

We hypothesized, that this effect might be caused by impaired secretion, leading to enlarged vesicles caused by accumulation of the sensor within these structures. Considering the low fluorescence signal at the cell border, these big sensor containing vesicles were not capable of fusing with the plasma membrane, but instead maybe fuse with MVBs for storage or degradation. INS-1 cells displayed, as expected, a similar distribution of vesicular structures as HeLa cells, although the number of acidic vesicles seemed to be elevated, with a region possessing an extremely high sensor density with moderate acidity, possibly representing the Golgi complex (176).

To exclude any artefacts of our vesicular pH measurements caused by sensor degradation, it was necessary to prove the functionality of the sensor located within the lumen of these vesicles. We used a mixture of NaN_3/NH_4Cl for neutralization, as this worked reliably in the past (191). After administration of these chemicals, the intravesicular pH was neutralized extremely fast, indicating that H^+ transported towards the vesicle membrane by V-ATPases or H^+ already present in the lumen of vesicles might be captured immediately (176). Due to the color transition from formerly red to green, i.e. neutralization, we could show that the sensor is still functional, and the reduced EYFP fluorescence in these structures is not caused by degradation of the FP, which would falsely also result in a high ratio and, hence, red vesicles (176). Interestingly, the effect of these substances could be reversed, as wash-out of the chemicals led to re-acidification of the vesicles, suggesting a high activity of the V-ATPases (176). It seems that cells try to restore vesicular pH levels under any circumstance, maybe even through enhancing V-ATPase activity, as the amount of highly acidic vesicles after wash-out seemed to be increased in some cells.

These experiments led us to the hypothesis that vesicular ion channel activity can easily be monitored using pH-Lemon, which was confirmed using Baf-A (108). The inhibition of the V-ATPases located in the vesicular membrane led to a similar phenomenon as previously observed using NaN_3/NH_4Cl, but, in this case, the H^+ pump activity was completely blocked (110). In contrast to the neutralizing chemicals, Baf-A pretreatment was necessary to guarantee inhibition of the H^+ pump, resulting in neutralization of many vesicles (176). As expected, wash-out of additionally applied NaN_3/NH_4Cl could restore the vesicular pH only to some extent (176). These experiments proved that Baf-A works as a potent H^+ pump inhibitor, however, NaN_3/NH_4Cl seemed to neutralize more efficiently than Baf-A in our model (176).

This might be due to different V-ATPase densities or activity on secretory vesicles compared to endosomes and lysosomes (60,101). In contrast to the functional principle of Baf-A, the neutralizing effect of NaN_3/NH_4Cl is independent of the amount of vesicular V-ATPases (108). Considering the high abundance of ion channels in the vesicular membrane, it might even be highly interesting to monitor vesicular pH as an indirect read-out for ion pump/channel activity (216). Possible alterations of vesicular pH levels caused by inhibition or activation of distinct ion channels and pumps could easily be observed and may yield a better understanding of the overall role of H^+ channels in these subcellular structures.

Considering the importance of controlled pH values within a cell, we aimed to use the GPI-targeted sensor in order to visualize pH_{ex} alterations. We hypothesized that pH_{ex} alterations might have severe consequences on cell metabolism by altering the intracellular pH levels. Strong pH changes, in particular pH decreases, can be found in the TME (128,129). Furthermore, areas of acute inflammation are known for their extremely acidic pH_{ex}, due to the metabolic activity and active immune cells fighting against the inflammation (217). The GPI construct, therefore, proved suitable to visualize changes of pH_{ex} values with the possibility to simultaneously monitor the effect on the intracellular pH, in particular, within vesicles (176). Interestingly, acidic pH_{ex} seemed to disrupt the vesicular pH completely, while alkaline pH affected only some of them. It seems like vesicles try to maintain their acidic pH, thereby fighting against neutralization in order to be capable of performing important degradation processes. Since most vesicles usually bear an acidic lumen, these compartments might be the only possibility for the cells to store and accumulate H^+ without the risk of severe damage caused by H^+ upon transport or diffusion to other organelles (218). However, the background signal coming from the ER and the vesicles upon expression of the GPI-targeted construct might complicate clean measurements of pH_{ex} alterations directly on the plasma membrane, especially if they are rather small (176).

To overcome the limitations of precise pH_{ex} measurements at the cell exterior, we re-designed a sophisticated approach to biotinylate the cell surface (160,163,164). This approach included the expression of BirA within the ER, as well as the AviTag that was supposed to travel through the ER, to the Golgi complex and, finally, via vesicles to the plasma membrane. So far, different proteins have been used to reach cell surface localization, however, a GPI-anchor has not been used to target the biotinylated AviTag to the membrane (163,164). Nevertheless, the time where both proteins, the enzyme and the AviTag, were located within the ER seemed sufficient for biotinylation of the AP. The rate of biotinylation might even be increased if a protein that resides within the ER for a longer time than a GPI-anchor was chosen. Although we hypothesized, that the big folded structure of mCherry near the AviTag might hamper its effective biotinylation, the addition of mCherry was necessary to select for cells expressing the constructs.

Since both transfected constructs, BirA as well as the AviTag, were tagged with mCherry, it was not possible to check for double transfection before coupling with the recombinant proteins, as both constructs displayed mild ER signal. Nevertheless, considering the aim of coupling CFP-YFP based FRET-sensors to the cell surface, the construct design containing mCherry was necessary to exclude spectral overlaps with CFP and YFP. However, positively transfected cells are likely to express both constructs upon co-transfection. Concerning the size of the FP, the biotinylation was successful, although the rate of biotinylation might be further increased if the FP was removed. While the first experiments were performed using a co-transfection of the AviTag and the BirA encoding plasmids, we wanted to further facilitate the method by generation of one Adenovirus encoding for both constructs separated by an IRES site. Considering the possibility of lower expression of the second ORFs when using an IRES, we decided that the first ORF should encode for the AviTag and the second for BirA. We hypothesized, that a lower expression of the BirA would be sufficient to biotinylated high amounts of the AviTag (219,220). This approach represented a big step in the adaptation of our novel method. While lipid based transfection is not suitable for primary cells or neurons, most cells can be infected using viruses encoding for the constructs.

The coupling of the recombinant sensor proteins was done by bathing the cells for approximately 30 minutes with the purified sensors. After incubation with the probe, the sensors were bound in high abundance to the cell surface, with solely staining of the plasma membrane. The biotinylation rate, i.e. mCherry signal coming from the GPI-AviTag, seemed to correlate with the sensor intensity after coupling. This led to the conclusion, that the supplemented biotin concentration was high enough and that the enzyme works very effectively within the ER. Considering the aim to detect extracellular acidification, pH-Lemon was the first purified sensor that was coupled to biotin on the cell surface. The approach yielded high plasma membrane staining, with the absence of intracellular vesicles. Although the sensors might have featured less flexibility upon immobilization in comparison to the freely diffusive probes in organelles, they still remained functional and precisely responded to extracellular pH and K^+ changes. Compared to pH-Lemon – GPI, purified traptavidin-pH-Lemon had a higher pKa of 7.0. Importantly, the biotin-traptavidin interaction was extremely strong. Although pH values in a range between 5.0 and 10.0 were perfused to calibrate the sensor, the strong bond of biotin and traptavidin was not affected, emphasizing a very low dissociation rate. While a huge sensor volume was used in order to incubate all cells growing on glass slides, the volume of protein solution was drastically reduced by the application of a microperfusion system.

Although the sensors were previously coupled in non-moving solution, perfusion with the BioPen, generating a constant buffer flow, did not impair sensor coupling efficiency. Contrary, a strong fluorescence signal could be found at the cell border after 10 minutes of coupling, highlighting the strong interaction between biotin and its counterpart. The coupling of only selected cells highlights the precision of this method, which might in future even allow the coupling of neighboring cells with different probes. Depending on the size of the perfused area, especially big cells like cardiomyocytes or neurons could be coupled partially with sensor protein. This would allow tracking of action potentials and cell signaling cascades.

In future, the coupling of traptavidin-pH-Lemon to the plasma membrane could further be used to visualize endocytotic events that might occur after some time allowing precise intracellular pH measurements within endosomal vesicles. This approach could, therefore, also serve as an identification method for the dynamics of the plasma membrane. Such approaches of using genetically-encoded sensors have already proven suitable to detect and follow endocytotic events (221). While the GPI-anchored pH-Lemon was localized within secretory vesicles and possibly also endosomes and lysosomes, a localization of the purified sensor in secretory vesicles can, at the early stage after endocytosis, be excluded. The fusion of endosomes with lysosomes can also be tracked, due to reduction of the EYFP signal upon increasing acidification. Upon co-staining with LysoTracker Red DND-99, the amount of EEs compared to the other vesicular populations possessing pH values close to neutral could easily be determined (192).

Besides pH-Lemon, our approach can also be used to couple other sensors of choice to the cell surface. This method represents a novelty in the field of using genetically-encoded sensors in an alternative way. So far, cells had to be transfected with different plasmids to eventually achieve plasma membrane located, genetically-encoded sensors measuring different analytes (222–224). However, the expression of different constructs might not be beneficial for the cell, and therefore, might irritate and influence cell homeostasis in different ways (225). Using our novel approach, only one plasmid, encoding for BirA and the AviTag, is needed which can either be transduced by transfection or viral infection.

The application of purified sensors without the need of *in situ*-expression of the sensor opens new doors for previously impossible applications. The CDH13 signal in combination with the GPI anchor turned out to be a useful targeting approach for pH-Lemon to measure a signal at the extracellular side of the plasma membrane. However, using other genetically-encoded sensors, like the recently developed GEPIIs, the same targeting sequence was unsuitable as the probe has lost its functionality (134). Despite the correct localization of the sensor at the cell border, the GPI-targeted GEPII 1.0 did not respond to K^+ alterations.

This might be due to glycosylation within the ER and Golgi complex that eventually prevents K^+ from binding or hampers the conformational change of the K^+ binding site. While it was not clear whether the immobilization via the non-covalent biotin-traptavidin binding might disturb K^+ binding or the structural change, the immobilized sensors turned out to remain fully functional. Furthermore, although present in a high density at the cell membrane, traptavidin-GEPII 1.0 could still adapt to the structural change upon K^+ binding, leading to increased FRET, thereby reporting changes in [K^+]. The use of purified traptavidin-GEPII 1.0 represents the first time to measure extracellular [K^+] and alterations directly at the cell surface. In terms of K^+ alterations in the TME caused by increased cell death and, as a result, elevated [K^+], this method might lead to novel insights into tumor development and cell death in the necrotic core of a tumor (197). Especially in excitable cells such as cardiac myocytes and neurons, K^+ alterations across the plasma membrane are essential for these cells to fulfill their function (226,227). But not only K^+ alterations are of utmost importance in neuronal metabolism, also cell signaling pathways like neuronal vesicle release or Ca^{2+} signals could possibly be observed in the future (228,229).

The application of purified sensors might also be used in combination with antibodies. Biotinylated antibodies are already available and could be targeted to a plasma membrane protein of choice for further coupling with a traptavidin-fused sensor (230). To further minimize the size of the biotinylated protein, instead of antibodies, nanobodies that are targeted against a membrane protein could be used (231). Upon biotinylation of a nanobody targeted against a special membrane component, different purified sensors could be bound to the biotin residue. This method would circumvent the need of transfection/infection and overexpression.

Purified sensors cannot only be bound to the cell surface for applications *in situ*, but can also be linked to surfaces of non-biological origin. The coupling of sensor proteins to glass slides possessing a biotinylated surface represents a major improvement in terms of biotechnology. While the biotin density seemed to be considerably lower at the glass compared to the cell surface, the density of sensor protein was still sufficient to detect sensor fluorescence, suitable for the quantification of analyte concentrations. As described by the company (Microsurfaces, Inc.), the biotin is thought to be linked to the glass via a PEG layer that provides hydrophilic groups for immobilization. Similar to the application *in situ*, the sensor possessed a high stability, even under extreme pH conditions or at high [K^+]. Furthermore, the sensor coupled glass slides did not seem to be affected by a gravity-based perfusion system generating a laminar flow across the surface. Incubation of the glass slide with 0.5 mL of protein solution covered the whole slide and led to a homogenous fluorescence signal. Since the use of a huge amount of solution is not feasible, we tested different methods to systematically reduce the sensor volume. Already the application of 2 µL of recombinant purified protein proved suitable to precisely measure and quantify K^+ alterations.

The fluorescence emissions were considerably higher at a roundish region at the border compared to the center of the spot. This might be due to surface tension that is higher at a 2 µL spot. This tension could have led to an accumulation of the sensor at the contact sides between the solution and the glass surface, creating a brighter border. Nonetheless, the sensor reacted ratiometrically and precisely, independent of a localization on the border or within the center of the spot. Due to the size, only parts of the spots could be observed using a 10x magnification.

Therefore, we further reduced the sensor volume using the microperfusion system. Interestingly, perfusion of the glass using the device created small spots that could easily be observed using a 40x magnification. This techniques might in future be used to generate surfaces for multi-parameter imaging. The use of different sensors for the determination of parameters relevant for medical treatment, for example, pH, glucose, K^+, Mg^{2+} and Ca^{2+}, would pave the way for screening of biological fluids within very short periods of time. Patients would immediately know, whether they should e.g. attend dialysis or consult a medical doctor to check for their health condition or get medical treatment. This might lead to the generation of novel devices, similar to the highly sophisticated insulin devices that drastically increase the life quality of diabetic patients. Considering biotechnological applications, using such sensor spots within a tube connected to the fluid source would serve as a real-time read out for the fast determination of various parameters. Especially within bioreactors, in sewage plants or in the food production/processing, important components of fluids have to be checked constantly to ensure high quality (232–234). Using this technique, taking specimen by hand will become redundant.

Considering the aspects of metabolic imbalances of cells, the determination of ion or metabolite concentrations is essential for a better understanding of processes regulating health and disease. The application of pH-Lemon might help to determine critical events in pH homeostasis in terms of vesicle metabolism in autophagy, secretion and endocytosis that could, eventually, help to generate new therapeutical strategies. Furthermore, the previously unknown application of purified genetically-encoded sensors, immobilized exploiting the affinity of biotin-traptavidin, could represent a hallmark for novel screening strategies, allowing precise real-time determinations of relevant parameters.

6 References

1. Ruffin VA, Salameh AI, Boron WF, Parker MD. Intracellular pH regulation by acid-base transporters in mammalian neurons. Front Physiol. 2014; 5. http://journal.frontiersin.org/article/10.3389/fphys.2014.00043/abstract

2. Boron WF. Regulation of intracellular pH. Adv Physiol Educ. Dezember 2004;28(1–4):160–79.

3. Aoi W, Marunaka Y. Importance of pH Homeostasis in Metabolic Health and Diseases: Crucial Role of Membrane Proton Transport. BioMed Res Int. 2014;2014:1–8.

4. Hamilton G, Mathur R, Allsop JM, Forton DM, Dhanjal NS, Shaw RJ, u. a. Changes in brain intracellular pH and membrane phospholipids on oxygen therapy in hypoxic patients with chronic obstructive pulmonary disease. Metab Brain Dis. März 2003;18(1):95–109.

5. Vingtdeux V, Hamdane M, Bégard S, Loyens A, Delacourte A, Beauvillain J-C, u. a. Intracellular pH regulates amyloid precursor protein intracellular domain accumulation. Neurobiol Dis. März 2007;25(3):686–96.

6. Cole NB, DiEuliis D, Leo P, Mitchell DC, Nussbaum RL. Mitochondrial translocation of α-synuclein is promoted by intracellular acidification. Exp Cell Res. Juni 2008;314(10):2076–89.

7. Lyros E, Ragoschke-Schumm A, Kostopoulos P, Sehr A, Backens M, Kalampokini S, u. a. Normal brain aging and Alzheimer's disease are associated with lower cerebral pH: an in vivo histidine 1H-MR spectroscopy study. Neurobiol Aging. November 2019;S0197458019304117.

8. Ibarreta D, Urcelay E, Parrilla R, Ayuso MS. Distinct pH homeostatic features in lymphoblasts from Alzheimer's disease patients. Ann Neurol. August 1998;44(2):216–22.

9. Madshus IH. Regulation of intracellular pH in eukaryotic cells. Biochem J. 15. Februar 1988;250(1):1–8.

10. Dechant R, Peter M. Cytosolic pH: A conserved regulator of cell growth? Mol Cell Oncol. 8. Dezember 2014;1(4):e969643.

11. Poburko D, Santo-Domingo J, Demaurex N. Dynamic Regulation of the Mitochondrial Proton Gradient during Cytosolic Calcium Elevations. J Biol Chem. 1. April 2011;286(13):11672–84.

12. Hu J, Dong L, Outten CE. The Redox Environment in the Mitochondrial Intermembrane Space Is Maintained Separately from the Cytosol and Matrix. J Biol Chem. 24. Oktober 2008;283(43):29126–34.

13. Dempsey JL, Winkler JR, Gray HB. Proton-Coupled Electron Flow in Protein Redox Machines. Chem Rev. 8. Dezember 2010;110(12):7024–39.

14. Santo-Domingo J, Demaurex N. The renaissance of mitochondrial pH. J Gen Physiol. 1. Juni 2012;139(6):415–23.

15. Llopis J, McCaffery JM, Miyawaki A, Farquhar MG, Tsien RY. Measurement of cytosolic, mitochondrial, and Golgi pH in single living cells with green fluorescent proteins. Proc Natl Acad Sci. 9. Juni 1998;95(12):6803–8.

16. Mitchell P. Coupling of Phosphorylation to Electron and Hydrogen Transfer by a Chemi-Osmotic type of Mechanism. Nature. Juli 1961;191(4784):144–8.

17. Mitchell P. Proton translocation mechanisms and energy transduction by adenosine triphosphatases: An answer to criticisms. FEBS Lett. 1. Februar 1975;50(2):95–7.

18. Mitchell P, Moyle J. Estimation of Membrane Potential and pH Difference across the Cristae Membrane of Rat Liver Mitochondria. Eur J Biochem. 3. März 2005;7(4):471–84.

19. Baughman JM, Perocchi F, Girgis HS, Plovanich M, Belcher-Timme CA, Sancak Y, u. a. Integrative genomics identifies MCU as an essential component of the mitochondrial calcium uniporter. Nature. August 2011;476(7360):341–5.

20. De Stefani D, Raffaello A, Teardo E, Szabò I, Rizzuto R. A forty-kilodalton protein of the inner membrane is the mitochondrial calcium uniporter. Nature. August 2011;476(7360):336–40.

21. Vergun O, Votyakova TV, Reynolds IJ. Spontaneous Changes in Mitochondrial Membrane Potential in Single Isolated Brain Mitochondria. Biophys J. November 2003;85(5):3358–66.

22. Kraemer R, Klingenberg M. Modulation of the reconstituted adenine nucleotide exchange by membrane potential. Biochemistry. 5. Februar 1980;19(3):556–60.

23. Jiang D, Zhao L, Clapham DE. Genome-Wide RNAi Screen Identifies Letm1 as a Mitochondrial Ca2+/H+ Antiporter. Science. 2. Oktober 2009;326(5949):144–7.

24. Nowikovsky K, Froschauer EM, Zsurka G, Samaj J, Reipert S, Kolisek M, u. a. The *LETM1* / *YOL027* Gene Family Encodes a Factor of the Mitochondrial K^+ Homeostasis with a Potential Role in the Wolf-Hirschhorn Syndrome. J Biol Chem. 16. Juli 2004;279(29):30307–15.

25. Nicholls DG. The regulation of extramitochondrial free calcium ion concentration by rat liver mitochondria. Biochem J. 15. November 1978;176(2):463–74.

26. Haworth RA, Hunter DR. The Ca2+-induced membrane transition in mitochondria. Arch Biochem Biophys. Juli 1979;195(2):460–7.

27. Roos A, Boron WF. Intracellular pH. Physiol Rev. April 1981;61(2):296–434.

28. Wu M, Neilson A, Swift AL, Moran R, Tamagnine J, Parslow D, u. a. Multiparameter metabolic analysis reveals a close link between attenuated mitochondrial bioenergetic function and enhanced glycolysis dependency in human tumor cells. Am J Physiol-Cell Physiol. Januar 2007;292(1):C125–36.

29. Mookerjee SA, Goncalves RLS, Gerencser AA, Nicholls DG, Brand MD. The contributions of respiration and glycolysis to extracellular acid production. Biochim Biophys Acta BBA - Bioenerg. Februar 2015;1847(2):171–81.

30. Robergs RA, Ghiasvand F, Parker D. Biochemistry of exercise-induced metabolic acidosis. Am J Physiol-Regul Integr Comp Physiol. September 2004;287(3):R502–16.

31. Hoffman JF, Hillier J, Wolman IJ, Parpart AK. New high density particles in certain normal and abnormal erythrocytes. J Cell Comp Physiol. April 1956;47(2):245–59.

32. Tamai I, Yabuuchi H, Nezu J, Sai Y, Oku A, Shimane M, u. a. Cloning and characterization of a novel human pH-dependent organic cation transporter, OCTN1. FEBS Lett. 8. Dezember 1997;419(1):107–11.

33. Eriksen J, Chang R, McGregor M, Silm K, Suzuki T, Edwards RH. Protons Regulate Vesicular Glutamate Transporters through an Allosteric Mechanism. Neuron. Mai 2016;90(4):768–80.

34. Coulter KL, Pe´rier F, Redeke CM, Vanderberg CA. Identification and molecular localization of a pH-sensing domain for the inward rectifier potassium channel HIR. Neuron. November 1995;15(5):1157–68.

35. Missner A, Kügler P, Saparov SM, Sommer K, Mathai JC, Zeidel ML, u. a. Carbon Dioxide Transport through Membranes. J Biol Chem. 12. September 2008;283(37):25340–7.

36. Reinertsen KV, Tønnessen TI, Jacobsen J, Sandvig K, Olsnes S. Role of chloride/bicarbonate antiport in the control of cytosolic pH. Cell-line differences in activity and regulation of antiport. J Biol Chem. 15. August 1988;263(23):11117–25.

37. Stewart AK, Boyd CAR, Vaughan-Jones RD. A novel role for carbonic anhydrase: cytoplasmic pH gradient dissipation in mouse small intestinal enterocytes. J Physiol. April 1999;516(1):209–17.

38. Halestrap AP. The monocarboxylate transporter family-Structure and functional characterization. IUBMB Life. Januar 2012;64(1):1–9.

39. Roth DA, Brooks GA. Lactate transport is mediated by a membrane-bound carrier in rat skeletal muscle sarcolemmal vesicles. Arch Biochem Biophys. Juni 1990;279(2):377–85.

40. Juel C. Lactate/proton co-transport in skeletal muscle: regulation and importance for pH homeostasis. Acta Physiol Scand. März 1996;156(3):369–74.

41. Brett CL, Donowitz M, Rao R. Evolutionary origins of eukaryotic sodium/proton exchangers. Am J Physiol-Cell Physiol. Februar 2005;288(2):C223–39.

42. Orlowski J, Grinstein S. Emerging roles of alkali cation/proton exchangers in organellar homeostasis. Curr Opin Cell Biol. August 2007;19(4):483–92.

43. Sanhueza C, Araos J, Naranjo L, Toledo F, Beltrán AR, Ramírez MA, u. a. Sodium/proton exchanger isoform 1 regulates intracellular pH and cell proliferation in human ovarian cancer. Biochim Biophys Acta BBA - Mol Basis Dis. Januar 2017;1863(1):81–91.

44. Aharonovitz O, Zaun HC, Balla T, York JD, Orlowski J, Grinstein S. Intracellular Ph Regulation by Na+/H+ Exchange Requires Phosphatidylinositol 4,5-Bisphosphate. J Cell Biol. 10. Juli 2000;150(1):213–24.

45. Amith SR, Fliegel L. Regulation of the Na+/H+ Exchanger (NHE1) in Breast Cancer Metastasis. Cancer Res. 15. Februar 2013;73(4):1259–64.

46. Saleh AM, Batlle DC. Kinetic properties of the Na+/H+ antiporter of lymphocytes from the spontaneously hypertensive rat: role of intracellular pH. J Clin Invest. 1. Juni 1990;85(6):1734–9.

47. Wakabayashi S, Shigekawa M, Pouyssegur J. Molecular physiology of vertebrate Na+/H+ exchangers. Physiol Rev. 1. Januar 1997;77(1):51–74.

48. Merezhinskaya N, Fishbein WN, Davis JI, Foellmer JW. Mutations in MCT1 cDNA in patients with symptomatic deficiency in lactate transport. Muscle Nerve. Januar 2000;23(1):90–7.

49. Halestrap AP, Wilson MC. The monocarboxylate transporter family-Role and regulation. IUBMB Life. Februar 2012;64(2):109–19.

50. Humphreys BD, Jiang L, Chernova MN, Alper SL. Functional characterization and regulation by pH of murine AE2 anion exchanger expressed in Xenopus oocytes. Am J Physiol-Cell Physiol. 1. November 1994;267(5):C1295–307.

51. Hulikova A, Swietach P. Nuclear proton dynamics and interactions with calcium signaling. J Mol Cell Cardiol. Juli 2016;96:26–37.

52. Casey JR, Grinstein S, Orlowski J. Sensors and regulators of intracellular pH. Nat Rev Mol Cell Biol. Januar 2010;11(1):50–61.

53. Masuda A, Oyamada M, Nagaoka T, Tateishi N, Takamatsu T. Regulation of cytosol–nucleus pH gradients by K+/H+ exchange mechanism in the nuclear envelope of neonatal rat astrocytes. Brain Res. Oktober 1998;807(1–2):70–7.

54. Wu MM, Llopis J, Adams S, McCaffery JM, Kulomaa MS, Machen TE, u. a. Organelle pH studies using targeted avidin and fluorescein–biotin. Chem Biol. März 2000;7(3):197–209.

55. Kim JH, Johannes L, Goud B, Antony C, Lingwood CA, Daneman R, u. a. Noninvasive measurement of the pH of the endoplasmic reticulum at rest and during calcium release. Proc Natl Acad Sci. 17. März 1998;95(6):2997–3002.

56. Glickman J, Croen K, Kelly S, Al-Awqati Q. Golgi membranes contain an electrogenic H+ pump in parallel to a chloride conductance. J Cell Biol. 1. Oktober 1983;97(4):1303–8.

57. Kim JH, Lingwood CA, Williams DB, Furuya W, Manolson MF, Grinstein S. Dynamic measurement of the pH of the Golgi complex in living cells using retrograde transport of the verotoxin receptor. J Cell Biol. 15. September 1996;134(6):1387–99.

58. Demaurex N, Furuya W, D'Souza S, Bonifacino JS, Grinstein S. Mechanism of Acidification of the *trans* -Golgi Network (TGN): *IN SITU* MEASUREMENTS OF pH USING

RETRIEVAL OF TGN38 AND FURIN FROM THE CELL SURFACE. J Biol Chem. 23. Januar 1998;273(4):2044–51.

59. Schapiro FB, Grinstein S. Determinants of the pH of the Golgi Complex. J Biol Chem. 14. Juli 2000;275(28):21025–32.

60. Wu MM, Grabe M, Adams S, Tsien RY, Moore H-PH, Machen TE. Mechanisms of pH Regulation in the Regulated Secretory Pathway. J Biol Chem. 31. August 2001;276(35):33027–35.

61. Paroutis P, Touret N, Grinstein S. The pH of the Secretory Pathway: Measurement, Determinants, and Regulation. Physiology. August 2004;19(4):207–15.

62. Kellokumpu S, Sormunen R, Kellokumpu I. Abnormal glycosylation and altered Golgi structure in colorectal cancer: dependence on intra-Golgi pH. FEBS Lett. 10. April 2002;516(1–3):217–24.

63. Huang C, Chang A. pH-dependent Cargo Sorting from the Golgi. J Biol Chem. 25. März 2011;286(12):10058–65.

64. DiCiccio JE, Steinberg BE. Lysosomal pH and analysis of the counter ion pathways that support acidification. J Gen Physiol. 1. April 2011;137(4):385–90.

65. Hu Y-B, Dammer EB, Ren R-J, Wang G. The endosomal-lysosomal system: from acidification and cargo sorting to neurodegeneration. Transl Neurodegener. Dezember 2015;4(1):18.

66. Bonifacino JS, Glick BS. The Mechanisms of Vesicle Budding and Fusion. Cell. Januar 2004;116(2):153–66.

67. Mancias JD, Goldberg J. Exiting the Endoplasmic Reticulum: Exiting the Endoplasmic Reticulum. Traffic. April 2005;6(4):278–85.

68. Bruckner JJ, Zhan H, Gratz SJ, Rao M, Ukken F, Zilberg G, u. a. Fife organizes synaptic vesicles and calcium channels for high-probability neurotransmitter release. J Cell Biol. 2. Januar 2017;216(1):231–46.

69. Mani M. Live imaging of synaptic vesicle release and retrieval in dopaminergic neurons. Front Neural Circuits [Internet]. 2009 [zitiert 27. Januar 2020];3. Verfügbar unter: http://journal.frontiersin.org/article/10.3389/neuro.04.003.2009/abstract

70. Seksek O, Biwersi J, Verkman AS. Direct Measurement of *trans* -Golgi pH in Living Cells and Regulation by Second Messengers. J Biol Chem. 10. März 1995;270(10):4967–70.

71. Saw NMN, Kang S-YA, Parsaud L, Han GA, Jiang T, Grzegorczyk K, u. a. Vacuolar H $^{+}$ -ATPase subunits Voa1 and Voa2 cooperatively regulate secretory vesicle acidification, transmitter uptake, and storage. Malhotra V, Herausgeber. Mol Biol Cell. 15. September 2011;22(18):3394–409.

72. Stauber T, Jentsch TJ. Chloride in Vesicular Trafficking and Function. Annu Rev Physiol. 10. Februar 2013;75(1):453–77.

73. Sankaranarayanan S, Ryan TA. Real-time measurements of vesicle-SNARE recycling in synapses of the central nervous system. Nat Cell Biol. April 2000;2(4):197–204.

74. Zerial M, McBride H. Rab proteins as membrane organizers. Nat Rev Mol Cell Biol. Februar 2001;2(2):107–17.

75. Lakadamyali M, Rust MJ, Zhuang X. Ligands for Clathrin-Mediated Endocytosis Are Differentially Sorted into Distinct Populations of Early Endosomes. Cell. März 2006;124(5):997–1009.

76. Grimes ML, Zhou J, Beattie EC, Yuen EC, Hall DE, Valletta JS, u. a. Endocytosis of Activated TrkA: Evidence that Nerve Growth Factor Induces Formation of Signaling Endosomes. J Neurosci. 15. Dezember 1996;16(24):7950–64.

77. Barbieri MA, Roberts RL, Gumusboga A, Highfield H, Alvarez-Dominguez C, Wells A, u. a. Epidermal Growth Factor and Membrane Trafficking. J Cell Biol. 30. Oktober 2000;151(3):539–50.

78. Nielsen E, Severin F, Backer JM, Hyman AA, Zerial M. Rab5 regulates motility of early endosomes on microtubules. Nat Cell Biol. Oktober 1999;1(6):376–82.

79. Maxfield FR, McGraw TE. Endocytic recycling. Nat Rev Mol Cell Biol. Februar 2004;5(2):121–32.

80. Murphy RF, Powers S, Cantor CR. Endosome pH measured in single cells by dual fluorescence flow cytometry: rapid acidification of insulin to pH 6. J Cell Biol. 1. Mai 1984;98(5):1757–62.

81. Poteryaev D, Datta S, Ackema K, Zerial M, Spang A. Identification of the Switch in Early-to-Late Endosome Transition. Cell. April 2010;141(3):497–508.

82. Ishida Y, Nayak S, Mindell JA, Grabe M. A model of lysosomal pH regulation. J Gen Physiol. 1. Juni 2013;141(6):705–20.

83. Reggiori F, Pelham HRB. Sorting of proteins into multivesicular bodies: ubiquitin-dependent and -independent targeting. EMBO J. 17. September 2001;20(18):5176–86.

84. Bissig C, Gruenberg J. Lipid Sorting and Multivesicular Endosome Biogenesis. Cold Spring Harb Perspect Biol. 1. Oktober 2013;5(10):a016816–a016816.

85. Bright NA, Reaves BJ, Mullock BM, Luzio JP. Dense core lysosomes can fuse with late endosomes and are re-formed from the resultant hybrid organelles. J Cell Sci. September 1997;110 (Pt 17):2027–40.

86. Pillay CS, Elliott E, Dennison C. Endolysosomal proteolysis and its regulation. Biochem J. 1. Mai 2002;363(3):417.

87. Glick D, Barth S, Macleod KF. Autophagy: cellular and molecular mechanisms. J Pathol. Mai 2010;221(1):3–12.

88. Lee JM, Wagner M, Xiao R, Kim KH, Feng D, Lazar MA, u. a. Nutrient-sensing nuclear receptors coordinate autophagy. Nature. Dezember 2014;516(7529):112–5.

89. Moruno F, Pérez-Jiménez E, Knecht E. Regulation of Autophagy by Glucose in Mammalian Cells. Cells. 27. Juli 2012;1(3):372–95.

90. Depaoli MR, Karsten F, Madreiter-Sokolowski CT, Klec C, Gottschalk B, Bischof H, u. a. Real-Time Imaging of Mitochondrial ATP Dynamics Reveals the Metabolic Setting of Single Cells. Cell Rep. Oktober 2018;25(2):501-512.e3.

91. Rabinowitz JD, White E. Autophagy and Metabolism. Science. 3. Dezember 2010;330(6009):1344–8.

92. Jung CH, Ro S-H, Cao J, Otto NM, Kim D-H. mTOR regulation of autophagy. FEBS Lett. 2. April 2010;584(7):1287–95.

93. Korkmaz G, le Sage C, Tekirdag KA, Agami R, Gozuacik D. miR-376b controls starvation and mTOR inhibition-related autophagy by targeting ATG4C and BECN1. Autophagy. Februar 2012;8(2):165–76.

94. Fujita N, Itoh T, Omori H, Fukuda M, Noda T, Yoshimori T. The Atg16L Complex Specifies the Site of LC3 Lipidation for Membrane Biogenesis in Autophagy. Riezman H, Herausgeber. Mol Biol Cell. Mai 2008;19(5):2092–100.

95. Wesselborg S, Stork B. Autophagy signal transduction by ATG proteins: from hierarchies to networks. Cell Mol Life Sci. Dezember 2015;72(24):4721–57.

96. Kopitz J, Kisen GO, Gordon PB, Bohley P, Seglen PO. Nonselective autophagy of cytosolic enzymes by isolated rat hepatocytes. J Cell Biol. 1. September 1990;111(3):941–53.

97. Zaffagnini G, Martens S. Mechanisms of Selective Autophagy. J Mol Biol. Mai 2016;428(9):1714–24.

98. Jefferies KC, Cipriano DJ, Forgac M. Function, structure and regulation of the vacuolar (H+)-ATPases. Arch Biochem Biophys. August 2008;476(1):33–42.

99. Marshansky V, Futai M. The V-type H+-ATPase in vesicular trafficking: targeting, regulation and function. Curr Opin Cell Biol. August 2008;20(4):415–26.

100. Toei M, Saum R, Forgac M. Regulation and Isoform Function of the V-ATPases. Biochemistry. 15. Juni 2010;49(23):4715–23.

101. Kane PM. The long physiological reach of the yeast vacuolar H+-ATPase. J Bioenerg Biomembr. Dezember 2007;39(5–6):415–21.

102. Lu M, Ammar D, Ives H, Albrecht F, Gluck SL. Physical Interaction between Aldolase and Vacuolar H $^{+}$ -ATPase Is Essential for the Assembly and Activity of the Proton Pump. J Biol Chem. 24. August 2007;282(34):24495–503.

103. Smardon AM, Tarsio M, Kane PM. The RAVE Complex Is Essential for Stable Assembly of the Yeast V-ATPase. J Biol Chem. 19. April 2002;277(16):13831–9.

104. Seidel T, Scholl S, Krebs M, Rienmüller F, Marten I, Hedrich R, u. a. Regulation of the V-type ATPase by redox modulation. Biochem J. 1. Dezember 2012;448(2):243–51.

105. Huss M, Wieczorek H. Inhibitors of V-ATPases: old and new players. J Exp Biol. 1. Februar 2009;212(3):341–6.

106. Mauvezin C, Neufeld TP. Bafilomycin A1 disrupts autophagic flux by inhibiting both V-ATPase-dependent acidification and Ca-P60A/SERCA-dependent autophagosome-lysosome fusion. Autophagy. 3. August 2015;11(8):1437–8.

107. Bowman EJ, Siebers A, Altendorf K. Bafilomycins: a class of inhibitors of membrane ATPases from microorganisms, animal cells, and plant cells. Proc Natl Acad Sci. 1. November 1988;85(21):7972–6.

108. Yoshimori T, Yamamoto A, Moriyama Y, Futai M, Tashiro Y. Bafilomycin A1, a specific inhibitor of vacuolar-type H(+)-ATPase, inhibits acidification and protein degradation in lysosomes of cultured cells. J Biol Chem. 15. September 1991;266(26):17707–12.

109. Hanada H, Moriyama Y, Maeda M, Futai M. Kinetic studies of chromaffin granule H+-ATPase and effects of bafilomycin A1. Biochem Biophys Res Commun. Juli 1990;170(2):873–8.

110. Crider BP, Xie XS, Stone DK. Bafilomycin inhibits proton flow through the H+ channel of vacuolar proton pumps. J Biol Chem. 1. Juli 1994;269(26):17379–81.

111. Zhang J, Feng Y, Forgac M. Proton conduction and bafilomycin binding by the V0 domain of the coated vesicle V-ATPase. J Biol Chem. 23. September 1994;269(38):23518–23.

112. Vergo S, Craner MJ, Etzensperger R, Attfield K, Friese MA, Newcombe J, u. a. Acid-sensing ion channel 1 is involved in both axonal injury and demyelination in multiple sclerosis and its animal model. Brain. Februar 2011;134(2):571–84.

113. Mattson MP, Pedersen WA, Duan W, Culmsee C, Camandola S. Cellular and Molecular Mechanisms Underlying Perturbed Energy Metabolism and Neuronal Degeneration in Alzheimer's and Parkinson's Diseases. Ann N Y Acad Sci. November 1999;893(1 OXIDATIVE/ENE):154–75.

114. Song E-S, Juliano MA, Juliano L, Hersh LB. Substrate Activation of Insulin-degrading Enzyme (Insulysin): A POTENTIAL TARGET FOR DRUG DEVELOPMENT. J Biol Chem. 12. Dezember 2003;278(50):49789–94.

115. Balestrino M, Somjen GG. Concentration of carbon dioxide, interstitial pH and synaptic transmission in hippocampal formation of the rat. J Physiol. 1. Februar 1988;396(1):247–66.

116. Tombaugh GC, Sapolsky RM. Mild acidosis protects hippocampal neurons from injury induced by oxygen and glucose deprivation. Brain Res. Januar 1990;506(2):343–5.

117. Shen Z, Zheng Y, Wu J, Chen Y, Wu X, Zhou Y, u. a. PARK2-dependent mitophagy induced by acidic postconditioning protects against focal cerebral ischemia and extends the reperfusion window. Autophagy. 4. März 2017;13(3):473–85.

118. Demetrius LA, Simon DK. An inverse-Warburg effect and the origin of Alzheimer's disease. Biogerontology. Dezember 2012;13(6):583–94.

119. Baranello RJ, Bharani KL, Padmaraju V, Chopra N, Lahiri DK, Greig NH, u. a. Amyloid-beta protein clearance and degradation (ABCD) pathways and their role in Alzheimer's disease. Curr Alzheimer Res. 2015;12(1):32–46.

120. Prasad H, Rao R. Amyloid clearance defect in ApoE4 astrocytes is reversed by epigenetic correction of endosomal pH. Proc Natl Acad Sci. 10. Juli 2018;115(28):E6640–9.

121. Lagadic-Gossmann D, Huc L, Lecureur V. Alterations of intracellular pH homeostasis in apoptosis: origins and roles. Cell Death Differ. September 2004;11(9):953–61.

122. Jeong JH, Chang JS, Jo Y-H. Intracellular glycolysis in brown adipose tissue is essential for optogenetically induced nonshivering thermogenesis in mice. Sci Rep. Dezember 2018;8(1):6672.

123. Westerblad H, Allen DG, Lännergren J. Muscle Fatigue: Lactic Acid or Inorganic Phosphate the Major Cause? Physiology. Februar 2002;17(1):17–21.

124. Spriet LL, Howlett RA, Heigenhauser GJF. An enzymatic approach to lactate production in human skeletal muscle during exercise: Med Sci Sports Exerc. April 2000;32(4):756–63.

125. Nalbandian M, Takeda M. Lactate as a Signaling Molecule That Regulates Exercise-Induced Adaptations. Biology. 8. Oktober 2016;5(4):38.

126. Gatenby RA, Gillies RJ. Why do cancers have high aerobic glycolysis? Nat Rev Cancer. November 2004;4(11):891–9.

127. Son SW, Chau GC, Kim S-T, Um SH. Vacuolar H+-ATPase Subunit V0C Regulates Aerobic Glycolysis of Esophageal Cancer Cells via PKM2 Signaling. Cells. 24. September 2019;8(10):1137.

128. Schulze A, Harris AL. How cancer metabolism is tuned for proliferation and vulnerable to disruption. Nature. November 2012;491(7424):364–73.

129. Warburg O. On the Origin of Cancer Cells. Science. 24. Februar 1956;123(3191):309–14.

130. Huang W-C, Swietach P, Vaughan-Jones RD, Ansorge O, Glitsch MD. Extracellular Acidification Elicits Spatially and Temporally Distinct Ca 2+ Signals. Curr Biol. Mai 2008;18(10):781–5.

131. Kato Y, Ozawa S, Miyamoto C, Maehata Y, Suzuki A, Maeda T, u. a. Acidic extracellular microenvironment and cancer. Cancer Cell Int. 2013;13(1):89.

132. Wojtkowiak JW, Verduzco D, Schramm KJ, Gillies RJ. Drug Resistance and Cellular Adaptation to Tumor Acidic pH Microenvironment. Mol Pharm. 5. Dezember 2011;8(6):2032–8.

133. Miyawaki A, Llopis J, Heim R, McCaffery JM, Adams JA, Ikura M, u. a. Fluorescent indicators for Ca2+based on green fluorescent proteins and calmodulin. Nature. August 1997;388(6645):882–7.

134. Bischof H, Rehberg M, Stryeck S, Artinger K, Eroglu E, Waldeck-Weiermair M, u. a. Novel genetically encoded fluorescent probes enable real-time detection of potassium in vitro and in vivo. Nat Commun. Dezember 2017;8(1):1422.

135. Lindenburg LH, Vinkenborg JL, Oortwijn J, Aper SJA, Merkx M. MagFRET: The First Genetically Encoded Fluorescent Mg2+ Sensor. Soares CM, Herausgeber. PLoS ONE. 2. Dezember 2013;8(12):e82009.

136. Imamura H, Huynh Nhat KP, Togawa H, Saito K, Iino R, Kato-Yamada Y, u. a. Visualization of ATP levels inside single living cells with fluorescence resonance energy transfer-based genetically encoded indicators. Proc Natl Acad Sci. 15. September 2009;106(37):15651–6.

137. Esposito A, Gralle M, Dani MAC, Lange D, Wouters FS. pHlameleons: A Family of FRET-Based Protein Sensors for Quantitative pH Imaging †. Biochemistry. 9. Dezember 2008;47(49):13115–26.

138. Miesenböck G, De Angelis DA, Rothman JE. Visualizing secretion and synaptic transmission with pH-sensitive green fluorescent proteins. Nature. Juli 1998;394(6689):192–5.

139. Hanson GT, McAnaney TB, Park ES, Rendell MEP, Yarbrough DK, Chu S, u. a. Green Fluorescent Protein Variants as Ratiometric Dual Emission pH Sensors. 1. Structural Characterization and Preliminary Application †. Biochemistry. Dezember 2002;41(52):15477–88.

140. Raimondo J. A genetically-encoded chloride and pH sensor for dissociating ion dynamics in the nervous system. Front Cell Neurosci [Internet]. 2013 [zitiert 29. Januar 2020];7. Verfügbar unter: http://journal.frontiersin.org/article/10.3389/fncel.2013.00202/abstract

141. Bajar B, Wang E, Zhang S, Lin M, Chu J. A Guide to Fluorescent Protein FRET Pairs. Sensors. 14. September 2016;16(9):1488.

142. Zhou C, Zhong W, Zhou J, Sheng F, Fang Z, Wei Y, u. a. Monitoring autophagic flux by an improved tandem fluorescent-tagged LC3 (mTagRFP-mWasabi-LC3) reveals that high-dose rapamycin impairs autophagic flux in cancer cells. Autophagy. 31. August 2012;8(8):1215–26.

143. Matlashov ME, Bogdanova YA, Ermakova GV, Mishina NM, Ermakova YG, Nikitin ES, u. a. Fluorescent ratiometric pH indicator SypHer2: Applications in neuroscience and regenerative biology. Biochim Biophys Acta BBA - Gen Subj. November 2015;1850(11):2318–28.

144. Ermakova YG, Pak VV, Bogdanova YA, Kotlobay AA, Yampolsky IV, Shokhina AG, u. a. SypHer3s: a genetically encoded fluorescent ratiometric probe with enhanced brightness and an improved dynamic range. Chem Commun. 2018;54(23):2898–901.

145. Tantama M, Hung YP, Yellen G. Imaging Intracellular pH in Live Cells with a Genetically Encoded Red Fluorescent Protein Sensor. J Am Chem Soc. 6. Juli 2011;133(26):10034–7.

146. Li Y, Tsien RW. pHTomato, a red, genetically encoded indicator that enables multiplex interrogation of synaptic activity. Nat Neurosci. Juli 2012;15(7):1047–53.

147. Poburko D, Santo-Domingo J, Demaurex N. Dynamic Regulation of the Mitochondrial Proton Gradient during Cytosolic Calcium Elevations. J Biol Chem. 1. April 2011;286(13):11672–84.

148. Zurzolo C, Simons K. Glycosylphosphatidylinositol-anchored proteins: Membrane organization and transport. Biochim Biophys Acta BBA - Biomembr. April 2016;1858(4):632–9.

149. Chatterjee S, Mayor S. The GPI-anchor and protein sorting: Cell Mol Life Sci. Dezember 2001;58(14):1969–87.

150. Ranscht B, Dours-Zimmermann MT. T-cadherin, a novel cadherin cell adhesion molecule in the nervous system lacks the conserved cytoplasmic region. Neuron. September 1991;7(3):391–402.

151. Griffiths G, Pfeiffer S, Simons K, Matlin K. Exit of newly synthesized membrane proteins from the trans cisterna of the Golgi complex to the plasma membrane. J Cell Biol. 1. September 1985;101(3):949–64.

152. Grisshammer R, Tateu CG. Overexpression of integral membrane proteins for structural studies. Q Rev Biophys. August 1995;28(3):315–422.

153. Anderson M, Moshnikova A, Engelman DM, Reshetnyak YK, Andreev OA. Probe for the measurement of cell surface pH in vivo and ex vivo. Proc Natl Acad Sci. 19. Juli 2016;113(29):8177–81.

154. Ohgaki R, Teramura Y, Hayashi D, Quan L, Okuda S, Nagamori S, u. a. Ratiometric fluorescence imaging of cell surface pH by poly(ethylene glycol)-phospholipid conjugated with fluorescein isothiocyanate. Sci Rep. Dezember 2017;7(1):17484.

155. Ke G, Zhu Z, Wang W, Zou Y, Guan Z, Jia S, u. a. A Cell-Surface-Anchored Ratiometric Fluorescent Probe for Extracellular pH Sensing. ACS Appl Mater Interfaces. 10. September 2014;6(17):15329–34.

156. Bayer EA, Wilchek M. The Use of the Avidin-Biotin Complex as a Tool in Molecular Biology. In: Glick D, Herausgeber. Methods of Biochemical Analysis [Internet]. Hoboken, NJ, USA: John Wiley & Sons, Inc.; 2006 [zitiert 29. Januar 2020]. S. 1–45. Verfügbar unter: http://doi.wiley.com/10.1002/9780470110461.ch1

157. Karhemo P-R, Ravela S, Laakso M, Ritamo I, Tatti O, Mäkinen S, u. a. An optimized isolation of biotinylated cell surface proteins reveals novel players in cancer metastasis. J Proteomics. Dezember 2012;77:87–100.

158. Xu T-H, Yan Y, G. Harikumar K, J. Miller L. Streptavidin bead pulldown assay to determine homooligomerization. BIO-Protoc [Internet]. 2017 [zitiert 29. Januar 2020];7(24). Verfügbar unter: http://www.bio-protocol.org/e2901

159. Sarda S, Pointu D, Pincet F, Henry N. Specific Recognition of Macroscopic Objects by the Cell Surface: Evidence for a Receptor Density Threshold Revealed by Micrometric Particle Binding Characteristics. Biophys J. Mai 2004;86(5):3291–303.

160. Howarth M, Takao K, Hayashi Y, Ting AY. Targeting quantum dots to surface proteins in living cells with biotin ligase. Proc Natl Acad Sci. 24. Mai 2005;102(21):7583–8.

161. Beckett D, Kovaleva E, Schatz PJ. A minimal peptide substrate in biotin holoenzyme synthetase-catalyzed biotinylation. Protein Sci. 31. Dezember 2008;8(4):921–9.

162. Cull MG, Schatz PJ. [26] Biotinylation of proteins in vivo and in vitro using small peptide tags. In: Methods in Enzymology [Internet]. Elsevier; 2000 [zitiert 29. Januar 2020]. S. 430–40. Verfügbar unter: https://linkinghub.elsevier.com/retrieve/pii/S0076687900260680

163. Barat B, Wu AM. Metabolic biotinylation of recombinant antibody by biotin ligase retained in the endoplasmic reticulum. Biomol Eng. September 2007;24(3):283–91.

164. Nesbeth D, Williams SL, Chan L, Brain T, Slater NKH, Farzaneh F, u. a. Metabolic Biotinylation of Lentiviral Pseudotypes for Scalable Paramagnetic Microparticle-Dependent Manipulation. Mol Ther. April 2006;13(4):814–22.

165. Chaiet L, Wolf FJ. The properties of streptavidin, a biotin-binding protein produced by Streptomycetes. Arch Biochem Biophys. 1964;106:1–5.

166. Chivers CE, Koner AL, Lowe ED, Howarth M. How the biotin–streptavidin interaction was made even stronger: investigation via crystallography and a chimaeric tetramer. Biochem J. 1. April 2011;435(1):55–63.

167. Chivers CE, Crozat E, Chu C, Moy VT, Sherratt DJ, Howarth M. A streptavidin variant with slower biotin dissociation and increased mechanostability. Nat Methods. Mai 2010;7(5):391–3.

168. Chen C, Okayama H. High-efficiency transformation of mammalian cells by plasmid DNA. Mol Cell Biol. August 1987;7(8):2745–52.

169. Goedhart J, von Stetten D, Noirclerc-Savoye M, Lelimousin M, Joosen L, Hink MA, u. a. Structure-guided evolution of cyan fluorescent proteins towards a quantum yield of 93%. Nat Commun. Januar 2012;3(1):751.

170. Kremers G-J, Goedhart J, van Munster EB, Gadella TWJ. Cyan and Yellow Super Fluorescent Proteins with Improved Brightness, Protein Folding, and FRET Förster Radius † , ‡. Biochemistry. Mai 2006;45(21):6570–80.

171. Balleza E, Kim JM, Cluzel P. Systematic characterization of maturation time of fluorescent proteins in living cells. Nat Methods. Januar 2018;15(1):47–51.

172. Rekas A, Alattia J-R, Nagai T, Miyawaki A, Ikura M. Crystal Structure of Venus, a Yellow Fluorescent Protein with Improved Maturation and Reduced Environmental Sensitivity. J Biol Chem. 27. Dezember 2002;277(52):50573–8.

173. Zhang Y, Robertson JB, Xie Q, Johnson CH. Monitoring Intracellular pH Change with a Genetically Encoded and Ratiometric Luminescence Sensor in Yeast and Mammalian Cells. In: Kim SB, Herausgeber. Bioluminescence [Internet]. New York, NY: Springer New York; 2016 [zitiert 29. Januar 2020]. S. 117–30. Verfügbar unter: http://link.springer.com/10.1007/978-1-4939-3813-1_9

174. Margolis LB, Novikova II, Rozovskaia IA, Skulachev VP. [The cytostatic action of the K+/H+ antiporter nigericin]. Vopr Onkol. 1990;36(8):952–6.

175. Smallridge RC, Gist ID, Kiang JG. Na+-H+ antiport and monensin effects on cytosolic pH and iodide transport in FRTL-5 rat thyroid cells. Am J Physiol-Endocrinol Metab. 1. Juni 1992;262(6):E834–9.

176. Burgstaller S, Bischof H, Gensch T, Stryeck S, Gottschalk B, Ramadani-Muja J, u. a. pH-Lemon, a Fluorescent Protein-Based pH Reporter for Acidic Compartments. ACS Sens. 26. April 2019;4(4):883–91.

177. Bischof H, Burgstaller S, Waldeck-Weiermair M, Rauter T, Schinagl M, Ramadani-Muja J, u. a. Live-Cell Imaging of Physiologically Relevant Metal Ions Using Genetically Encoded FRET-Based Probes. Cells. 22. Mai 2019;8(5):492.

178. Chen X, Zaro JL, Shen W-C. Fusion protein linkers: Property, design and functionality. Adv Drug Deliv Rev. Oktober 2013;65(10):1357–69.

179. Tanida I, Ueno T, Kominami E. Human Light Chain 3/MAP1LC3B Is Cleaved at Its Carboxyl-terminal Met ^{121} to Expose Gly ^{120} for Lipidation and Targeting to Autophagosomal Membranes. J Biol Chem. 12. November 2004;279(46):47704–10.

180. Palmer BF. Regulation of Potassium Homeostasis. Clin J Am Soc Nephrol. 5. Juni 2015;10(6):1050–60.

181. Meyer J, Untiet V, Fahlke C, Gensch T, Rose CR. Quantitative determination of cellular [Na+] by fluorescence lifetime imaging with CoroNaGreen. J Gen Physiol. 4. November 2019;151(11):1319–31.

182. Palmer AE, Jin C, Reed JC, Tsien RY. Bcl-2-mediated alterations in endoplasmic reticulum Ca2+ analyzed with an improved genetically encoded fluorescent sensor. Proc Natl Acad Sci. 14. Dezember 2004;101(50):17404–9.

183. Nemoto Y. Recruitment of an alternatively spliced form of synaptojanin 2to mitochondria by the interaction with the PDZ domain of a mitochondrial outer membrane protein. EMBO J. 1. Juni 1999;18(11):2991–3006.

184. Palmer AE, Tsien RY. Measuring calcium signaling using genetically targetable fluorescent indicators. Nat Protoc. August 2006;1(3):1057–65.

185. Mellman I, Fuchs R, Helenius A. Acidification of the Endocytic and Exocytic Pathways. Annu Rev Biochem. Juni 1986;55(1):663–700.

186. Tanida I, Ueno T, Kominami E. LC3 and Autophagy. In: Deretic V, Herausgeber. Autophagosome and Phagosome [Internet]. Totowa, NJ: Humana Press; 2008 [zitiert 29. Januar 2020]. S. 77–88. Verfügbar unter: http://link.springer.com/10.1007/978-1-59745-157-4_4

187. Shang L, Chen S, Du F, Li S, Zhao L, Wang X. Nutrient starvation elicits an acute autophagic response mediated by Ulk1 dephosphorylation and its subsequent dissociation from AMPK. Proc Natl Acad Sci. 22. März 2011;108(12):4788–93.

188. Wang D, Hiesinger PR. The vesicular ATPase: A missing link between acidification and exocytosis. J Cell Biol. 28. Oktober 2013;203(2):171–3.

189. Jackson MP, Hewitt EW. Cellular proteostasis: degradation of misfolded proteins by lysosomes. van Oosten-Hawle P, Herausgeber. Essays Biochem. 15. Oktober 2016;60(2):173–80.

190. Dean RT. LYSOSOMAL MECHANISMS OF PROTEIN DEGRADATION. In: Protein Turnover and Lysosome Function [Internet]. Elsevier; 1978 [zitiert 29. Januar 2020]. S. 29–41. Verfügbar unter: https://linkinghub.elsevier.com/retrieve/pii/B9780126361506500088

191. Marchetti A, Lelong E, Cosson P. A measure of endosomal pH by flow cytometry in Dictyostelium. BMC Res Notes. 2009;2(1):7.

192. Pierzyńska-Mach A, Janowski PA, Dobrucki JW. Evaluation of acridine orange, LysoTracker Red, and quinacrine as fluorescent probes for long-term tracking of acidic vesicles: Tracking Acidic Vesicles. Cytometry A. August 2014;85(8):729–37.

193. Decrock E, Vinken M, Bol M, D'Herde K, Rogiers V, Vandenabeele P, u. a. Calcium and connexin-based intercellular communication, a deadly catch? Cell Calcium. September 2011;50(3):310–21.

194. McCarty MF, Whitaker J. Manipulating tumor acidification as a cancer treatment strategy. Altern Med Rev J Clin Ther. September 2010;15(3):264–72.

195. Bischof H, Burgstaller S, Vujic N, Madl T, Kratky D, Graier WF, u. a. Purification and Application of Genetically Encoded Potassium Ion Indicators for Quantification of Potassium Ion Concentrations within Biological Samples. Curr Protoc Chem Biol [Internet]. September 2019 [zitiert 30. Januar 2020];11(3). Verfügbar unter: https://onlinelibrary.wiley.com/doi/abs/10.1002/cpch.71

196. Li Y, Sousa R. Expression and purification of E. coli BirA biotin ligase for in vitro biotinylation. Protein Expr Purif. März 2012;82(1):162–7.

197. Eil R, Vodnala SK, Clever D, Klebanoff CA, Sukumar M, Pan JH, u. a. Ionic immune suppression within the tumour microenvironment limits T cell effector function. Nature. September 2016;537(7621):539–43.

198. Ashraf KU, Josts I, Mosbahi K, Kelly SM, Byron O, Smith BO, u. a. The Potassium Binding Protein Kbp Is a Cytoplasmic Potassium Sensor. Structure. Mai 2016;24(5):741–9.

199. Lemieux G, Aranda MR, Fournel P, Lemieux C. Renal enzymes during experimental diabetes mellitus in the rat. Role of insulin, carbohydrate metabolism, and ketoacidosis. Can J Physiol Pharmacol. 1. Januar 1984;62(1):70–5.

200. Maalouf NM, Cameron MA, Moe OW, Adams-Huet B, Sakhaee K. Low Urine pH: A Novel Feature of the Metabolic Syndrome. Clin J Am Soc Nephrol. September 2007;2(5):883–8.

201. Chaumeil MM, Valette J, Baligand C, Brouillet E, Hantraye P, Bloch G, u. a. pH as a Biomarker of Neurodegeneration in Huntington's Disease: A Translational Rodent-Human MRS Study. J Cereb Blood Flow Metab. Mai 2012;32(5):771–9.

202. Fujikake N, Shin M, Shimizu S. Association Between Autophagy and Neurodegenerative Diseases. Front Neurosci. 22. Mai 2018;12:255.

203. Wang T, Hay JC. Alpha-synuclein Toxicity in the Early Secretory Pathway: How It Drives Neurodegeneration in Parkinsons Disease. Front Neurosci [Internet]. 12. November 2015 [zitiert 30. Januar 2020];9. Verfügbar unter: http://journal.frontiersin.org/Article/10.3389/fnins.2015.00433/abstract

204. Allison KE, Coomber BL, Bridle BW. Metabolic reprogramming in the tumour microenvironment: a hallmark shared by cancer cells and T lymphocytes. Immunology. Oktober 2017;152(2):175–84.

205. Pakhomov AA, Martynov VI, Orsa AN, Bondarenko AA, Chertkova RV, Lukyanov KA, u. a. Fluorescent protein Dendra2 as a ratiometric genetically encoded pH-sensor. Biochem Biophys Res Commun. Dezember 2017;493(4):1518–21.

206. Serresi M, Bizzarri R, Cardarelli F, Beltram F. Real-time measurement of endosomal acidification by a novel genetically encoded biosensor. Anal Bioanal Chem. Februar 2009;393(4):1123–33.

207. Leavesley SJ, Rich TC. Overcoming limitations of FRET measurements. Cytometry A. April 2016;89(4):325–7.

208. Zheng K, Jensen TP, Rusakov DA. Monitoring intracellular nanomolar calcium using fluorescence lifetime imaging. Nat Protoc. März 2018;13(3):581–97.

209. Rakymzhan A, Radbruch H, Niesner RA. Quantitative Imaging of Ca2+ by 3D–FLIM in Live Tissues. In: Dmitriev RI, Herausgeber. Multi-Parametric Live Cell Microscopy of 3D Tissue Models [Internet]. Cham: Springer International Publishing; 2017 [zitiert 30. Januar 2020]. S. 135–41. Verfügbar unter: http://link.springer.com/10.1007/978-3-319-67358-5_9

210. Rizzo MA, Springer GH, Granada B, Piston DW. An improved cyan fluorescent protein variant useful for FRET. Nat Biotechnol. April 2004;22(4):445–9.

211. Waldeck-Weiermair M, Alam MR, Khan MJ, Deak AT, Vishnu N, Karsten F, u. a. Spatiotemporal Correlations between Cytosolic and Mitochondrial Ca2+ Signals Using a Novel Red-Shifted Mitochondrial Targeted Cameleon. Degtyar VE, Herausgeber. PLoS ONE. 21. September 2012;7(9):e45917.

212. Piper RC, Katzmann DJ. Biogenesis and Function of Multivesicular Bodies. Annu Rev Cell Dev Biol. November 2007;23(1):519–47.

213. Roizin L, Nishikawa K, Koizumi J, Keoseian S. The Fine Structure of the Multivesicular Body and Their Relationship to the Ultracellular Constituents of the Central Nervous System * †. J Neuropathol Exp Neurol. April 1967;26(2):223–49.

214. Altick AL, Baryshnikova LM, Vu TQ, von Bartheld CS. Quantitative analysis of multivesicular bodies (MVBs) in the hypoglossal nerve: Evidence that neurotrophic factors do not use MVBs for retrograde axonal transport. J Comp Neurol. 20. Juni 2009;514(6):641–57.

215. Xu H, Ren D. Lysosomal Physiology. Annu Rev Physiol. 10. Februar 2015;77(1):57–80.

216. Xiong J, Zhu MX. Regulation of lysosomal ion homeostasis by channels and transporters. Sci China Life Sci. August 2016;59(8):777–91.

217. Okajima F. Regulation of inflammation by extracellular acidification and proton-sensing GPCRs. Cell Signal. November 2013;25(11):2263–71.

218. Anderson RG, Orci L. A view of acidic intracellular compartments. J Cell Biol. 1. März 1988;106(3):539–43.

219. Mizuguchi H, Xu Z, Ishii-Watabe A, Uchida E, Hayakawa T. IRES-Dependent Second Gene Expression Is Significantly Lower Than Cap-Dependent First Gene Expression in a Bicistronic Vector. Mol Ther. April 2000;1(4):376–82.

220. Predonzani A, Arnoldi F, López-Requena A, Burrone OR. In vivo site-specific biotinylation of proteins within the secretory pathway using a single vector system. BMC Biotechnol. 2008;8(1):41.

221. Villarreal S, Lee SH, Wu L-G. Measuring Synaptic Vesicle Endocytosis in Cultured Hippocampal Neurons. J Vis Exp JoVE. 04 2017;(127).

222. Suzuki M, Sato M, Koyama H, Hara Y, Hayashi K, Yasue N, u. a. Distinct intracellular Ca^{2+} dynamics regulate apical constriction and differentially contribute to neural tube closure. Development. 1. April 2017;144(7):1307–16.

223. Conley JM, Radhakrishnan S, Valentino SA, Tantama M. Imaging extracellular ATP with a genetically-encoded, ratiometric fluorescent sensor. Idzko M, Herausgeber. PLOS ONE. 9. November 2017;12(11):e0187481.

224. Hires SA, Zhu Y, Tsien RY. Optical measurement of synaptic glutamate spillover and reuptake by linker optimized glutamate-sensitive fluorescent reporters. Proc Natl Acad Sci. 18. März 2008;105(11):4411–6.

225. Bolognesi B, Lehner B. Reaching the limit. eLife. 10. August 2018;7:e39804.

226. Misonou H. Homeostatic Regulation of Neuronal Excitability by K^+ Channels in Normal and Diseased Brains. The Neuroscientist. Februar 2010;16(1):51–64.

227. Aggarwal NT, Makielski JC. Redox Control of Cardiac Excitability. Antioxid Redox Signal. Februar 2013;18(4):432–68.

228. Xiong Q-Y, Yu C, Zhang Y, Ling L, Wang L, Gao J-L. Key proteins involved in insulin vesicle exocytosis and secretion. Biomed Rep. Februar 2017;6(2):134–9.

229. Bouschet T, Henley JM. Calcium as an extracellular signalling molecule: perspectives on the Calcium Sensing Receptor in the brain. C R Biol. August 2005;328(8):691–700.

230. Mao S-Y. Biotinylation of Antibodies. In: Oliver C, Jamur MC, Herausgeber. Immunocytochemical Methods and Protocols [Internet]. Totowa, NJ: Humana Press; 2010 [zitiert 30. Januar 2020]. S. 49–52. Verfügbar unter: http://link.springer.com/10.1007/978-1-59745-324-0_7

231. Doshi R, Chen BR, Vibat CRT, Huang N, Lee C-W, Chang G. In vitro nanobody discovery for integral membrane protein targets. Sci Rep. Mai 2015;4(1):6760.

232. Jeevarajan AS, Vani S, Taylor TD, Anderson MM. Continuous pH monitoring in a perfused bioreactor system using an optical pH sensor. Biotechnol Bioeng. 20. Mai 2002;78(4):467–72.

233. Gao FG, Jeevarajan AS, Anderson MM. Long-term continuous monitoring of dissolved oxygen in cell culture medium for perfused bioreactors using optical oxygen sensors. Biotechnol Bioeng. 20. Mai 2004;86(4):425–33.

234. Daughton CG. Monitoring wastewater for assessing community health: Sewage Chemical-Information Mining (SCIM). Sci Total Environ. April 2018;619–620:748–64.